



Western Michigan University
ScholarWorks at WMU

Dissertations

Graduate College

8-2022

Peridynamic Modeling of Crack Propagation in Brittle Materials with Electromechanical Coupling

Semsi Coskun
Western Michigan University

Follow this and additional works at: <https://scholarworks.wmich.edu/dissertations>



Part of the Mechanical Engineering Commons

Recommended Citation

Coskun, Semsi, "Peridynamic Modeling of Crack Propagation in Brittle Materials with Electromechanical Coupling" (2022). *Dissertations*. 3892.

<https://scholarworks.wmich.edu/dissertations/3892>

This Dissertation-Open Access is brought to you for free and open access by the Graduate College at ScholarWorks at WMU. It has been accepted for inclusion in Dissertations by an authorized administrator of ScholarWorks at WMU. For more information, please contact wmu-scholarworks@wmich.edu.



PERIDYNAMIC MODELING OF CRACK PROPAGATION IN BRITTLE MATERIALS WITH ELECTROMECHANICAL COUPLING

Semsi Coskun, Ph.D.

Western Michigan University, 2022

The bond-based peridynamics (BB-PD) is a widely used peridynamic model in the literature. Despite Poisson's ratio restriction, it still serves as a powerful tool to solve challenging engineering problems with a relatively cheap computational cost. Consider the Poisson ratio of the material does not deviate from the ones that BB-PD can model. In that case, it becomes advantageous to use the BB-PD compared to other PD models in terms of computational cost and simplicity. However, the BB-PD suffers from the so-called *surface* or *skin effect* where the material response at boundaries becomes softer than the bulk material points. As a remedy, this study presents a new surface correction method that calculates the material parameters discretely during the numerical simulations. As a result, the accuracy of the BB-PD simulations is significantly improved for the problems with regular boundaries and the problems involving fractures where new boundaries emerge as the crack propagates and branches.

The piezoelectric ceramics have high stiffness compared to their natural counterparts and can be used efficiently as sensors, actuators, and transducers in various smart devices and structures. However, they have low ultimate tensile strength and fracture toughness, making them

susceptible to damage. Furthermore, the piezoelectric ceramics are operated at high electrical and mechanical loads. Therefore, studying piezoelectric materials' damage and cracking mechanisms is crucial to operating them safely. Therefore, this study utilizes the non-ordinary state-based peridynamics (NOSB-PD) to model the fully coupled electromechanical behavior and fracture of the transversely isotropic piezo ceramics. The results obtained from the proposed implicit formulation for the static problems agree well with the analytical solutions available in the literature. Finally, an iterative solution procedure is utilized to perform the mode-I fracture simulations of a pre-notched PZT-4 ceramic plate under combined electromechanical loading. The effect of the direction and magnitude of the applied electric field on the crack propagation under quasi-static conditions are discussed.

PERIDYNAMIC MODELING OF CRACK PROPAGATION IN BRITTLE MATERIALS WITH
ELECTROMECHANICAL COUPLING

by

Semsi Coskun

A dissertation submitted to the Graduate College
in partial fulfillment of the requirements
for the degree of Doctor of Philosophy
Mechanical and Aerospace Engineering
Western Michigan University
August 2022

Doctoral Committee:

Jinseok Kim, Ph.D., Chair
Judah Ari-Gur, D.Sc.
Daniel Kujawski, Ph.D., D.Sc.
Peter A. Gustafson, Ph.D.
Michael Powell, Ph.D.

© 2022 Semsî Coskun

ACKNOWLEDGMENTS

I would like to express my most profound appreciation to my advisor Dr. Jinseok Kim for his encouragement, patience, and continuous support. He always encouraged me to be an independent researcher, and at the same time, he was always there when I needed his help. I am grateful to have excellent guidance with his invaluable feedback and contributions.

I sincerely thank my committee members: Dr. Judah Ari-Gur, Dr. Daniel Kujawski, Dr. Peter Gustafson, and Dr. Michael Powell. Their thoughtful questions and suggestions helped me develop a deeper perspective on my thesis. Furthermore, I am fortunate to have the opportunity to discuss my results with Dr. Powell throughout my studies. Hence, my special thanks go to Dr. Powell for his invaluable discussions and suggestions.

I want to extend my sincere thanks to Dr. Ari-Gur. It is always my pleasure to be his TA and student. He is such an incredible mentor that enlightenment comes with tremendous joy when brainstorming. Also, he is one of the few people that make me feel at home, safe and secure. So, I am profoundly grateful for his emotional support. Also, I want to thank the WMU MAE Department for supporting me by providing a teaching assistantship during my study.

In addition, I wish to thank my teammates: Francisco Americo Yapor Genao and Enrique Nava Munoz, for their positive and supportive discussions.

Also, I would like to express my deepest gratitude to my parents, Zohre and Hasan Coskun, and my brother Musa Dede Coskun. Their unconditional trust and love provide me the energy to

Acknowledgments–Continued

move on.

Finally, my warmest thanks go to my husband, Salih Can Rakici. I am grateful for his understanding, support, and love.

Semsi Coskun

TABLE OF CONTENTS

ACKNOWLEDGMENTS	ii
LIST OF TABLES	vii
LIST OF FIGURES	xii

CHAPTER

1 INTRODUCTION	1
1.1 Background Information	1
1.2 Literature Review	3
1.3 Problem Statement and Significance	13
1.4 Objectives and Outline	14
2 BB-PD WITH A NEW SURFACE CORRECTION METHOD	16
2.1 Bond-Based Peridynamic Model	16
2.1.1 A brief description of bond-based peridynamics	16
2.1.2 Discretization of BB-PD equations	18
2.2 Discrete Surface Correction Method	21
2.2.1 Determination of PD micromodulus	21
2.2.2 Discrete calculation of the micromodulus	24
2.2.3 Determination of PD critical stretch	26
2.2.4 Discrete calculation of the critical stretch	27
2.3 Numerical Examples	32
2.3.1 A rectangular plate under uniaxial tension	32
2.3.2 Plate with a center hole	36
2.3.3 Uniaxial dynamic loading	40
2.3.4 Kalthoff-Winkler's experiment	47

Table of Contents–Continued

CHAPTER

2.4	Chapter Summary	51
3	NOSB-PD WITH ELECTROMECHANICAL COUPLING	52
3.1	A Brief Description of Non-Ordinary State-Based Peridynamics	52
3.1.1	Discrete equations of non-ordinary state-based peridynamics	53
3.2	Linear Piezoelectricity in Classical Continuum Mechanics	58
3.2.1	Constitutive equations	58
3.2.2	In-plane and anti-plane piezoelectric equations	63
3.2.3	Governing equations of a piezoelectric continuum	64
3.3	Non-Ordinary State-Based Formulation for Linear Piezoelectricity	65
3.4	An Implicit Formulation for Static Linear Piezoelectricity in Non-Ordinary State-Based Peridynamics	68
3.5	Numerical Examples	70
3.5.1	A two-dimensional piezoelectric beam with an analytical solution	70
3.5.2	A two-Dimensional piezoelectric strip with fixed-fixed boundaries	74
3.5.3	A two-dimensional piezoelectric strip under compression and an applied electric field perpendicular to the poling axis	77
3.6	Chapter Summary	82
4	NOSB-PD WITH ELECTROMECHANICAL COUPLING FOR FRACTURE PROB- LEMS	83
4.1	A Brief Description of the Solution Procedure	83
4.2	Finite Difference Discretization of Electrical Equilibrium Equation	85
4.2.1	Iterative solution technique for the electric potential field	93
4.3	Mode-I Fracture Problem	98
4.4	Chapter Summary	110

Table of Contents–Continued

CHAPTER	
5	CONCLUSIONS AND FUTURE WORKS 111
5.1	Future Works 112
REFERENCES 113

LIST OF TABLES

3.1	Material Properties of PZT-5 [69]	70
3.2	Material Properties of PVDF [102]	75
4.1	Material Properties of PZT-4 [13]	98

LIST OF FIGURES

2.1	A PD body in the reference (left) and deformed (right) configurations	17
2.2	Partial areas	19
2.3	PD body under a prescribed strain field (left) and the resulting deformation of the bond ξ (adopted from [97])	22
2.4	Evaluation of fracture energy (adopted from [109])	27
2.5	PD domain including a crack	28
2.6	Illustration of the broken bonds: (a) set I, (b) set II, and (c) set III	29
2.7	Broken bonds used in simplified calculation of the critical stretch discretely, corresponding to (a) set I, (b) set II, and (c) set III	30
2.8	Problem setup: A plate under uniaxial tension	33
2.9	Contour plots for absolute relative difference [%] of x-displacements in CCM and PD re- sults with (a) no correction, (b) Silling's, (c) Madenci's, and (d) discrete surface correction methods, 100×50 , $\delta = 5h$	33
2.10	Contour plots for absolute relative difference [%] of y-displacements in CCM and PD re- sults with (a) no correction, (b) Silling's, (c) Madenci's, and (d) discrete surface correction methods, 100×50 , $\delta = 5h$	34
2.11	Change of maximum absolute relative differences in (a) x, and (b) y-displacements with different m-ratios	35
2.12	Problem setup: A square plate with a center hole is subjected to uniaxial tensile stress	36
2.13	Results of FEA: (a) horizontal, and (b) vertical displacement fields	36
2.14	PD results for x-displacement [m] with (a) no correction, (b) Silling's, (c) Madenci's, and (d) Current discrete surface correction methods, $\delta = 5h$	37
2.15	PD results for y-displacement [m] with (a) no correction, (b) Silling's, (c) Madenci's, and (d) Current discrete surface correction methods, $\delta = 5h$	38
2.16	Comparison of the horizon displacement field along the line $y = 0$ and $0.05 < x < 0.03$ m, $\delta = 5h$	39

List of Figures–Continued

2.17	Comparison of the vertical displacement field along the line $x = 0$ and $0.05 < y < 0.03$ m, $\delta = 5h$	40
2.18	Comparison of the horizon displacement field along the line $y = 0$ and $0.05 < x < 0.03$ m, for different horizon sizes	41
2.19	Comparison of the vertical displacement field along the line $x = 0$ and $0.05 < y < 0.03$ m, for different horizon sizes	41
2.20	Problem setup: a plate under uniaxial dynamic loading	42
2.21	Comparison of crack paths under uniaxial dynamic loading of 12 MPa with (a) no correc- tion, (b) Silling’s, (c) Madenci’s, and (d) Current discrete surface corrections, 200×80 , $\delta = 5h$	43
2.22	Comparison of crack paths under uniaxial dynamic loading of 12 MPa with (a) no correc- tion, (b) Silling’s, (c) Madenci’s, and (d) Current discrete surface corrections, 400×160 , $\delta = 5h$	43
2.23	Comparison of crack paths under uniaxial dynamic loading of 30 MPa with (a) no correc- tion, (b) Silling’s, (c) Madenci’s, and (d) Current discrete surface corrections, 200×80 , $\delta = 5h$	45
2.24	Comparison of crack paths under uniaxial dynamic loading of 30 MPa with (a) no correc- tion, (b) Silling’s, (c) Madenci’s, and (d) Current discrete surface corrections, 400×160 , $\delta = 5h$	45
2.26	Crack paths results under uniaxial dynamic loading of 12 MPa for PD simulation with discrete surface correction and $\delta =$ (a) $3h$, (b) $4h$, and (c) $5h$ in a 400×160 grid	46
2.27	Crack paths results under uniaxial dynamic loading of 30 MPa for PD simulation with discrete surface correction and $\delta =$ (a) $3h$, (b) $4h$, and (c) $5h$ in a 200×80 grid	47
2.28	Crack paths results under uniaxial dynamic loading of 30 MPa for PD simulation with discrete surface correction and $\delta =$ (a) $3h$, (b) $4h$, and (c) $5h$ in a 400×160 grid	47
2.29	Numerical model to simulate Kalthoff-Winkler’s experiment	48

List of Figures–Continued

2.30	Comparison of crack paths with the experimental result (solid white line) and peridynamic simulation with (a) no correction, (b) Silling’s, (c) Madenci’s, and (d) Current discrete surface correction methods, 200×200 , $\delta = 5h$	49
2.31	Comparison of crack paths with the experimental result (solid white line) and peridynamic simulation with (a) no correction, (b) Silling’s, (c) Madenci’s, and (d) Current discrete surface correction methods, 400×400 , $\delta = 5h$	49
2.32	Comparison of crack paths with the experimental result (solid white line) and PD simulation with discrete surface correction and $\delta =$ (a) $3h$, (b) $4h$, and (c) $5h$ in a 200×200 grid	50
2.33	Comparison of crack paths with the experimental result (solid white line) and PD simulation with discrete surface correction and $\delta =$ (a) $3h$, (b) $4h$, and (c) $5h$ in a 400×400 grid	50
3.1	Problem setup: A two-dimensional PZT-5 strip. Adopted from [68].	71
3.2	PD solutions for (a) ϕ [V], (b) u [nm], and (c) w [nm].	72
3.3	Comparison of the PD solutions along the $x = 0.5$ mm line (a) u , (b) w , and (c) ϕ	73
3.4	Comparison of the PD solutions along the $z = 0$ and $0 \leq x \leq 0.5$ mm line (a) u , (b) w , and (c) ϕ	74
3.5	Problem setup: A two-dimensional PVDF strip. Adopted from [102].	75
3.6	PD solutions for (a) ϕ [V], (b) u [nm], and (c) w [nm].	76
3.7	Comparison of the PD solutions along the $z = 2$ mm line (a) u , and (b) w	77
3.8	Comparison of the PD solutions along the $x = 5$ mm line (a) w , and (b) ϕ	77
3.9	Problem setup: A two-dimensional PZT-5 strip under uniform compression. Adopted from [69].	78
3.10	Distribution of (a) PD, and (b) exact solution for ϕ [V].	79
3.11	Distribution of (a) PD, and (b) exact solution for u [nm].	79
3.12	Distribution of (a) PD, and (b) exact solution for w [nm].	79

List of Figures–Continued

3.13 Comparison of the PD solutions along the $z = 0$ line (a) u , (b) w , and (c) ϕ 80

3.14 Comparison of the PD solutions along the $z = 0.25$ mm line (a) u , (b) w , and (c) ϕ 81

4.1 Implementation of the iterative solution at each time step for electromechanical system including fracture. 84

4.4 Problem setup: A pre-notched PZT-4 plate under tension and applied electric field. 98

4.5 Comparison of the fracture load versus applied electric field with the PD results and the experimental data [13]. 99

4.6 Reaction force versus applied displacement results for (a) coarse, and (b) fine meshes with $\delta = 3.015h$ 100

4.7 Reaction force versus applied displacement results for (a) coarse, and (b) fine meshes with $\delta = 4.015h$ 101

4.8 (a-b) Damage, (c-d) w [μm], and (e-f) ϕ [V] distributions at the crack opening for an applied electric field of -2.5 kV/m at the left and +2.5 kV/m at the right. 103

4.9 (a-b) Damage, (c-d) w [μm], and (e-f) ϕ [V] distributions when the crack reaches approximately 18 mm for an applied electric field of -2.5 kV/m at the left and +2.5 kV/m at the right. 104

4.10 (a-b) Damage, (c-d) w [μm], and (e-f) ϕ [V] distributions when the crack reaches approximately 24 mm for an applied electric field of -2.5 kV/m at the left and +2.5 kV/m at the right. 105

4.11 (a-b) Damage, (c-d) w [μm], and (e-f) ϕ [V] distributions at the crack opening for an applied electric field of -5 kV/m at the left and +5 kV/m at the right. 106

4.12 (a-b) Damage, (c-d) w [μm], and (e-f) ϕ [V] distributions when the crack reaches approximately 18 mm for an applied electric field of -5 kV/m at the left and +5 kV/m at the right. 107

List of Figures–Continued

4.13 (a-b) Damage, (c-d) w [μm], and (e-f) ϕ [V] distributions when the crack reaches approximately 24 mm for an applied electric field of -5 kV/m at the left and +5 kV/m at the right. 108

4.14 (a) Damage, (b) w [μm], and (c) ϕ [V] distributions at the crack opening without an applied electric field. 109

4.15 (a) Damage, (b) w [μm], and (c) ϕ [V] distributions when the crack reaches approximately 18 mm without an applied electric field. 109

4.16 (a) Damage, (b) w [μm], and (c) ϕ [V] distributions when the crack reaches approximately 24 mm without an applied electric field. 109

CHAPTER 1

INTRODUCTION

1.1 Background Information

The partial differential equations of the classical continuum mechanics (CCM) are singular at the point of discontinuity, such as cracks. Linear elastic fracture mechanics (LEFM) is one of the most commonly utilized tools to obtain the solutions around the crack locations. Unfortunately, the LEFM presents considerable drawbacks to use. First, LEFM offers closed-form solutions for a limited number of crack configurations with particular loading and geometry. The analytical calculations of the stress intensity factor are derived for simple configurations such as through a crack in an infinite plate that is subjected to remote tensile stress. For more complex crack configurations, the stress intensity factor can be obtained by experiments or numerical analyses [1]. Second, and perhaps most importantly, it is necessary to know the crack location before using the LEFM equations. These drawbacks make the LEFM impractical and even unavailable to be utilized in complex problems. With this motivation, Silling [2] proposed peridynamics (PD) as a new mathematical framework that remains valid regardless of discontinuities in the problem domain.

This new continuum model is based on integrodifferential equations without spatial derivatives. This feature allows unifying the set of equations used for the entire problem domain regardless of the singularities. Also, the determination of the initiation, growth, direction and branching of cracks does not need predefined rules other than damage criterion [3]. Instead, the fracture is considered a result of deformation in conjunction with the material model. In addition, PD is a nonlocal model in which material particles interact within a finite distance, called *horizon*, rather than in a direct adjacency. The internal force at a material point acts as in the intermolecular and surface forces through this finite distance. This feature makes PD attractive for small-scale or

multi-scale modelings [4–7].

The bond-based peridynamics (BB-PD), the earliest version of the peridynamics, assumes that the interaction within a pair of material points is based on a central pairwise force which can be visualized as a spring force. Therefore, the Poisson ratio of linear elastic material is fixed to 1/4 for 3D and plane strain problems and 1/3 for plane stress problems. Furthermore, BB-PD exhibits surface effects causing a weak material behavior at the boundaries. There are several techniques published in the literature to eliminate this problem. However, none of them did consider the newly created boundaries due to crack propagation in the problem domain. This motivates us to propose a new correction method for BB-PD that is also efficient for the problems with crack propagation.

In 2007, Silling et al. [8] proposed a *state-based* formulation for peridynamics where the interaction between the material points is affected by all material points within the neighborhood. The state-based peridynamics (SB-PD) [8] provides a significant improvement to model materials with a Poisson ratio other than 1/4 within a peridynamic framework and provides mathematical operators to adopt the material models from the CCM to peridynamics. There are two types of material models used in state-based peridynamics. The first one is called *ordinary state-based peridynamics* (OSB-PD), which is the extension of the BB-PD. The second one is *non-ordinary state-based peridynamics* (NOSB-PD) which allows us to use the material models in the CCM.

On the other hand, today's technology offers dramatic changes in terms of engineering structures. The micro-electro-mechanical systems (MEMS) and nano-electro-mechanical systems (NEMS) find broad application in many mechanical and aerospace engineering fields. These technological devices use piezoelectric materials as sensors, actuators, and transducers due to their inherited properties [9, 10]. A piezoelectric sensor converts mechanical vibrations or forces into a measurable electric field. The same material can be used as actuators that convert the electrical signal into displacement or force [11]. However, most piezoelectric ceramics are susceptible to damage due to their brittleness and low fracture toughness [12]. Damage or fracture of piezoelectric ceramics can result in reduced efficiency or failure of the device [12–14].

Non-ordinary state-based peridynamics provides an opportunity to use the available constitutive relations in CCM with the great advantage of peridynamics to model fracture simulations. This feature helps us develop a fully coupled electromechanical peridynamic model for linear piezoelectricity and investigate the fracture behavior of piezoelectric ceramics within the peridy-

namic framework.

1.2 Literature Review

The governing equations of PD can be discretized using several methods [15]. First, the weak form of the governing equations can be obtained using a finite element discretization [15–17]. Alternatively, the strong form of the equations can be used directly in the meshfree discretization. It is most widely used in the literature due to its simplicity in numerical implementation and the low computational cost compared to other discretization techniques [18]. Silling and Askari [19] proposed the first meshfree discretization technique for PD, known as meshless or EMU discretization. In this technique, the problem domain is divided into nodes with known volumes (in 3D) or areas (in 2D), and the integral terms in the governing equations are transformed into finite sums over the neighborhood for each node. The neighborhood of a node is defined as a sphere (in 3D) or disk (in 2D) with the radius of the horizon centered at the node. In this discretization, the node center is considered the quadrature point, and the nodal volumes (or areas) of the neighbor nodes are interpreted as the summation weights. Later, various algorithms have been developed to improve the selection of quadrature points and summation weights for better accuracy and convergence of the meshless discretization-based PD simulation. Most of these algorithms focus on improving the calculation of the summation weights. One way to do it is to use the area (or volume) of the overlapping region between the node’s neighborhood and the neighboring nodes’ area (or volume) as the summation weight. As one may expect, a partial overlapping (called *partial volumes* in 3D and *partial areas* in 2D) exists for the neighbor nodes located at the boundary of the neighborhood of any node. However, an exact calculation of these partial areas (or volumes) is not straightforward and not always possible. Therefore, the approximations of these partial areas (or volumes) result in the primary source of numerical errors resulting from the spatial discretization of integral equations in meshless schemes.

One of the algorithms that improve the spatial integration of the meshfree discretization was proposed in a study implementing the PD into a molecular dynamics model [20]. This algorithm is called PA-PDLAMMPS or PV-PDLAMMPS, where “PA” and “PV” stand for the partial area and partial volume, respectively, and “PDLAMMPS” is the name of a PD module for a molec-

ular dynamics package (LAMMPS). Later, the so-called “PV-HHB” algorithm is proposed where “HHB” is the initials of the three authors of the study [21]. The present study uses the PA-HHB algorithm to enhance the numerical accuracy of the meshless method.

Yu et al. [22] proposed an adaptive integration method based on geometrical classifications and calculation of the overlapping areas with controlled accuracy using the trapezoidal rule. Seleson [23], on the other hand, further improved one-point quadrature algorithms for 2D PD models. He calculated the partial areas and their centroids analytically for several different configurations. Then, the analytically calculated overlapping areas are used as the summation weights and centroids as quadrature points. This approach was applied to the previous partial volume correction PA-HHB algorithm, which significantly improved the accuracy and convergence of this algorithm. However, the given analytical calculations of area and centroid are only valid for uniform grids in 2D.

Another approach to improve numerical integration in PD is to use a kernel that decays to zero at the neighborhood boundary. This idea was initially suggested by Yu et al. [22] and implemented by Seleson [23] with the help of influence functions introduced by Silling and his coworkers [8]. It is shown that if the influence function decays to zero at the boundary nodes of the neighborhood, the contribution, including the discretization error from these nodes, of boundary nodes of the neighborhood can be significantly reduced [18, 23].

Gerstle [24, 25] introduced rotational degrees of freedom to the BB-PD model and proposed the *micropolar peridynamic model*. Diana and Casolo [26] enhanced the micropolar peridynamic model by introducing a shear stiffness term in addition to normal and rotational stiffness of the microelastic energy function. Also, several bond-based models enriched with bond rotations [27–29] have recently been proposed to prevent Poisson ratio restriction.

The BB-PD has at least two material parameters. One is the *bond constant*, stiffness of the bonds between material points. The other one is the *critical bond stretch*, which is the ultimate stretch value that a bond can have without failure. As a common practice, these parameters are calculated analytically for bulk material points and used in the entire problem domain. For example, a PD material constant for linear elastic material is calculated by equating the strain energy densities obtained from CCM and PD under a given deformation. When two counterpart expressions are equating, integral terms in PD expressions are evaluated analytically, assuming a complete

neighborhood. The resulting PD material constant is then used for the entire domain, resulting in a softer material response at boundary nodes where the neighborhood is incomplete compared to bulk material nodes. This effect is called the *surface* or *skin effect*.

Various surface correction algorithms are suggested in the literature to minimize skin effects. It is possible to categorize them into three. The methods in the first category restore the missing neighborhood by adding fictitious nodes along the problem boundary; therefore, one can safely use the analytically calculated PD parameters for the entire problem domain [30–32]. The second category adjusts the PD force interactions to prevent artificial softening in the boundary nodes due to the skin effect. The energy method [30, 33], the force normalization method [34], the force density method [30, 33, 35], the position-aware peridynamics [36], and the volume method [37] are some examples of them. Le and Bobaru [38] implemented the methods mentioned in the first two categories and demonstrated their performance in reducing skin effects. In their study, both a static problem with homogeneous deformations and an edge crack problem under mode I loading are used. This study shows that any surface correction algorithm improves results significantly compared to uncorrected cases. However, the performance of these methods strongly depends on the deformation type, i.e., homogeneous or uniaxial deformation, and the geometry of the problem. For example, although the fictitious nodes method eliminates the skin effects for cases where the deformation is homogeneous, and the geometry is simple, it results in the highest error in the edge-crack problem among surface correction algorithms used for comparison [38]. Also, this method is not very useful for complex geometries and problems where crack propagation and branching occur.

The third category is one of the main interests of this study. In this category, the skin effects are eliminated using PD parameters obtained in their discrete form [39, 40]. Contrary to common practice, the strain energy density in the PD is first converted to its discrete form and then equated to its counterpart in the CCM. Therefore, the resulting PD constants are obtained in a discrete form for each material point, which takes into account missing neighborhoods and successfully reduces skin effects.

In the middle of the 18th century, it was discovered that some crystalline minerals such as quartz (SiO_2) generate an electric voltage proportional to the applied tension and compression. This phenomenon is named as *piezoelectric effect* meaning that electricity resulted from the pres-

sure, i.e., piezo in Greek. Jacques and Pierre Curie brothers showed experimentally that piezoelectric minerals stretch or shorten according to the applied electric field's polarity. Hence, the *direct* piezoelectric effect refers to the resultant electricity due to applied stresses. On the other hand, the *converse* piezoelectric effect is the resultant change in the dimensions due to induced electric field. Therefore, the piezoelectric effect is a reversible process. This effect is originated from the linear electromechanical coupling between the mechanical and electrical states in crystalline materials with noncentrosymmetry. When a longitudinal compression force is applied to the quartz crystal, it shrinks in the longitudinal direction and elongates in the transverse direction. This deformation results in a shift of the center of the positive charges move downward while the center of the negative charges move upward, resulting in polarization in the downward direction. Polarization in the reverse direction can be obtained if the mechanical force is applied in the transverse direction. Therefore, the electrodes at the top and the bottom surfaces are charged electrostatically, and an electric voltage can be measured in between these electrodes.

Piezoelectricity continued to be studied to describe their crystalline structures under the subject of crystal physics. In 1910, Woldemar Voigt identified the 20 natural crystal classes exhibiting piezoelectric effect and defined the piezoelectric constants using tensor analysis [41]. During World War I and II, piezoelectric materials began to be used practically, such as resonators for an ultrasonic submarine detector [42], filters for radios, and televisions and audio transducers. Today, piezoelectric materials are used in the following areas:

- Piezoelectric sensors. Piezoelectric effect is used in the measurement of pressure, temperature, strain changes. When a piezoelectric sensor is attached to a structure, any force (or deformation) on the sensor creates electric voltage that can be monitored to measure specific property. As an example, ultrasonic transducers equipped with piezoelectric ceramics are used for accurate measuring the viscosity and material constants in fluids and solids. Also, piezoelectric materials are used in echolocation devices in cars help drivers to determine the distance of any object to the car.
- Structural health monitoring in conjunction with the direct effect.
- Piezoelectric actuators. The converse effect is used in manufacturing accurate actuators because piezoelectric materials deform with a predictable amount under an applied electric

field. As an example, a piezoelectric ceramic rod can be manufactured so that it can be used as a piston where axial deformation can be controlled with the applied electric field. This becomes very useful where micro precision and adjustment are required such as positioning lens for microscopes.

- Energy harvesting structures.
- Micro-electro-mechanical systems (MEMS)

The piezoelectric materials are dielectrics, i.e., electric insulators that can be polarized. Also, they intrinsically exhibit an electromechanical coupling with an anisotropic material behavior. Unlike the standard dielectric materials that need an electric field to be polarized, the application of mechanical stresses also causes the polarization of piezoelectric materials, which are not ferroelectric. On the other hand, piezoelectric materials, which are also ferroelectric, have spontaneous electric polarization in their structure even without an applied electric field. Therefore, the crystalline structure of the ferroelectric material governs its piezoelectric effect, and a specific poling process is needed to use them as piezoelectrics. Some ceramics, such as PZT and BaTiO₃, and polymers such as PVDF gain the piezoelectric properties through an electrical polarization process. As a result, these materials exhibit higher piezoelectric coupling coefficients and fracture toughness than their natural counterparts. Typically, an applied electric field of 1 kV/mm to a ferroelectric ceramic can create a linear strain up to 0.002 and vice versa [43]. Therefore, these materials are preferred to use in sensor and actuator applications.

Piezoelectric ceramics are operated at high electrical fields and high mechanical loads, depending on their application purpose as sensors or actuators. For example, the mechanical loads can go up to 50 MPa, close to the material's strength, in an actuator application [43]. In addition, these ceramics are brittle materials with low fracture toughness, making these materials prone to fracture.

Studies for the fracture of piezoelectric materials started in the 1980s. Experiments show that the fracture toughness of the poled piezoelectric ceramics reveals strong anisotropy and dependence on the applied electric field [44–46]. Pisarenko et al. [46] found that the difference in the fracture toughness in the two parallel material planes can reach 20%. However, most of the published data regarding theoretical and experimental studies of fracture behaviour of piezoelectric

materials have shown some contradictions [47]. The experimental contradictions are apparent for different PZT ceramics and fracture test setups, such as compact tension, indentation, three-point bending, different levels of electromechanical loadings, and different types of media within the crack gap, such as air, silicon oil, and NaCl solution. For example, there are different observations on the fracture toughness of the poled PZT material when both poling direction and the electric fields are perpendicular to the crack surface. While many experiments [13, 48–53] show that the positive electric field promotes the crack opening and the negative one impedes it, some of the theoretical studies [54–58] state that an applied electric field impedes the crack growth regardless of its direction. Even a few studies [59–61] claim the opposite of the previous findings and state that the positive electric field impedes the crack growth and vice versa. In addition, the imposition of the electric boundary conditions through the crack faces is another controversial topic in the fracture properties of piezoelectric materials [47, 62, 63]. The most commonly used one is the impermeable electric boundary conditions. This condition assumes that the normal component of the electric displacement is zero along the crack surfaces. Hence, there is no free charge along the surface and no electric field within the crack gap. Another boundary condition used in the literature is electrically permeable. This approach assumes that the electric displacement and potential are continuous across the crack surfaces, which results in free charges at the crack surface. The third approach is called the exact electrical boundary condition, which requires consideration of the finite permittivity of the medium within the crack gap and its corresponding electric displacement.

Standard fracture parameters for the brittle materials such as stress intensity factors and energy release rate may not be sufficient to describe the crack tip because of the electromechanical coupling [47]. Whereas some of the criteria totally neglect the electrical part of the energy release rate and only consider the mechanical energy release rate (MERR [13]), some of them use the total energy release rate (ERR). Although MERR produces the correct influence of the electric field on the crack propagation, it causes a theoretical inconsistency by neglecting the electric field because the piezoelectric coupling requires an electric field at the crack tip. On the other hand, ERR causes that electric field always prevents the crack growth regardless of its direction, which contradicts with the experimental results [64]. The other criteria can be listed as the local energy release rate criterion G_C [65], generalized stress intensity factors utilized with the crack-opening-displacements (CODs) [66] and some phase-field models [67]. Most of the numerical studies use

the impermeable electric boundary conditions together with the MERR fracture criteria.

Gaudenzi and Bathe [68] proposed an iterative finite element procedure for analyzing piezoelectric materials. Although the formulations are based on finite elements, it provides a simple but powerful schematic for obtaining a fully-coupled electromechanical analysis of piezoelectric materials utilizing an iterative procedure. Furthermore, thanks to the iterative nature of the coupling strategy, this formulation can easily be implemented in any nonlinear incremental finite element solver.

Ohs and Aluru [69] studied the meshless analysis of the piezoelectric devices with two different approaches. In the first approach, the governing equations of piezoelectricity are separated into electrical and mechanical systems of equations. Then electric potentials are obtained from the electrical system of equations where the potential values are the only unknown, and the displacement fields are moved to the right-hand side as a forcing term. Similarly, displacement fields are solved from the mechanical system of equations where the electric potential terms are taken as a forcing term on the right-hand side of the equations. Then, they utilize an iterative approach to solve the coupled electromechanical system. However, it is stated that convergence issues may arise from the iterative procedure when the applied electric potential or mechanical forces are high. Hence, they provided a fully-coupled approach to overcome these issues. In this approach, the electric potential and displacement fields are solved implicitly as a single system of equations without any iterations. Finally, both algorithms are tested on the problems with analytical solutions. The results show perfect agreement with the analytical ones.

There is a considerable effort in the literature on the fracture simulations of piezoelectric materials. However, one of the techniques that can overcome the challenges of modeling crack propagation in piezoelectric solids is phase-field modeling. Miehe and his coworkers [70] proposed the phase field formulation and its numerical implementation using FEM in 2010. They provide crack propagation results for compact tension and three-point bending tests and compare the obtained fracture loads for various applied electric fields with the experimental data [13]. They showed that the numerical results agree with the experimental ones with a modified material parameter. Also, crack patterns were provided for the three-point bending test with compact tension and three different notch positions, resulting in a pattern similar to the experimental ones. Mohanty et al. [71] used the proposed phase-field model by Miehe et al. [70] to model crack growth

in functionally graded piezoelectric ceramics. In addition to homogenous PZT-4, a composite piezoelectric ceramic composed of PZT-4 and BaTiO₃ is used in the several mode-one and mixed-mode fracture simulations. They also studied how the fracture load is affected by the presence and arrangement of holes in piezoelectric ceramics. They conclude that the size of the hole has a higher effect on the decrease in the fracture load than the number of holes. They also found that regardless of the applied electric field's direction and the initial crack's length, the fracture load increases if the material degradation coincides with the polarization direction. Sridhar and Keip [72] also used the phase-field model developed by Miehe et al. [70] and investigated different crack electric boundary conditions, such as permeable, impermeable, and semi-permeable cracks in two- and three-dimensional settings. Another phase-field model to capture fracture in piezoelectric ceramics was introduced by Wilson et al. [73].

In addition to phase-field models, various finite element models are available in the literature regarding fracture modeling of piezoelectric materials. Linder et al. [74] present new finite elements with embedded strong discontinuities and show that the new finite elements were successfully verified against the compact tension and three-point bending experiments presented by Park and Sun [13]. Jański and Kuna [75] propose an adaptive finite element modeling of stationary and propagating cracks in the piezo structures. Unlike the previous study, this work considers the dependence of fracture toughness on the applied electric field. However, they conclude that the effect of the electric field on the mechanical fracture toughness can be ignored during the crack propagation. Another interesting study was published by Wang et al. [76]. They performed impact experiments and conducted finite element analyses with cohesive units to study the dynamic fracture of PZT-5H ceramics. Based on the stress and electric field distribution obtained during the fracture process, an electric breakdown criterion is obtained for an elliptic crack parallel to the applied electric field's direction. A detailed review by Kuna [77] provides more information regarding the finite element analyses of cracks in piezoelectric structures.

The extended finite element method (XFEM) is another widely used numerical technique to study fracture analysis of piezoelectric structures. In 2009, Béchet et al. [78] proposed the new enrichment functions required to define cracks in piezoelectric material for the first time. Later, Bhargava and Sharma [79] used these enrichment functions to calculate the stress intensity factors and energy release rates for center and edge crack problems. Their results confirm the accuracy

and efficiency of the proposed XFEM. Bui and Zhang [80] presents the simulations of stationary dynamic cracks in piezoelectric structures under electromechanical impact loads. They obtain the normalized dynamic intensity factor from their numerical simulations and compare them with those available in the literature. So, they show the accuracy of their numerical results in good agreement with the literature. Another dynamic extended finite element analysis is performed by Liu et al. [81]. Unlike the previous study, the non-homogenous functionally graded piezoelectric materials are subjected to electromechanical impact loads. They also provide an extensive parametric study by investigating the effects of the poling direction, material degradation, impact loads, and more. Liu et al. [82] extended this XFEM of functionally graded piezoelectric structures by including the thermal shock. They obtain that the effects of thermal shock loading on the dynamic intensity factors are apparent. Furthermore, the poling direction and material degradation significantly affect the dynamic intensity factors under thermal shock loading as well as under mechanical and electrical impact loadings. Sharma et al. [83] analyze subinterface cracks in piezoelectric bi-materials using XFEM. Later, this study is extended to investigate the transient analysis of interfacial cracks in dissimilar piezoelectric materials by Yu et al. [84].

The boundary element method (BEM) is another numerical technique used for fracture simulations of piezoelectric solids. In 2008, García-Sánchez et al. [85] proposed a transient dynamic crack analysis of homogeneous piezoelectric solids. Similar to previous studies, they also conclude that the dynamic intensity factors significantly depend on the applied electric field's direction and intensity. Lei et al. [86] successfully simulate the crack propagation in infinite and finite plates using the dual boundary element computer program they developed. In 2015, Bui [87] presented an extended isogeometric analysis (XIGA) for fracture simulations in piezoelectric materials. In this study, the crack growth simulation results are provided in addition to numerical results of static and dynamic fracture parameters. Both static and dynamic intensity factors agree well with the BEM solutions obtained from the literature. Later, this study is extended to cover the dynamic fracture modeling of magneto-electroelastic composite materials by Bui et al. [88].

When a dielectric material is subjected to a high voltage that exceeds the material's dielectric strength, it rapidly increases the temperature and conductivity of the material. This process causes permanent damage to the material and electronic device, which is called dielectric breakdown. Raymond et al. [89] studied the dynamic modeling of dielectric breakdown in solid di-

electrics using peridynamics in 2015. Electromechanical coupling is achieved by considering the electrostatic forces. Moreover, their model includes temperature dependence of the conductivity and the degradation of the permittivity due to damage [89]. The thermal diffusion was ignored because the failure happens in a short time. A finite-difference solver is adopted to find the electrostatic potentials, and their effect on the displacement field is obtained through the Lorentz and Kelvin forces. However, the effects of the deformation on the electrostatic potential field are not considered. Their study clearly shows the effect of the applied voltage on the specimen and the resulting damage pattern. Also, rapid degradation of the material is observed when the effect of temperature-conductivity coupling is increased.

Traditionally, carbon or glass microfibers have been used in composites to enhance polymeric materials' mechanical, electrical, and thermal properties [90]. Recently, it has been shown that using a few weight percent of nanofillers as a reinforcing material in the polymers results in significant changes in these composites' mechanical, thermal, and electrical properties [91–93]. Carbon nanotubes (CNTs) are the most common nanofillers that have been used and studied due to their extraordinary strengths and high thermal conductivity [90]. On the other hand, CNTs have a pretty unusual behavior for electrical conductivity. Depending on their atomic structures, they can be either a semiconductor or conductors [90].

In 2016, Naveen and Seidel [94] proposed a formulation for electromechanical Peridynamics to model the piezoresistive response of carbon nanotube nanocomposites. The piezoresistive effect describes the change in the electrical resistivity, or resistance to an electric current, of material under the application of mechanical strains. As opposed to the piezoelectric effect, where mechanical strain causes an electric potential, the piezoresistive effect results in a change only in the electric resistance of that material. In this study [94], the electric conduction equations are formulated using the Peridynamic heat conduction equations proposed by Bobaru and Monchai [95, 96]. Furthermore, the electron hopping phenomenon is included in the proposed formulation. Hence, they demonstrated the capability of peridynamics to model the coupling between deformation and electron hopping, a significant source of the piezoresistive response. A detailed investigation has been done on the relationship between conductivity, piezoresistivity, and volume fraction of CNTs. Later same authors used their formulations to model the strain and damage sensing in nanocomposite bonded explosive materials (NCBX) [97–99]. The key idea is that by monitoring

the piezoresistive response of the explosive material bonded with the CNT, it can be understood whether micro-damage is present in the explosive composite. Thus, accidental explosions caused by microstructural damage in explosives can be prevented.

Diana and Carvelli [100] proposed a micropolar peridynamic formulation to model the in-plane electromechanical behavior of isotropic conductive brittle solids. An interaction between two material points consists of a mechanical normal, shear, and rotational springs and a conductive bond to define the electrical conduction equations in their model. As in Naveen and Seidel's studies [94, 98], the bonds whose stretch values exceed a known ultimate value, i.e., broken bonds, are not allowed to conduct the electric field. In addition, the fracture process is not influenced by the electric field. The results of this study [100] show that the proposed model is successful in predicting the electric potential and current density for electromechanical problems, including fracture and piezoresistive response.

Roy and Roy [101] proposed the flexoelectric peridynamics for the first time. The constitutive equations are written for isotropic centrosymmetric flexoelectric and exhibit electromechanical coupling. Unlike the previous studies, they used the correspondence state-based peridynamics model in conjunction with the phase-field theory.

In 2021, Vieira and Araújo [102] extended the implicit non-ordinary state-based formulation Breitenfeld et al. [103] initially proposed to linear piezoelectricity problems. Several static problems were solved to verify the proposed model. The peridynamic solutions for displacement and electric fields were compared with the analytical results or the FEM results whenever the analytical solution was unavailable. In addition, the convergence of the results was tested for different horizon sizes. Their results agree very well with the reference solutions in most cases. However, displacement fields exhibit strong oscillation near the clamped boundaries.

1.3 Problem Statement and Significance

Although there is a Poisson ratio restriction in the BB-PD model, it still serves as a powerful tool to solve challenging engineering problems with a relatively cheap computational cost. If the Poisson ratio of the material does not deviate from the ones that BB-PD can model, it becomes advantageous to use the BB-PD compared to other PD models in terms of computational cost and

simplicity. Therefore, this study focuses on improving the BB-PD model without adding additional degrees of freedom to the model. Instead, the calculation of the PD material parameters is enhanced to improve the results of the BB-PD simulations. However, it is essential to note that when the simulation involves fracture, new boundaries will form as the cracks propagate and branch. As a result, additional material points will suffer from the skin effect due to the missing neighbors. Therefore, the correction algorithm should also be able to make the necessary corrections for these newly created boundaries.

Although piezoelectric ceramics have high stiffness compared to their natural counterparts and can be used efficiently in smart structures, they are brittle with an ultimate tensile strength smaller than 100 MPa and have low fracture toughness ($0.5 - 2.0 \text{ MPa}\sqrt{\text{m}}$) [104]. In addition, damage can occur either by electric breakdown or mechanical failure under concentrated stresses and electric fields. Therefore, analyzing the damage and fracture processes in piezoelectric components is crucial, considering the electromechanical coupling. Various experimental, theoretical, and numerical studies focus on the damage in piezoelectric materials. However, theoretical studies are limited to simple crack and geometrical configurations.

Peridynamics and its meshless discretization have several advantages over their counterparts as CCM and Finite Element Method (FEM) or Extended-FEM (XFEM) based on CCM. However, there is a very limited number of studies in peridynamics related to modeling this specific class of materials. Furthermore, as the technological devices become smaller and smarter with increasing energy demand, it is more likely to use piezoelectric materials in our daily life in the near future. Therefore, it is increasingly important to learn more about piezoelectric materials' damage and cracking mechanisms to operate them safely.

1.4 Objectives and Outline

This thesis aims to propose:

1. a surface correction method for the bond-based peridynamics to decrease the surface effects by considering the newly emerging boundaries,
2. an implicit formulation within the non-ordinary state-based peridynamics for linear piezoelectricity that can capture the fully coupled electromechanical behavior of the material, and

3. an iterative solution procedure for modeling the electromechanical crack propagation within the transversely isotropic piezoelectric ceramics.

The first chapter of this thesis outlines the background information and literature review regarding the peridynamic theory and linear piezoelectricity. Then, the motivation and objectives of this study are stated. The second chapter presents the proposed discrete surface correction method, and several numerical examples are provided to test the performance of the proposed correction method. These examples include the static analysis under homogenous deformation and dynamic crack propagation resulting from the brittle failure. Then, the third chapter introduces the non-ordinary state-based peridynamic (NOSB-PD) formulation for linear piezoelectricity. The tangent stiffness matrix of the electromechanical system is obtained using a perturbation technique and used for solving various static problems. The numerical examples provided in this chapter show the capability of the NOSB-PD for the analysis of piezoelectric materials subjected to mechanical and electrical loading with various boundary conditions. The fourth chapter continues with the fracture modeling of piezoelectric ceramics. An iterative solution procedure is utilized to simulate the mode-I fracture of the pre-notched under an applied electric field. Finally, the fifth section summarizes the conclusions and presents the future perspectives and direction of this study.

CHAPTER 2

BB-PD WITH A NEW SURFACE CORRECTION METHOD

2.1 Bond-Based Peridynamic Model

This section provides a brief description of bond-based peridynamics. Also, discretized equations used in the numerical simulations are discussed in the following sections. As a notation, vectors are denoted in bold face letters, tensors in open-faced capitals, and scalars in lowercase letters.

2.1.1 A brief description of bond-based peridynamics

In a PD body, each material point at \mathbf{x} interacts with other material points at \mathbf{x}' within its neighborhood, $\mathcal{H}_{\mathbf{x}}$. This region corresponds to a disk having a radius of the horizon, δ , and centered at \mathbf{x} in two dimensional space. In BB-PD, internal forces within a PD body are treated as a network of pairwise interactions that can be pictured as spring forces [105].

A *bond*, ξ , corresponds to the relative position vector between two material points whose positions are \mathbf{x} and \mathbf{x}' in the reference configuration as shown in Fig. 2.1. For a given displacement field, \mathbf{u} , the relative position of these particles in the deformed configuration can be named as *deformed bond* and becomes $\xi + \eta$, where η is the relative displacement vector:

$$\xi = \mathbf{x}' - \mathbf{x}, \quad (2.1a)$$

$$\eta = \mathbf{u}(\mathbf{x}', t) - \mathbf{u}(\mathbf{x}, t). \quad (2.1b)$$

The equation of motion for a material point \mathbf{x} is written as [2]:

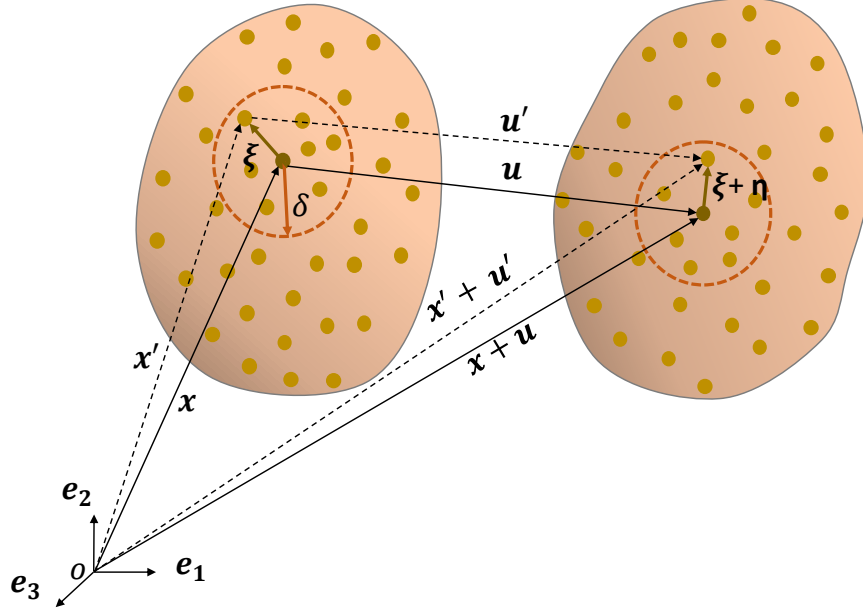


Figure 2.1: A PD body in the reference (left) and deformed (right) configurations

$$\rho(\mathbf{x}) \ddot{\mathbf{u}}(\mathbf{x}, t) = \int_{\mathcal{H}_{\mathbf{x}}} \mathbf{f}(\eta, \xi, t) dV_{\mathbf{x}'} + \mathbf{b}(\mathbf{x}, t) \quad (2.2)$$

where $\rho(\mathbf{x})$, $\ddot{\mathbf{u}}(\mathbf{x}, t)$ and $\mathbf{b}(\mathbf{x}, t)$ are the mass density, acceleration and prescribed body force density at the material point \mathbf{x} at time t , respectively. The *pairwise force density*, \mathbf{f} , is the force per unit volume squared that the material point \mathbf{x}' exerts on \mathbf{x} . The force density depends on constitutive and damage models.

Linear elastic material model for PD solids, named as *prototype micro-elastic brittle (PMB) material* [2, 19], is used in the present study. In this model, force density between two material points linearly depends on the relative elongation of the bond and acts in the direction of the deformed bond. Furthermore, a damage model can be incorporated in the material model. Hence, the pairwise force density can be written as [19]:

$$\mathbf{f}(\eta, \xi, t) = \mu(\xi, t) c(|\xi|) s \frac{\xi + \eta}{|\xi + \eta|} \quad (2.3)$$

where $\mu(\xi, t)$ is a history dependent damage function, $c(|\xi|)$ is the micromodulus, and s is called *stretch*, which is the relative elongation of the bond. For a brittle material, the damage function can be defined such that a bond cannot sustain any load after the bond stretch exceeds a pre-defined

value [19]:

$$\mu(\xi, t) = \begin{cases} 1, & \text{if } s(\xi, t') < s_0 \text{ for all } 0 \leq t' \leq t \\ 0, & \text{otherwise} \end{cases} \quad (2.4)$$

where s_0 is called the *critical bond stretch* for bond failure.

Therefore, an irreversible damage is nucleated when the bond stretch exceeds the critical one. Since the broken bond cannot contribute to the load carrying capacity of the material, the forces carried by neighboring bonds begin to increase and the damaged material points become weaker than undamaged material points. Hence, the damage at a material point \mathbf{x} at time t can be defined as:

$$D(\mathbf{x}, t) = 1 - \frac{\int_{\mathcal{H}_{\mathbf{x}}} \mu(\xi, t) dV_{\mathbf{x}'}}{\int_{\mathcal{H}_{\mathbf{x}}} dV_{\mathbf{x}'}}. \quad (2.5)$$

The local damage at a material point given in Eq. (2.5) can have any value between zero and one. Zero corresponds no damage at the material point \mathbf{x} , and one corresponds each bond that was initially connected to point \mathbf{x} are broken, resulting in full damage at that point.

As can be seen from the formulations, PD does not include any additional information to guide crack initiation, propagation, and direction. Therefore, it is said that crack growth in PD is autonomous [106].

The evaluation of the PD parameters such as the bond constant called *micromodulus*, $c(|\xi|)$, and the critical stretch, s_0 , are given in Section 3.

2.1.2 Discretization of BB-PD equations

The 2D domain is first divided by a uniform grid, and each cell center is called a *node*. Then, a discrete version of the Eq. (2.2) is written for node i as following:

$$\rho_i \frac{d^2 \mathbf{u}(\mathbf{x}_i, t)}{dt^2} = \sum_{j \in \mathcal{F}_i} \mathbf{f}(\mathbf{u}(\mathbf{x}_j, t) - \mathbf{u}(\mathbf{x}_i, t), \mathbf{x}_j - \mathbf{x}_i) V_j^{(i)} + \mathbf{b}(\mathbf{x}_i, t) \quad (2.6)$$

where \mathcal{F}_i represents the family of node i , and $V_j^{(i)}$ is the volume of the node j associated with the neighborhood of node i , named as partial volumes.

To improve the partial volume approximation in the meshless discretization, PA-HHB algorithm [21] is used in this study. According to this algorithm, the family of node i is defined as:

$$\mathcal{F}_i := \{j \neq i \quad : \quad \mathbf{x}_j \in \Omega; \quad \|\mathbf{x}_j - \mathbf{x}_i\| - \frac{h}{2} \leq \delta\} \quad (2.7)$$

where h is the uniform grid size, and the δ is the horizon. Algorithm 1 describes the procedure for partial volume calculation in [21].

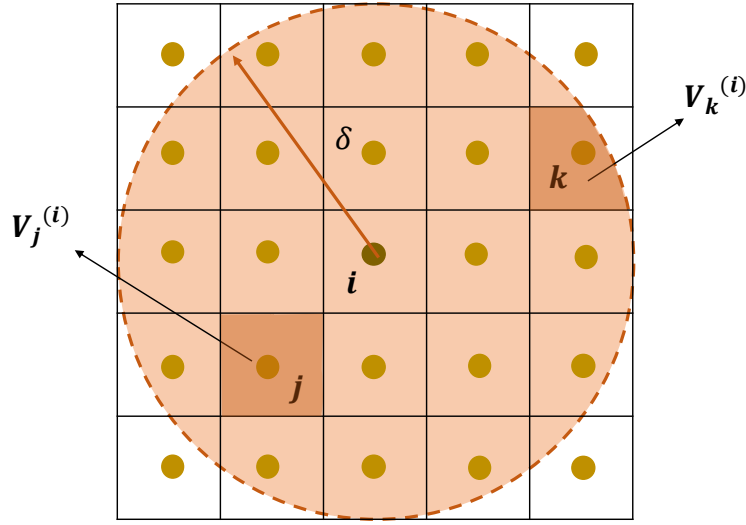


Figure 2.2: Partial areas

Algorithm 1 PA-HHB [21]

- 1: Calculate the bond length between node i and node j
 - 2: $|\xi| = |\mathbf{x}_j - \mathbf{x}_i|$
 - 3: Check if node j is a family node for node i and using Eq. (2.7)
 - 4: **if** $|\xi| \leq \delta - \frac{h}{2}$ **then**
 - 5: $V_j^{(i)} = bh^2$ $\triangleright b$ is the thickness of the plate
 - 6: **else if** $|\xi| \leq \delta + \frac{h}{2}$ **then**
 - 7: $V_j^{(i)} = \left[\frac{1}{h} \left(\delta + \frac{h}{2} - |\xi| \right) \right] bh^2$
 - 8: **else**
 - 9: $V_j^{(i)} = 0$
 - 10: **end if**
-

Half-step central differences time integration scheme [107, 108] is applied for the time discretization. A stable time step for the PMB material can be calculated by [19]:

$$\Delta t < \sqrt{\frac{2\rho}{\sum_j (c(|\xi|)/|\xi|) V_j^{(i)}}} \quad (2.8)$$

where ρ is the density, j is an iterator for all neighbors of the material point i , and $V_j^{(i)}$ is the partial volume described in Algorithm 1.

In the numerical calculation, the minimum Δt calculated for all material points in the problem domain is selected, and a safety factor smaller than 1 is applied to obtain the critical time step for the stability of the explicit solution. The details of the explicit time integration scheme are given in Algorithm 2.

Algorithm 2 Half-step central differences time integration scheme [106]

- 1: Initialization: $n = 0, t = 0, \mathbf{u} = 0$ and $\ddot{\mathbf{u}} = 0$, where n is the time counter
 - 2: Time updates: $t^{n+1} = t^n + \Delta t$ and $t^{n+\frac{1}{2}} = \frac{1}{2}(t^n + t^{n+1})$
 - 3: First partial velocity update: $\dot{\mathbf{u}}^{n+\frac{1}{2}} = \dot{\mathbf{u}}^n + (t^{n+\frac{1}{2}} - t^n) \ddot{\mathbf{u}}$
 - 4: Velocity boundary conditions are assigned by setting $\dot{\mathbf{u}}^{n+\frac{1}{2}}$ with prescribed values to the corresponding nodes
 - 5: Displacement update: $\mathbf{u}^{n+1} = \mathbf{u}^n + \Delta t \dot{\mathbf{u}}^{n+\frac{1}{2}}$
 - 6: Evaluate internal forces \mathbf{f}_{int}^{n+1} using Eq. (2.3) with updated displacement and velocity values
 - 7: Compute acceleration: $\ddot{\mathbf{u}}^{n+1} = \mathbf{M}^{-1} (\mathbf{f}_{int}^{n+1} + \mathbf{f}_{ext}^{n+1})$, where \mathbf{f}_{ext} is the applied (external) body forces per volume
 - 8: Second partial velocity update: $\dot{\mathbf{u}}^{n+1} = \dot{\mathbf{u}}^{n+\frac{1}{2}} + (t^{n+1} - t^{n+\frac{1}{2}}) \ddot{\mathbf{u}}^{n+1}$
 - 9: Update time counter: $n \leftarrow n + 1$
 - 10: If simulation is not complete, go to *step 2*.
-

2.2 Discrete Surface Correction Method

The proposed correction method includes the re-evaluation of the micromodulus and associated bond breakage criteria to reduce the skin effects. For this purpose, parameters c and s_0 are calculated discretely in the numerical simulation. If the simulation involves fracture, new boundaries will emerge as the crack propagates, and the required correction can be conducted by evaluating the c and s_0 through the simulation.

For the sake of completeness, the analytical calculation of the c and s_0 are first presented in the following sections. Then, the proposed surface correction method, which consists of the discrete calculation of the material parameters, is explained in detail.

2.2.1 Determination of PD micromodulus

Assuming the micromodulus is a constant function and excluding the time and history dependent damage function for simplicity, Eq. (2.3) can be written as:

$$\mathbf{f}(\boldsymbol{\eta}, \boldsymbol{\xi}) = c s \frac{\boldsymbol{\xi} + \boldsymbol{\eta}}{|\boldsymbol{\xi} + \boldsymbol{\eta}|} \quad (2.9)$$

where $\boldsymbol{\xi}$, $\boldsymbol{\eta}$, c and s are the relative position vector (bond), the relative displacement vector, constant micromodulus and stretch, respectively. Eq. (2.1) defines the bond and the relative displacement vector. The stretch of the bond is given as:

$$s = \frac{|\boldsymbol{\xi} + \boldsymbol{\eta}| - |\boldsymbol{\xi}|}{|\boldsymbol{\xi}|} = \frac{e}{|\boldsymbol{\xi}|} \quad (2.10)$$

where $|\boldsymbol{\xi}|$, $|\boldsymbol{\xi} + \boldsymbol{\eta}|$ and e are the magnitude of the reference (undeformed) bond vector, magnitude of the deformed bond vector (can be seen in Fig. 2.3), and bond elongation, respectively. The bond stretch, s , is a nonlinear function of relative displacement vector $\boldsymbol{\eta}$. Assuming small deformations $|\boldsymbol{\eta}| \ll 1$, the pairwise force density function in Eq. (2.9) can be linearized. After expanding the Taylor series for Eq. (2.9) around $|\boldsymbol{\eta}| = 0$ and ignoring the higher order terms, the linearized force-displacement equation is obtained as [97]:

$$\mathbf{f}(\boldsymbol{\eta}, \boldsymbol{\xi}) = c \frac{\boldsymbol{\eta}_n}{|\boldsymbol{\xi}|} \frac{\boldsymbol{\xi}}{|\boldsymbol{\xi}|} \quad (2.11)$$

where η_n is the component of the relative displacement vector in the direction of the undeformed bond ξ .

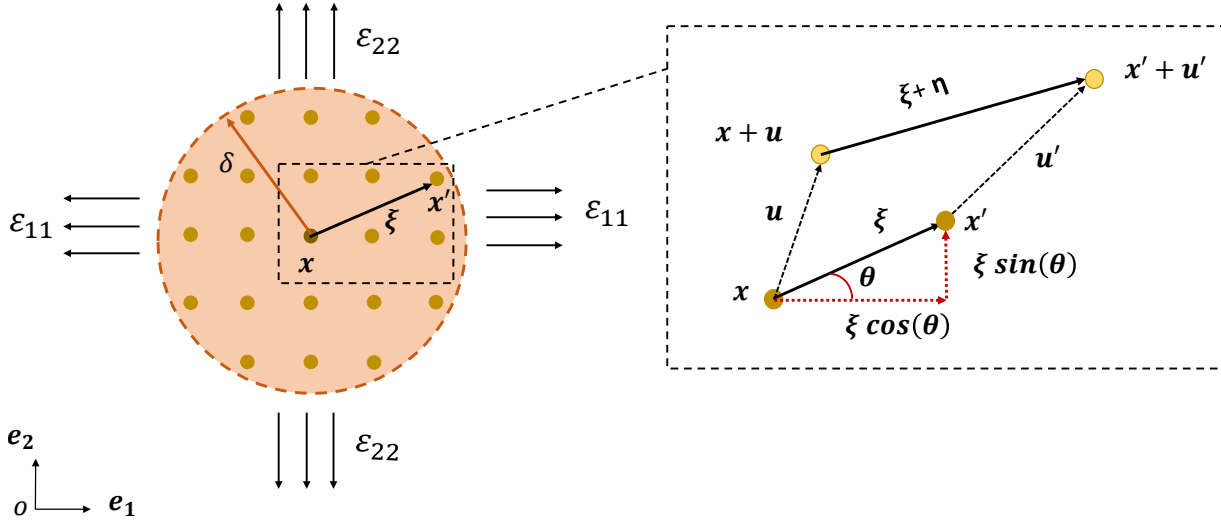


Figure 2.3: PD body under a prescribed strain field (left) and the resulting deformation of the bond ξ (adopted from [97])

Fig. 2.3 shows an isotropic homogeneous body under prescribed bi-axial strain field ϵ_{11} and ϵ_{22} . Under these loading conditions, the deformed bond can be obtained using the deformation gradient tensor \mathbb{F} with the assumption of small strains as follows:

$$\xi + \eta = \mathbb{F}\xi = \begin{bmatrix} \epsilon_{11} + 1 & 0 \\ 0 & \epsilon_{22} + 1 \end{bmatrix} \begin{Bmatrix} |\xi| \cos(\theta) \\ |\xi| \sin(\theta) \end{Bmatrix} \quad (2.12)$$

which results in the relative displacement vector as:

$$\eta = \begin{Bmatrix} \epsilon_{11} |\xi| \cos(\theta) \\ \epsilon_{22} |\xi| \sin(\theta) \end{Bmatrix}. \quad (2.13)$$

Hence, the component of the relative displacement vector in the direction of the bond can be calculated using dot product:

$$\eta_n = \eta \cdot \mathbf{e}_n = \begin{Bmatrix} \epsilon_{11} |\xi| \cos(\theta) \\ \epsilon_{22} |\xi| \sin(\theta) \end{Bmatrix} \cdot \begin{Bmatrix} \cos(\theta) \\ \sin(\theta) \end{Bmatrix} = |\xi| (\epsilon_{11} \cos^2(\theta) + \epsilon_{22} \sin^2(\theta)). \quad (2.14)$$

In order to determine the micromodulus, strain energy densities calculated from classical continuum mechanics (CCM) and PD are equated under the same loading conditions. According to CCM, the strain energy for plane stress conditions is:

$$U^{CCM}(\mathbf{x}) = \frac{E}{2(1-\nu^2)} (\varepsilon_{11}^2 + \varepsilon_{22}^2) + \frac{E\nu}{1-\nu^2} \varepsilon_{11} \varepsilon_{22}. \quad (2.15)$$

where E is the elastic modulus and ν is the Poisson's ratio of the material. For $\varepsilon_{11} = \varepsilon_{22} = \varepsilon$, the Eq. (2.15) becomes;

$$U^{CCM}(\mathbf{x}) = \frac{E}{1-\nu} \varepsilon^2. \quad (2.16)$$

In PD, the strain energy density stored at a material point \mathbf{x} can be calculated as [38]:

$$U^{PD}(\mathbf{x}) = \frac{1}{2} \int_{\mathcal{H}_x} \frac{1}{2} f(\eta, \xi) e \, dV_{\mathbf{x}'} = \frac{1}{4} \int_{\mathcal{H}_x} c \frac{\eta_n^2}{\xi} \, dV_{\mathbf{x}'} \quad (2.17)$$

where $\xi = |\xi|$. Because each bond connects two material points, the strain energy at a single material point is half of the energy stored in the bond. Assuming the complete neighborhood (please see Eq. (2.7)), \mathcal{H}_x , Eq. (2.17) can be written in polar coordinates as:

$$U^{PD}(\mathbf{x}) = \frac{1}{4} b \int_0^{2\pi} \int_0^\delta c (\varepsilon_{11} \cos^2(\theta) + \varepsilon_{22} \sin^2(\theta))^2 \xi^2 \, d\xi \, d\theta \quad (2.18)$$

where b is the thickness of the plate. For $\varepsilon_{11} = \varepsilon_{22} = \varepsilon$, Eq. (2.18) result in:

$$U^{PD}(\mathbf{x}) = \frac{c\pi b\delta^3}{6} \varepsilon^2. \quad (2.19)$$

After equating Eqs. (2.16) and (2.19), the constant micromodulus under plane stress conditions can be obtained as:

$$c = \frac{6E}{(1-\nu)\pi b\delta^3}. \quad (2.20)$$

2.2.2 Discrete calculation of the micromodulus

Instead of using Eq. (2.20), the value of micromodulus, i.e. bond constant, can be computed numerically in the simulation progress considering the missing neighborhood due to problem boundaries or new boundaries created from the crack propagation.

For this purpose, the integral expression given in Eq. (2.17) is first converted to a Riemann sum and equated with its counterpart in CCM. A stress ellipsoid approach which is also used by Madenci [30] can be utilized. The procedure can be summarized as:

1. The values of micromodulus are found by equating the strain energy densities from CCM and PD for two loading cases, which are uniaxial tension in x and y-directions in 2D.
2. An ellipse is drawn whose radii are the values of micromodulus found from the first step.
3. The value of the micromodulus for a bond is obtained by intersecting the bond vector to the ellipse.

For a uniaxial loading case in 2D, the principle strains can be expressed as:

$$\varepsilon_{11} = \frac{\sigma}{E} = \varepsilon, \quad \varepsilon_{22} = -\frac{\nu}{E}\sigma = -\nu\varepsilon. \quad (2.21)$$

Substituting Eq. (2.21) into Eq. (2.15), the strain energy density can be obtained using:

$$U_{uniaxial}^{CCM} = \frac{E}{2}\varepsilon^2. \quad (2.22)$$

Equating the strain energy density in CCM and PD given in Eqs. (2.21) and (2.17), respectively:

$$U(\mathbf{x}) = \frac{E}{2}\varepsilon^2 = \frac{1}{4} \int_{\mathcal{H}_x} c \frac{\eta_n^2}{\xi} dV_{\mathbf{x}'} \quad (2.23a)$$

$$\frac{E}{2}\varepsilon^2 = \frac{1}{4} \sum_{j \in \mathcal{F}_i} c \frac{\eta_n^2}{\xi} V_j^{(i)} \quad (2.23b)$$

where \mathcal{F}_i is family nodes inside the neighborhood of the point i , the component of the relative displacement vector in the direction of bond, η_n , can be found from Eq. (2.14) when the uniaxial loading is in x -direction:

$$\eta_n = |\xi| (\varepsilon_{11} \cos^2(\theta) + \varepsilon_{22} \sin^2(\theta)) \quad (2.24)$$

$$= |\xi| (\varepsilon \cos^2(\theta) + (-\nu\varepsilon) \sin^2(\theta)) \quad (2.25)$$

which results in the discrete form of the bond constant as:

$$c_{(x)(i)} = 2E \left(\sum_{j \in \mathcal{F}_i} |\xi| (\cos^2(\theta) - \nu \sin^2(\theta))^2 V_j^{(i)} \right)^{-1}. \quad (2.26)$$

Similarly, if the uniaxial loading is in y -direction, the component of the relative displacement vector in the direction of bond becomes:

$$\eta_n = |\xi| (\varepsilon_{11} \cos^2(\theta) + \varepsilon_{22} \sin^2(\theta)) \quad (2.27)$$

$$= |\xi| ((-\nu\varepsilon) \cos^2(\theta) + \varepsilon \sin^2(\theta)) \quad (2.28)$$

which results in the discrete form of the bond constant as:

$$c_{(y)(i)} = 2E \left(\sum_{j \in \mathcal{F}_i} |\xi| (-\nu \cos^2(\theta) + \sin^2(\theta))^2 V_j^{(i)} \right)^{-1}. \quad (2.29)$$

In the BB-PD, the forces acting on material points i and j are in the same magnitude but opposite in direction acting along the same line, i.e. $\mathbf{f}_{ij} = -\mathbf{f}_{ji}$. Therefore, both linear and angular momenta are conserved. Similarly, to satisfy the linear and angular momenta, the average bond constants calculated for each bond that connects material points i and j can be used as the effective bond constants for each loading cases (i.e. uniaxial tension in x and y directions) such that:

$$\bar{c}_{(x)(i)(j)} = \frac{c_{(x)(i)} + c_{(x)(j)}}{2}, \quad \bar{c}_{(y)(i)(j)} = \frac{c_{(y)(i)} + c_{(y)(j)}}{2} \quad (2.30)$$

where $\bar{c}_{(x)(i)(j)}$ and $\bar{c}_{(y)(i)(j)}$ are the effective bond constants when the applied uniaxial tension is in x and y directions, respectively. These two effective bond constants correspond to the radius of the ellipse that is constructed to find the effective bond constant for a single bond. Then, the intersection of the ellipse and the relative position vector results in the effective bond constant as:

$$c_{(i)(j)} = \sqrt{(n_x \cdot \bar{c}_{(x)(i)(j)})^2 + (n_y \cdot \bar{c}_{(y)(i)(j)})^2} \quad (2.31)$$

where n_x and n_y are components of the unit direction of bond vector, i.e.:

$$n_x = \cos \theta = \frac{\xi_x}{\xi}, \quad \text{and} \quad n_y = \sin \theta = \frac{\xi_y}{\xi}. \quad (2.32)$$

Hence, the micromodulus can be obtained for the nodes that do not have the complete neighborhood and significantly reduce the skin effects. However, if there is any damage at the material points i and j , Eq. (2.31) can be rewritten as:

$$c_{ij} = \phi \sqrt{(n_x \cdot \bar{c}_{(x)(i)(j)})^2 + (n_y \cdot \bar{c}_{(y)(i)(j)})^2} \quad (2.33)$$

where ϕ is named as degradation parameter, which is defined as the highest damage between the material points i and j at time t :

$$\phi = 1 - \max(D(\mathbf{x}_i, t), D(\mathbf{x}_j, t)) \quad (2.34)$$

2.2.3 Determination of PD critical stretch

The fracture energy, G_0 , can be defined as the energy per crack surface which is required to separate the body into two [109]. In a PD body, the bonds whose stretch value exceeds the critical stretch value, s_0 , is broken, and successive breakage of the bond forms a crack line. Therefore, the relationship between the fracture energy and work required to break the bonds per unit crack length provides an expression for the s_0 . In BB-PD, the fracture energy can be obtained as [109]:

$$G_0 = 2b \int_0^\delta \int_z^\delta \int_0^{\cos^{-1}\left(\frac{z}{\xi}\right)} \left(\frac{1}{2} \cdot c \cdot s_0^2 \cdot \xi\right) \xi d\theta d\xi dz \quad (2.35)$$

where the integration limits are shown in Fig. 2.4.

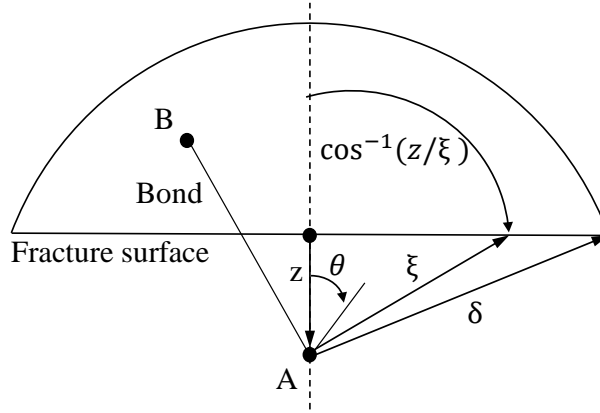


Figure 2.4: Evaluation of fracture energy (adopted from [109])

Under plane-stress conditions, analytical integration of Eq. (2.35) for a constant micro-modulus given in Eq. (2.20) with $\nu = 1/3$ results in a critical stretch value as:

$$s_0 = \sqrt{\frac{4\pi G_0}{9E\delta}}. \quad (2.36)$$

2.2.4 Discrete calculation of the critical stretch

Fig. 2.5 illustrates uniformly distributed PD nodes with a crack. 2.5. The work required to break the nodes on the green dotted line shown in Fig. 2.5 will be calculated. Let us set the horizon to 3.5 times grid spacing. So, the nodes on the green line, whose distance is smaller than the horizon, are of interest because there is no bond passing through the crack line far from the horizon.

Fig. 2.6 shows only half of the broken bonds to prevent confusion and simplify the drawing. One grid space below the crack line, a node called 'j,' is located on the green dotted line shown in Fig. 2.6a. The node j has its bonds, representing the interactions with the neighbors within its horizon, shown in the blue circle. Due to the existence of the crack, the bonds passing through the crack line need to be broken. Let us call them 'set I.' 'Set I' bonds are plotted in Fig. 2.6a.

In Fig. 2.6b, another node 'j' is shown two grid spaces below the crack line. It has fewer number bonds passing through the crack line than in the previous case. Let us call the broken nodes 'set II.' Set II bonds are plotted in Fig. 2.6b.

Finally, the node 'j' presented in Fig. 2.6c is located three grid spaces below the crack line.

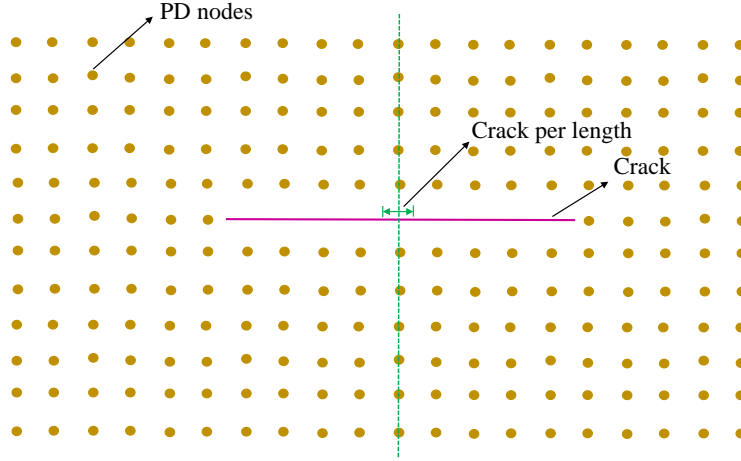


Figure 2.5: PD domain including a crack

As shown in Fig. 6c, it has only three bonds that need to be broken. Let us call them 'set III.'

For the crack configuration shown in Fig.2.5, the procedure to identify the bonds that need to be broken seems straightforward. However, identifying broken bonds can be cumbersome for more complex crack configurations. In addition, even the analytical calculation of the critical stretch value may not be applicable to these cases because the analytical calculation of the critical bond stretch is based on the assumption of a single crack within a neighborhood. In the proposed method, the critical stretch value for a bond connecting material points i and j is discretely calculated in order to consider multiple cracks in a neighborhood and newly formed free surfaces. The discrete critical stretch value will then be used in the bond breakage criteria given in Eq. (2.4). For illustration purposes, the critical stretch value is calculated at a material point i , which corresponds to the energy per unit crack surface which is required to separate the body by generating two free surfaces at that location. Therefore, an imaginary crack line is assumed to pass the material point i , where the discrete s_0 will be calculated, as shown in Fig. 2.7a. The required work to break the bonds passing through this crack line can be computed as discussed in the following paragraphs.

Fig. 2.7 illustrates the procedure used for identifying the bonds that are required to be broken. In Fig. 2.7a, the red dashed line is drawn such that the y-coordinates of the bond vectors are larger than 0.5 grid spacing. Then, the set I bonds, shown in Fig. 2.6a, can be obtained by selecting the bonds passing through the red dashed line. Similarly, the set II bonds can be obtained by drawing the red dashed line at the location where the y-coordinates of bond vectors are larger than 1.5 grid spacing, as shown in Fig. 2.7b. If the bonds passing through this dashed line are

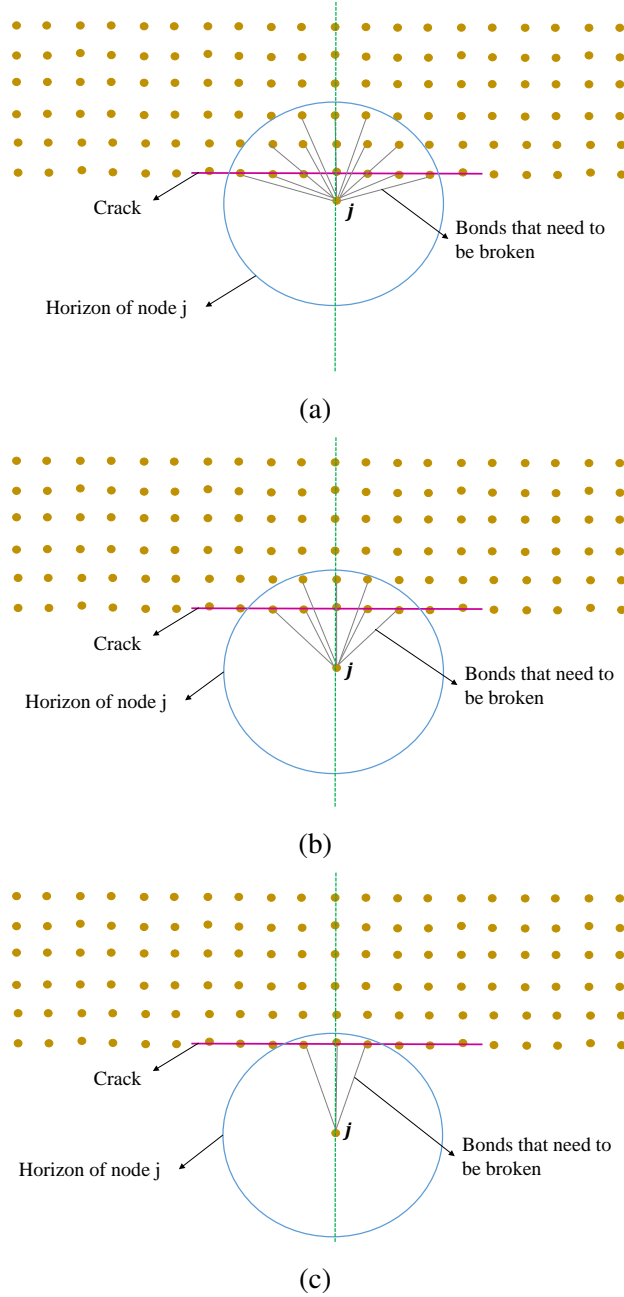


Figure 2.6: Illustration of the broken bonds: (a) set I, (b) set II, and (c) set III

selected, the set II bonds given in Fig. 2.6b are obtained. Lastly, the set III bonds shown in Fig. 2.6c can be obtained by choosing the bonds whose y-coordinate of the bond vector is larger than 2.5 grid spacing as shown in Fig. 2.7c.

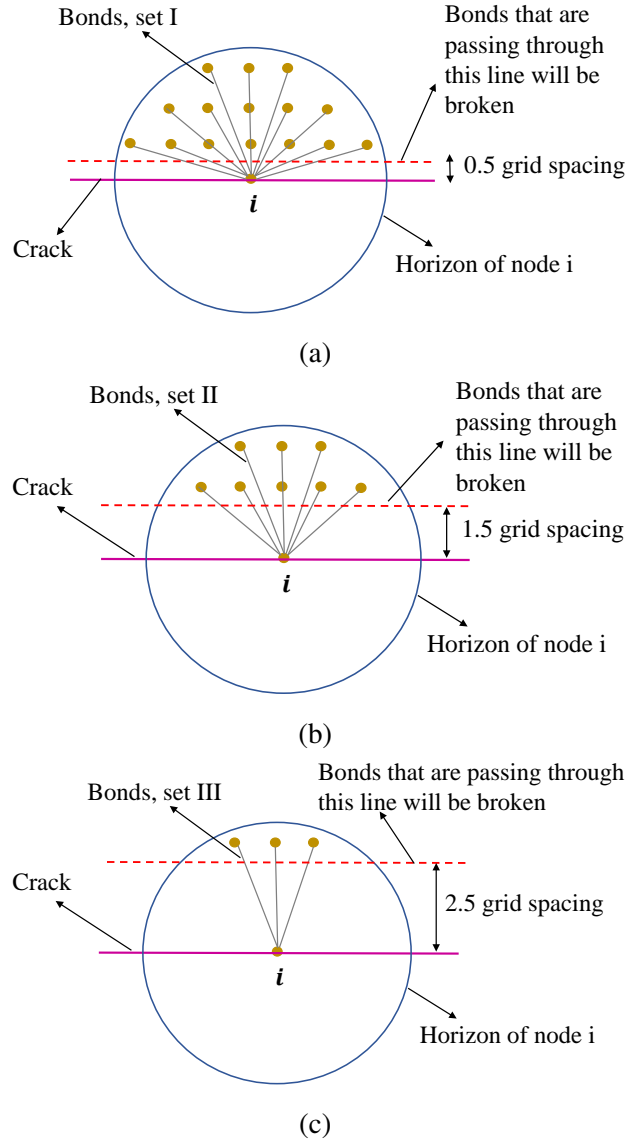


Figure 2.7: Broken bonds used in simplified calculation of the critical stretch discretely, corresponding to (a) set I, (b) set II, and (c) set III

After identifying the bonds that need to be broken, one can sum the strain energies stored in these selected bonds, which results in the work required to break the bonds per unit crack length. The discrete critical stretch value at any material point i can be then computed by equating the fracture energy to the work required to break the bonds per unit crack length, as explained in Algorithm 3. For the bond that connects material points q and r , the critical stretch value can be selected as the critical one, i.e., the minimum s_0 :

$$s_{0,qr} = \min(s_{0,q}, s_{0,r}). \quad (2.37)$$

Algorithm 3 Discrete Critical Stretch Calculation

```

1: procedure CALCULATION FOR CRITICAL STRETCH( $\mathbf{s}_{0,i}$ )
2:    $m = \text{horizon} / h$ , where  $h$  is the uniform grid spacing
3:   for node  $i \leftarrow 1$  to  $N$  do ▷  $N$  is the total number of nodes
4:     summationTerm  $\leftarrow 0.0$ 
5:     for node  $j$ : neighbor node of node  $i$  do
6:        $\xi = \mathbf{x}_j - \mathbf{x}_i$  ▷ bond vector
7:       Calculate the bond constant  $c$  given in Eq. (2.33)
8:       Calculate integration weight,  $V_j^{(i)}$  using Algorithm 1
9:        $i = 0$ 
10:      while  $i < m$  do
11:        if  $|\xi|_y \geq 0.5(2i + 1)h$  then
12:          summationTerm  $+= \frac{1}{4} \cdot c \cdot |\xi| \cdot V_j^{(i)}$ 
13:        end if
14:         $i++$ 
15:      end while
16:    end for
17:     $\mathbf{s}_{0,i} \leftarrow \sqrt{G_0 / (b \cdot \text{summationTerm})}$  ▷ Discrete critical stretch at node  $i$ 
18:  end for
19: end procedure

```

2.3 Numerical Examples

In this section, the results of four benchmark problems are presented and compared with the available results in the literature. An in-house code written in C++ language was developed for peridynamic simulations. The first two problems are solved with an adaptive dynamic relaxation technique (ADR) [30] to obtain the static results, and the remaining two problems are solved with a half-step central difference time integration scheme [108]. The in-house code uses the meshless discretization of the peridynamic equations. In order to improve the numerical integration, PA-HHB algorithm [21] is utilized.

Peridynamic simulation results are obtained with different surface corrections and different horizon sizes. Silling's [37] and Madenci's [30] surface correction methods are used to compare the PD results with the proposed discrete surface correction method. However, these methods only include a correction on the PD micromodulus. For comparison purposes, the PD micromodulus that is obtained by Silling's and Madenci's method is first multiplied with the degradation parameter given in Eq. (2.34) and then used to calculate the discrete critical bond stretch given in Algorithm 3. If a surface correction is not utilized, the analytical values for the peridynamic material parameters given in Eqs. (2.20) and (2.36) are used. Damage contour plots are used to show crack paths in dynamic problems.

2.3.1 A rectangular plate under uniaxial tension

A 0.1×0.05 m plate is subjected to uniaxial tensile stress of 1 MPa, as shown in Fig. 2.8. Young's modulus of the plate, E , is 91 GPa and Poisson's ratio, ν , is used as $1/3$. The uniform grid spacing is fixed to 1×10^{-3} m.

The PD results are compared with the available CCM solution. For this purpose, the absolute relative difference of displacement fields in PD and CCM solutions can be defined as:

$$ARD_x = \frac{|\mathbf{u}_x^{PD} - \mathbf{u}_x^{CCM}|}{|\mathbf{u}_x^{CCM}|} \quad (2.38a)$$

$$ARD_y = \frac{|\mathbf{u}_y^{PD} - \mathbf{u}_y^{CCM}|}{|\mathbf{u}_y^{CCM}|} \quad (2.38b)$$

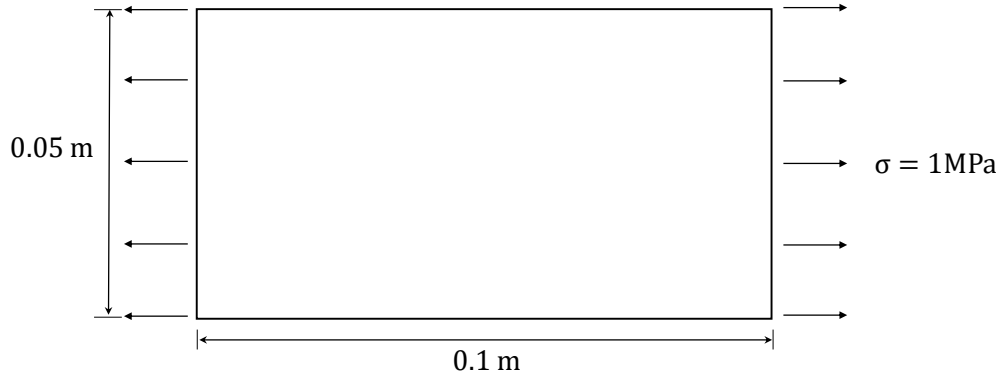


Figure 2.8: Problem setup: A plate under uniaxial tension

where ARD_x and ARD_y are the absolute relative differences of horizontal and vertical displacement fields, respectively.

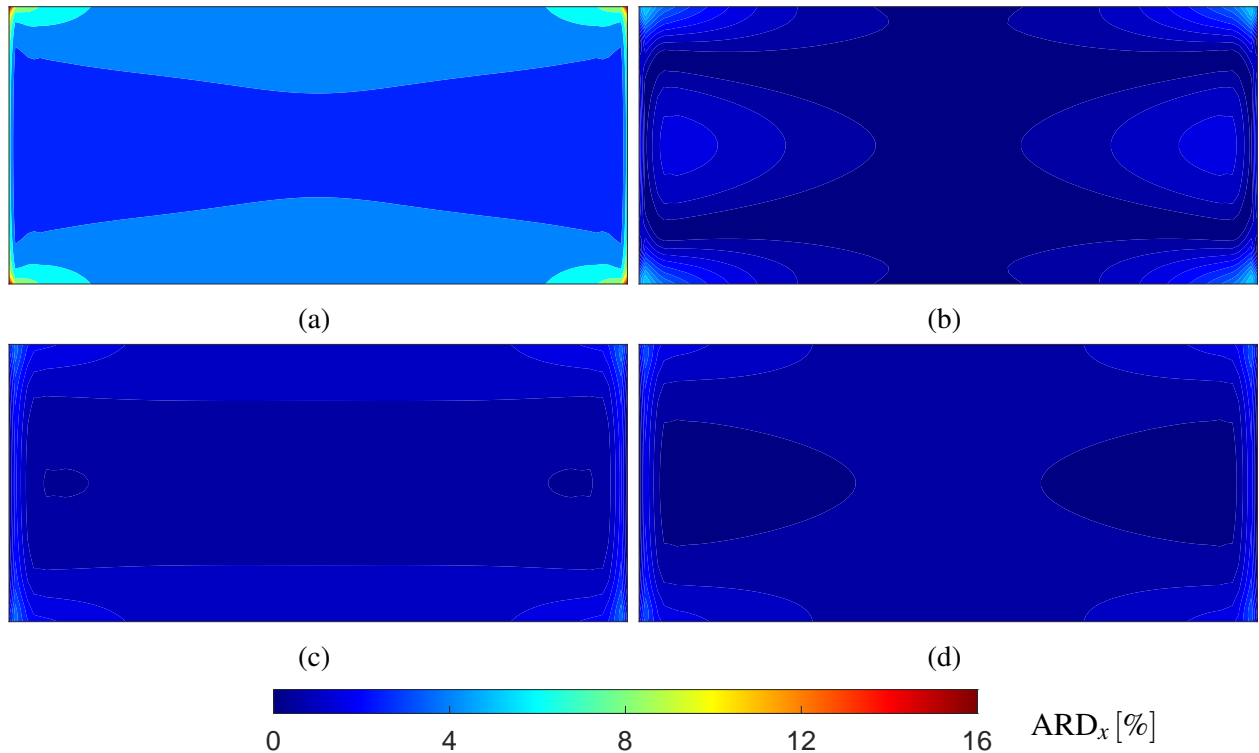


Figure 2.9: Contour plots for absolute relative difference [%] of x-displacements in CCM and PD results with (a) no correction, (b) Silling's, (c) Madenci's, and (d) discrete surface correction methods, 100×50 , $\delta = 5h$

Fig. 2.9 shows the distribution of absolute relative difference of x-displacements in CCM and PD results. Whereas the distribution of the absolute relative differences in transverse displacements in CCM and Pd results are shown in Fig. 2.10. The maximum differences in CCM and PD

results are obtained from the non-corrected case, as shown in Figs. 2.9a and 2.10a. Due to missing neighbors, PD material points at the corners and edges suffer from the skin effect and exhibit larger deformation as expected. It is obtained that Silling’s, Madenci’s, and the proposed discrete surface correction methods significantly decrease the skin effect, as shown in Figs. 2.9b and 2.10b; 2.9c and 2.10c; and 2.9d and 2.10d, respectively.

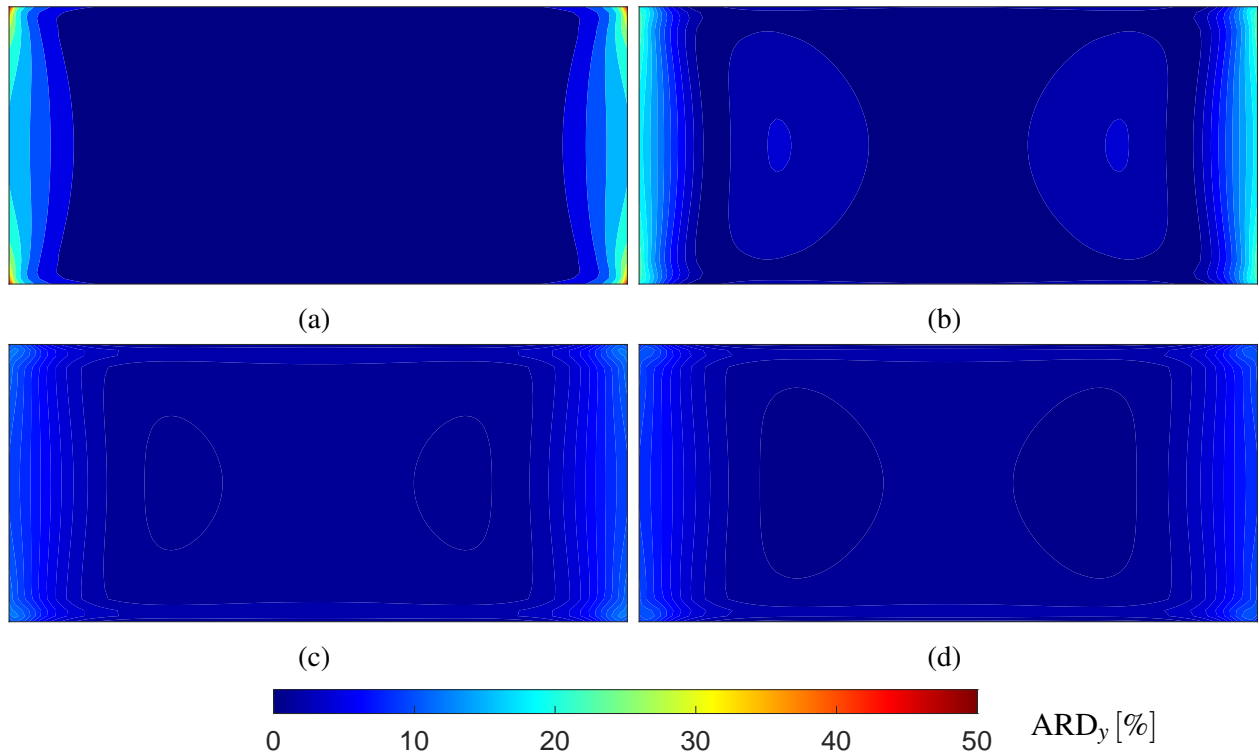


Figure 2.10: Contour plots for absolute relative difference [%] of y -displacements in CCM and PD results with (a) no correction, (b) Silling’s, (c) Madenci’s, and (d) discrete surface correction methods, 100×50 , $\delta = 5h$

As the horizon size increases, the number of neighbors in the neighborhood of the PD nodes increase. Therefore, it is expected that the number of material points suffering from the skin effect also increases for larger horizons. This can be seen easily from Fig. (2.11). Solid black lines represent the maximum differences in CCM and PD results without any correction method. For a constant uniform grid spacing, h , maximum differences in both x and y -displacements increase as the horizon size increases. The difference in CCM and PD results can reach a value of 50% as in the case of the difference in transverse displacements when the horizon is five times the uniform grid spacing. This indicates that PD results without surface corrections deviate from CCM results

as the horizon increases.

Maximum absolute relative differences in the CCM and PD results with Silling's, Madenci's, and the proposed surface correction techniques with increasing horizons can also be seen in Fig. (2.11) with blue, green, and red lines, respectively. Contrary to the non-corrected case, the differences in the results of CCM and PD with a surface correction decrease as the horizon size increases. It is important to note that we use a 1-point Gauss quadrature rule in the spatial discretization of the PD equation of motion in the meshless technique. Therefore, each neighbor represents a collocation point that is used in spatial discretization. Therefore, it is not preferred to use $\delta = 3h$ in 2D simulations. Instead, it is suggested to use 4 or 5 times grid spacing to increase the number of collocation points used in the discretization, which will eventually increase the accuracy of the discretization. However, an increase in the horizon can dramatically increase the computational time. Therefore, an optimum size of the horizon should be selected by considering the accuracy and computational cost.

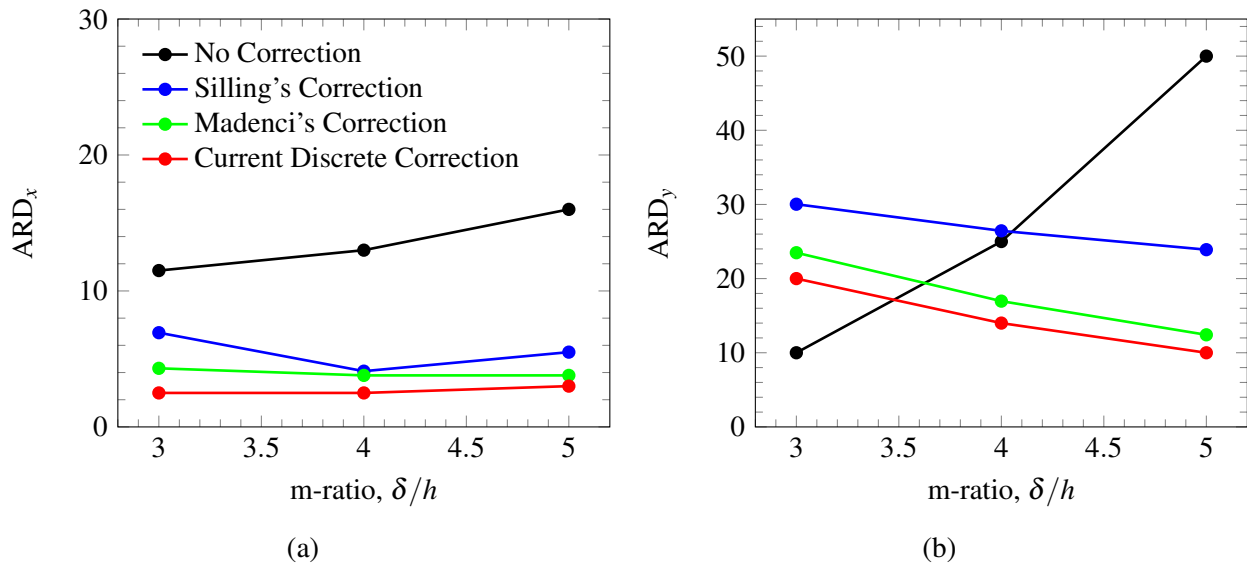


Figure 2.11: Change of maximum absolute relative differences in (a) x, and (b) y-displacements with different m-ratios

As shown in Fig. (2.11), the lowest maximum differences in CCM and PD results are achieved when the proposed surface correction technique is utilized in the simulations. The maximum difference in the entire problem domain is obtained as 3% and 10% in horizontal and transverse displacement fields obtained from PD with discrete surface correction method, respectively.

2.3.2 Plate with a center hole

A 0.06×0.06 m plate having a center hole whose radius is 5 mm is subjected to uniaxial tensile stress of 10 MPa, as shown in Fig. 2.12. Young's modulus of the plate, E , is 1 GPa, and Poisson's ratio, ν , is used as $1/3$.

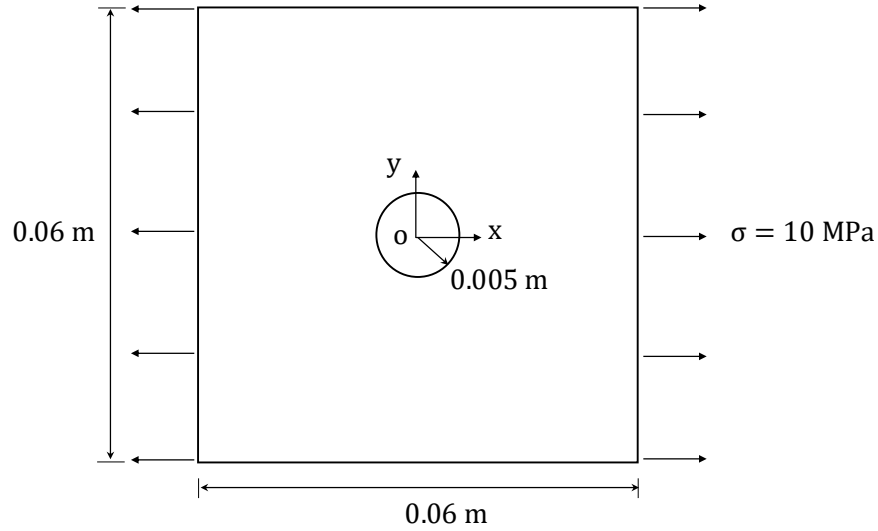


Figure 2.12: Problem setup: A square plate with a center hole is subjected to uniaxial tensile stress

This problem was first modeled in a commercial FEA software, ABAQUS, with 9872 quadrilateral elements. Then, ABAQUS mesh is used for seeding the peridynamic nodes at the geometrical centers of the quadrilateral elements. The approximate grid spacing in the horizontal and vertical direction is 0.6×10^{-3} m in peridynamic simulation.

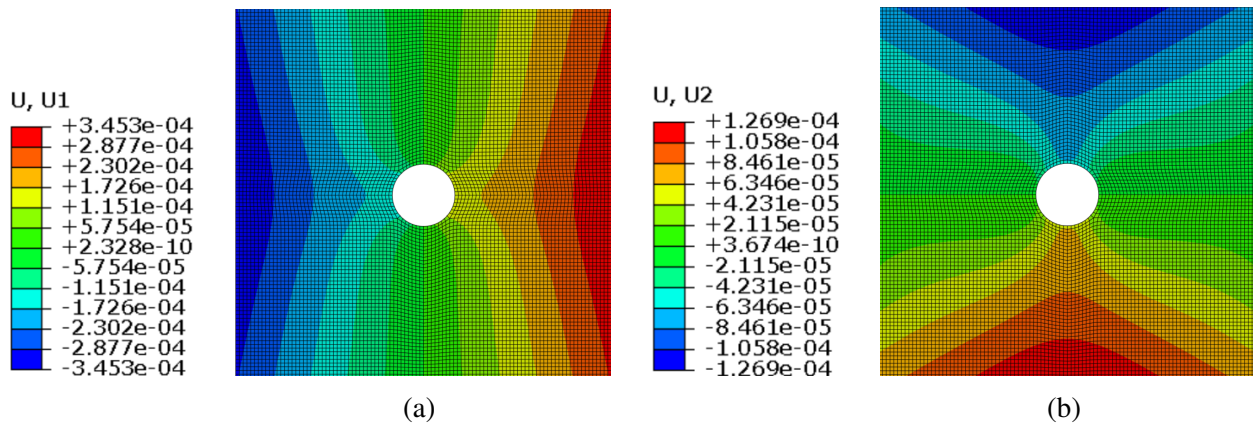


Figure 2.13: Results of FEA: (a) horizontal, and (b) vertical displacement fields

The solutions of the horizontal and vertical displacements from FEA are given in Figs.

2.13a and 2.13b, respectively. The corresponding peridynamic results without surface correction are shown in Figs. 2.14a and 2.15a. Similar to the previous problem, peridynamic analysis gives higher displacements at the corners and along the plate boundaries. Due to skin effects, boundary nodes become weaker than the nodes located far from boundaries, resulting in higher displacements at these locations.

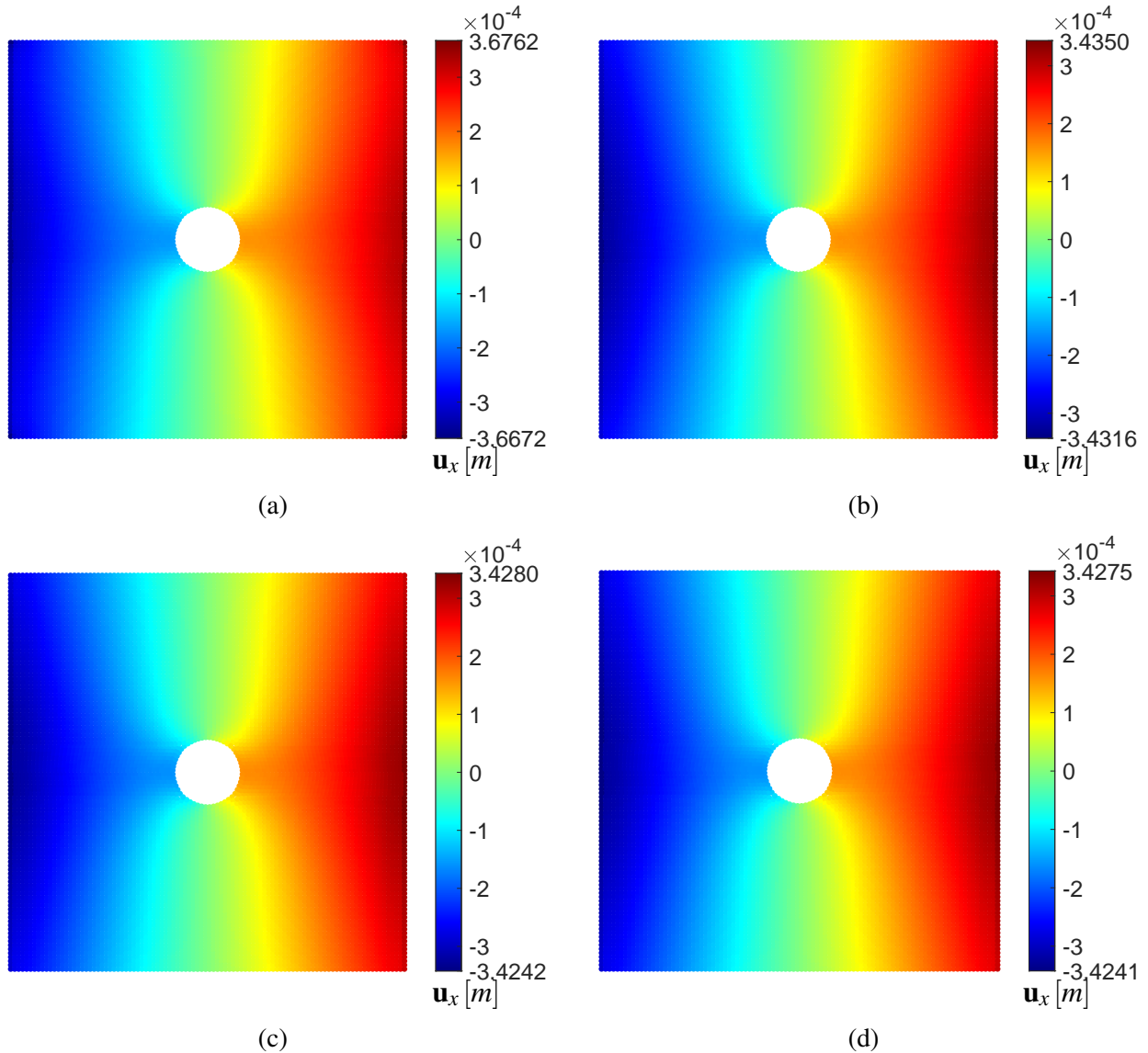


Figure 2.14: PD results for x-displacement [m] with (a) no correction, (b) Silling's, (c) Madenci's, and (d) Current discrete surface correction methods, $\delta = 5h$

Horizontal displacement fields obtained from PD analyses with Silling's, Madenci's, and the proposed discrete surface correction methods are given in Figs. 2.14b, 2.14c, and 2.14d, re-

spectively. Compared to the non-corrected PD result given in Fig. 2.14a, higher displacement values obtained from surface nodes decreased effectively. The same conclusion is obtained for the vertical displacements fields shown in Fig. 2.15.

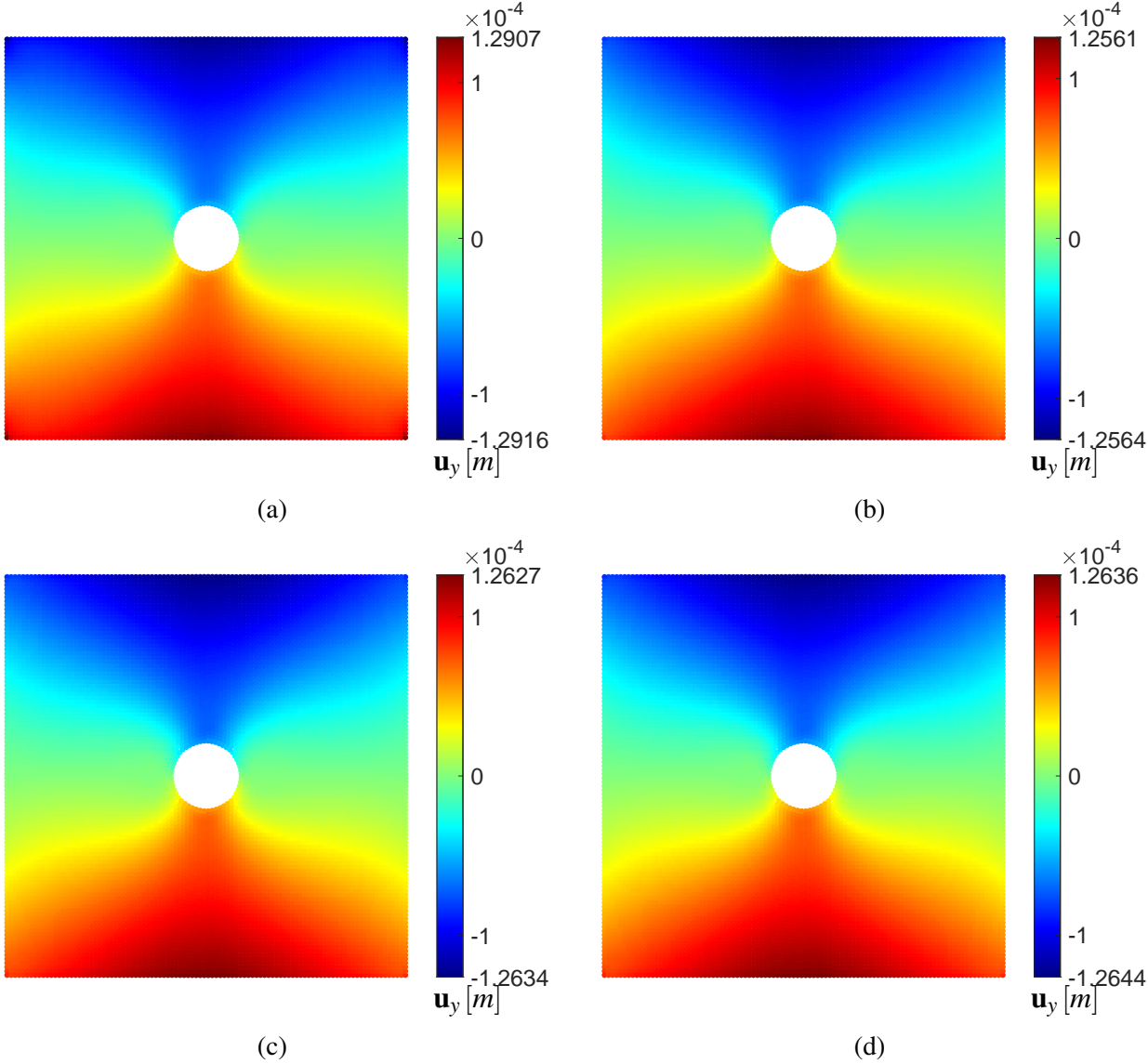


Figure 2.15: PD results for y-displacement [m] with (a) no correction, (b) Silling's, (c) Madenci's, and (d) Current discrete surface correction methods, $\delta = 5h$

In Fig. 2.16, the horizon displacement field is plotted along the line $y = 0$ and $0.05 < x < 0.03$ m, where maximum horizontal displacements are obtained. The PD result without surface correction significantly deviates from the FEA results at the plate's right edge, where tensile stress is applied. The node at the right edge of the plate is weaker due to the skin effect, and when a

load is applied to that node, it deforms more than expected. However, when a surface correction technique is utilized, skin effects are reduced, and PD results show better agreement with the FEA results.

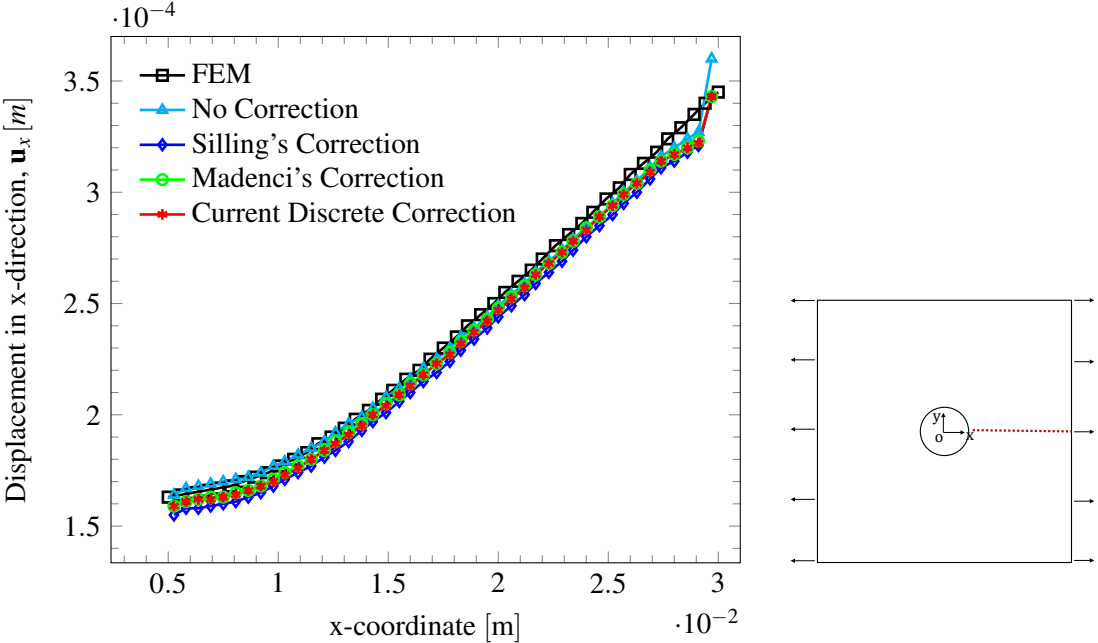


Figure 2.16: Comparison of the horizon displacement field along the line $y = 0$ and $0.05 < x < 0.03$ m, $\delta = 5h$

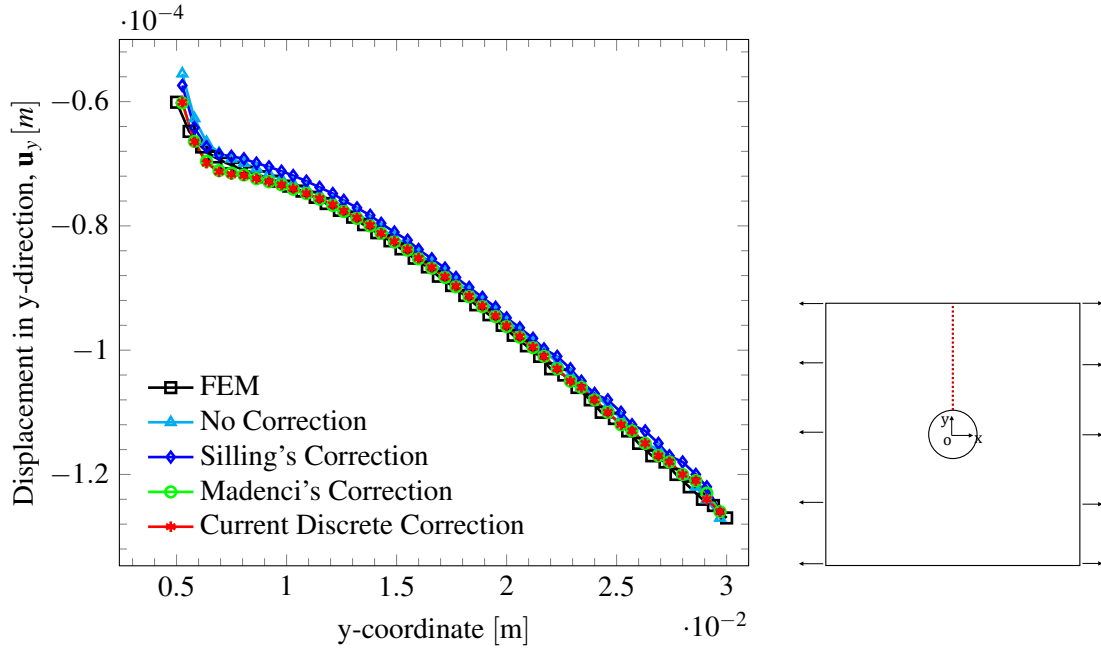


Figure 2.17: Comparison of the vertical displacement field along the line $x = 0$ and $0.05 < y < 0.03$ m, $\delta = 5h$

Vertical displacements are plotted along the line $x = 0$ and $0.05 < y < 0.03$ m as shown in Fig. 2.17. This time, the non-corrected case predicts less displacement around the circular hole. On the other hand, FEM results agree very well with peridynamic results when Silling's, Madenci's, and proposed discrete surface correction methods are utilized.

The FEA and PD results with discrete surface correction methods with different horizon sizes are plotted in Figs. 2.18 and 2.19 for the same grid. It is obtained that while the horizontal displacement does show a considerable difference, the transverse displacement field approaches the FEA results as the horizon increases. Hence, it is concluded that the discrete surface correction technique is also effective in reducing the skin effects and improving the results' accuracy even with the non-uniform grids and boundaries.

2.3.3 Uniaxial dynamic loading

A rectangular pre-notched plate with 0.1 m length and 0.04 m width is subjected to uniaxial tensile stresses as shown in Fig. 2.20. The selected material is Duran 50 glass whose density is $2,235 \text{ kg/m}^3$, Young's modulus is 65 GPa, and fracture energy is 204 J/m^2 . Although Poisson's

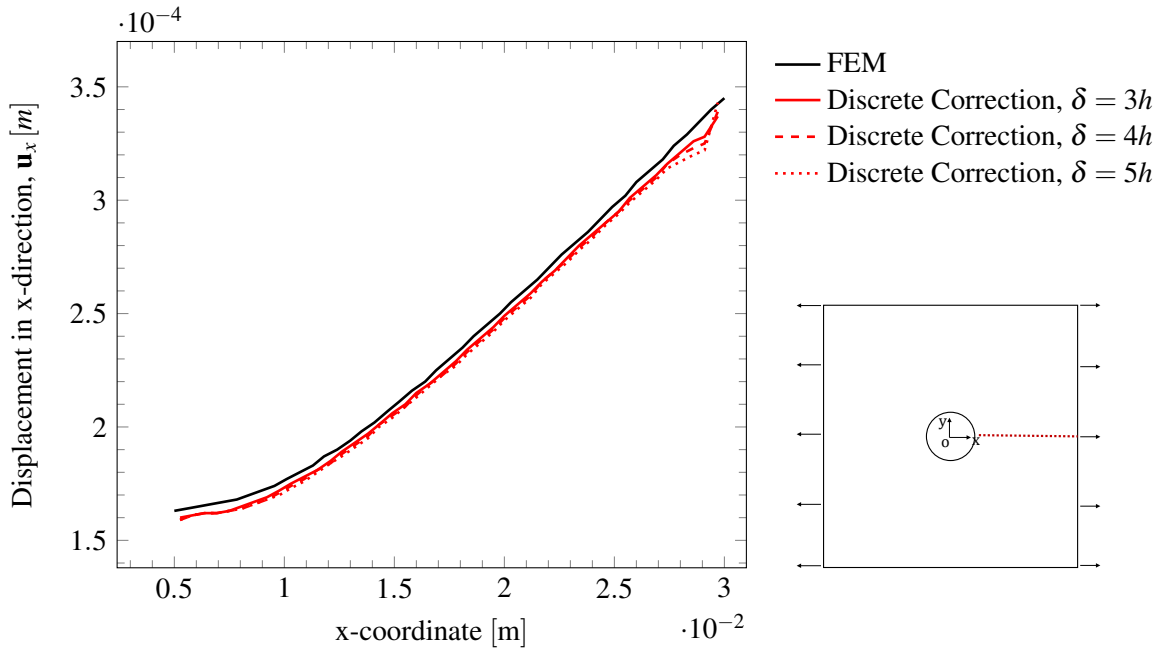


Figure 2.18: Comparison of the horizon displacement field along the line $y = 0$ and $0.05 < x < 0.03$ m, for different horizon sizes

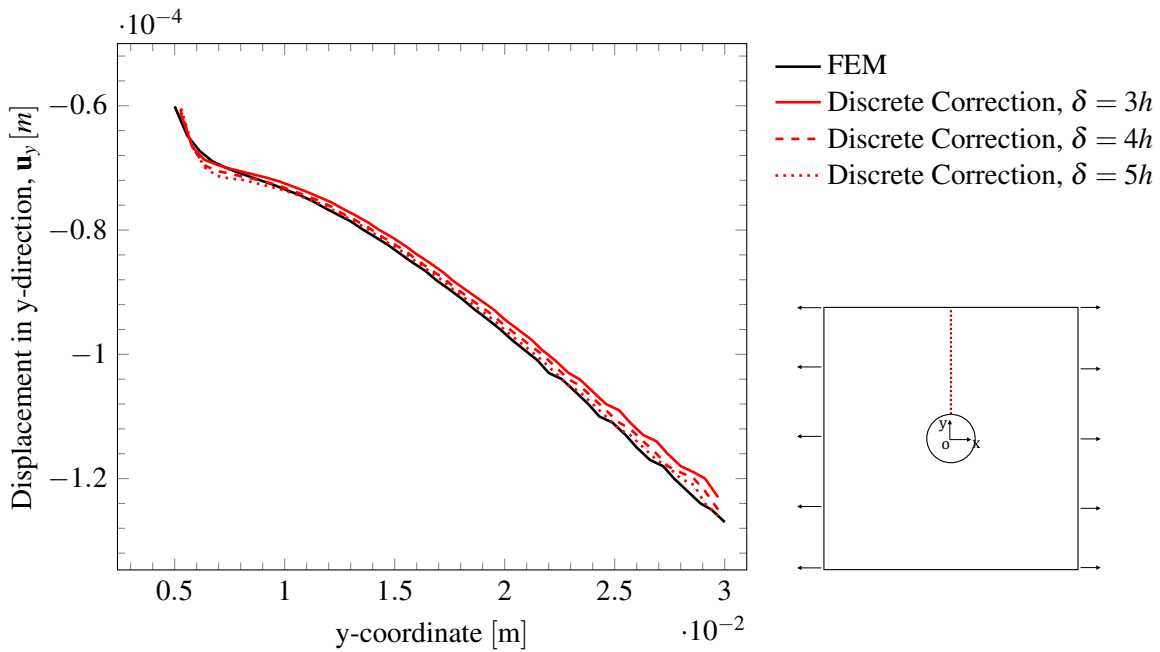


Figure 2.19: Comparison of the vertical displacement field along the line $x = 0$ and $0.05 < y < 0.03$ m, for different horizon sizes

ratio of the material is 0.2, it is used as $1/3$ in the simulations due to Poisson's ratio restriction of the bond-based peridynamic material model.

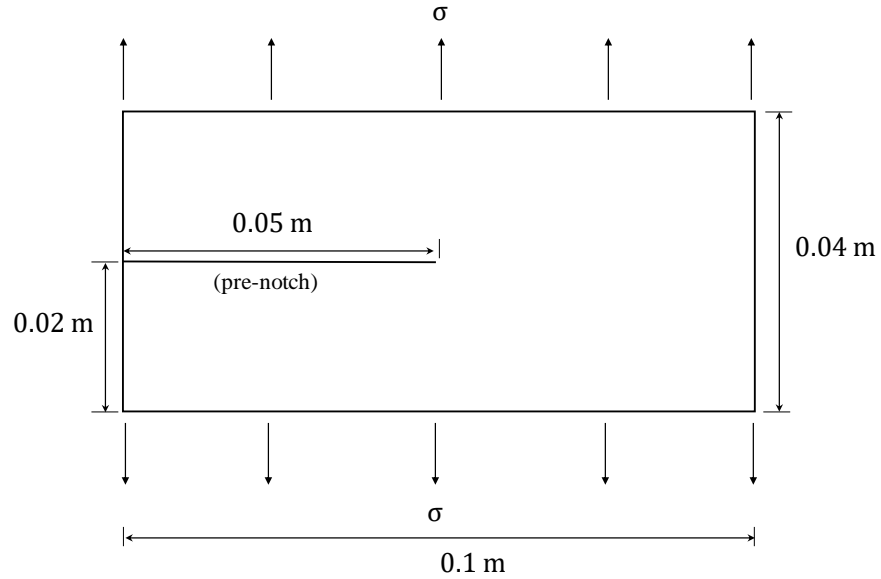


Figure 2.20: Problem setup: a plate under uniaxial dynamic loading

The pre-notched plate's crack propagation and branching results are obtained for the different grid and horizon sizes and two different stress magnitudes, 12 and 30 MPa. Stresses are converted to body forces and directly applied to one layer of material points along the plate's top and bottom edges and kept constant during the simulation. Furthermore, to prevent tearing of the first few layers of material points from the entire plate, no-failure zones are defined with a horizon size width at locations where the stresses are applied. A stable constant time step is fixed to 30 nanoseconds, and the total duration of the simulation is 60 microseconds. The selected time step is smaller than the 70% of the critical time step calculated using Algorithm 2. PD nodes are seeded on uniform grids.

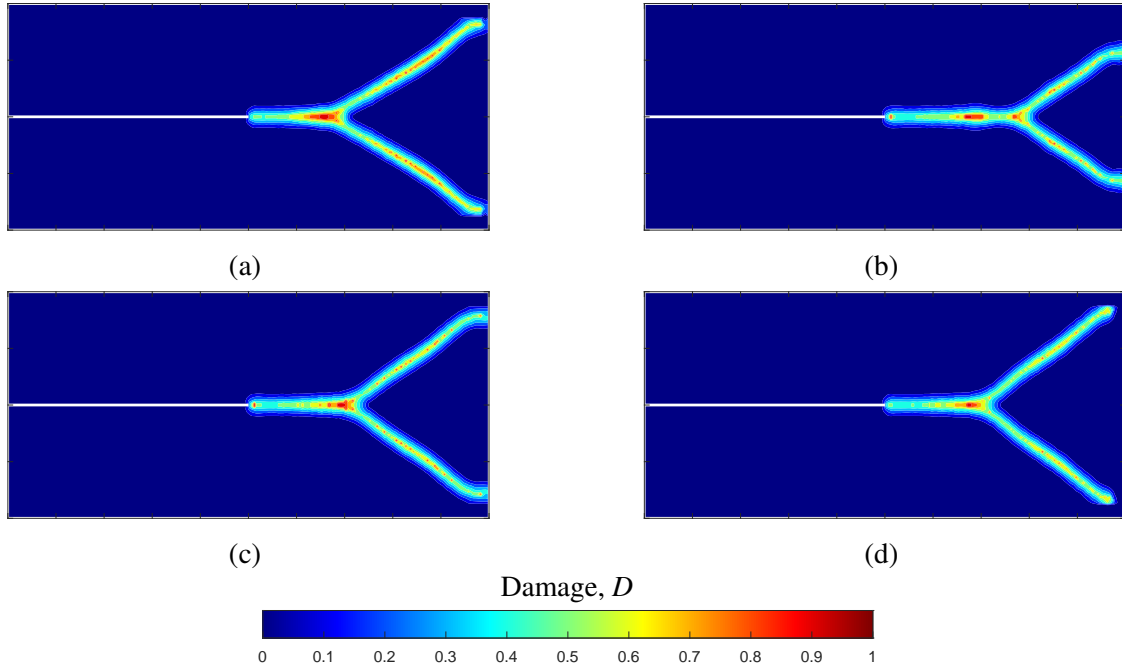


Figure 2.21: Comparison of crack paths under uniaxial dynamic loading of 12 MPa with (a) no correction, (b) Silling's, (c) Madenci's, and (d) Current discrete surface corrections, 200×80 , $\delta = 5h$

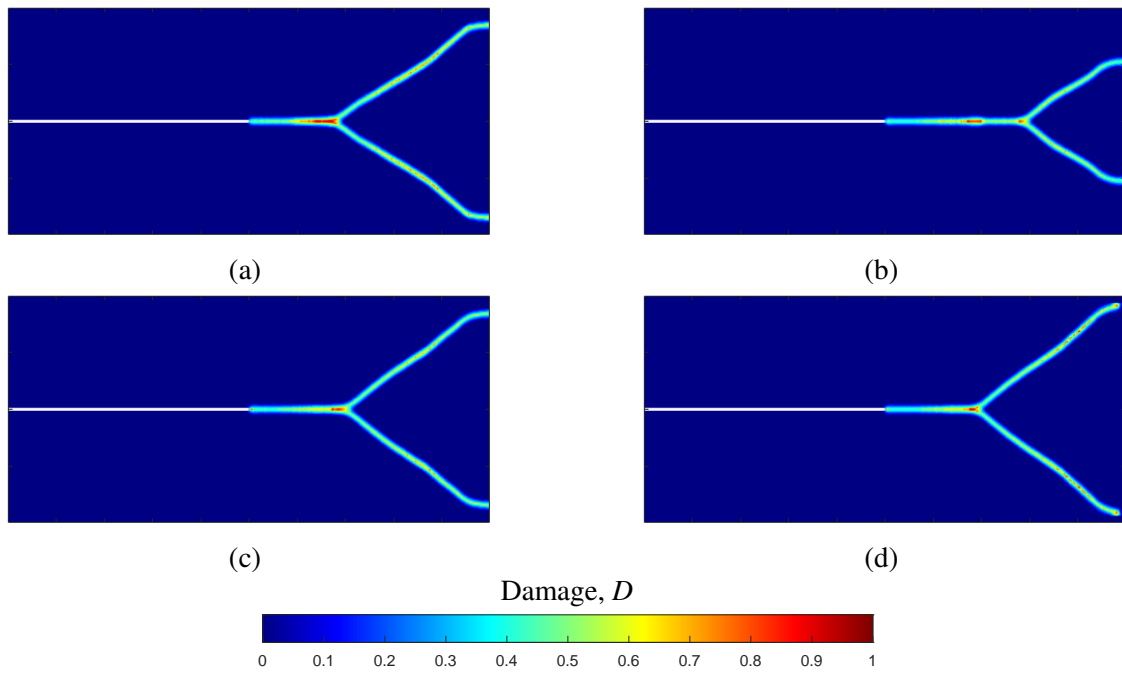


Figure 2.22: Comparison of crack paths under uniaxial dynamic loading of 12 MPa with (a) no correction, (b) Silling's, (c) Madenci's, and (d) Current discrete surface corrections, 400×160 , $\delta = 5h$

For a uniform grid spacing of 0.5×10^{-3} m with a horizon of 2.5×10^{-3} m, a comparison of the crack paths from PD simulations under 12 MPa uniaxial dynamic loading is given in Fig.

2.21. For the same loading conditions, PD results with a finer mesh are provided in Fig. 2.22. In these simulations, the main crack starts to propagate from the tip of the pre-notch. It branches into two cracks after straight crack propagation. It is obtained that PD results with no-correction, Madenci's, and discrete surface corrections give similar crack growth and branching. On the other hand, Silling's surface correction results in more extended straight propagation of the main crack compared to others.

Figs. 2.23 and 2.24 show the comparison of the crack paths when the applied stress is 30 MPa for different uniform grid spacing. Although the selected time step is much smaller than the critical one calculated using Eq. (2.8), the crack path results from PD simulations with uniform grids of 0.5×10^{-3} m and 0.25×10^{-3} m show considerable differences due to high crack tip instabilities that occur in the crack branching phenomenon under the high-stress levels. When the applied stresses are increased from 12 to 30 MPa, the straight propagation of the main crack decreases significantly. Moreover, secondary branches are observed in the PD simulations with higher stress levels.

For a uniform grid spacing of 0.5×10^{-3} m, crack paths obtained from PD results with the proposed discrete surface correction results are plotted in Fig. 2.25 for three different horizon sizes. As shown in Fig. 2.25, crack paths are not significantly affected by the increase in the horizon. However, this is not the case for the values of the different uniform grid and horizon sizes. Fig. 2.26 shows the crack paths when uniform grid spacing is 0.25×10^{-3} m, and applied stresses are still 12 MPa. It is obtained that crack branching happens after a longer straight crack growth in PD results with discrete surface correction when the uniform grid spacing is 0.25×10^{-3} m, and the horizon is 1.0×10^{-3} m, as shown in Fig. 2.26b.

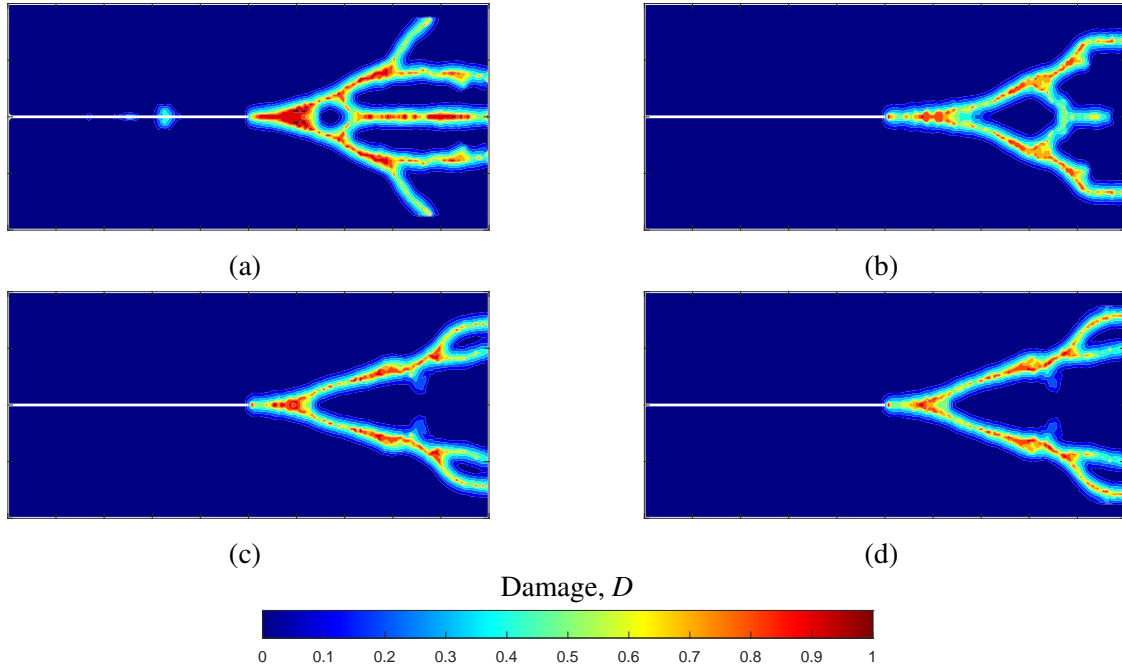


Figure 2.23: Comparison of crack paths under uniaxial dynamic loading of 30 MPa with (a) no correction, (b) Silling's, (c) Madenci's, and (d) Current discrete surface corrections, 200×80 , $\delta = 5h$

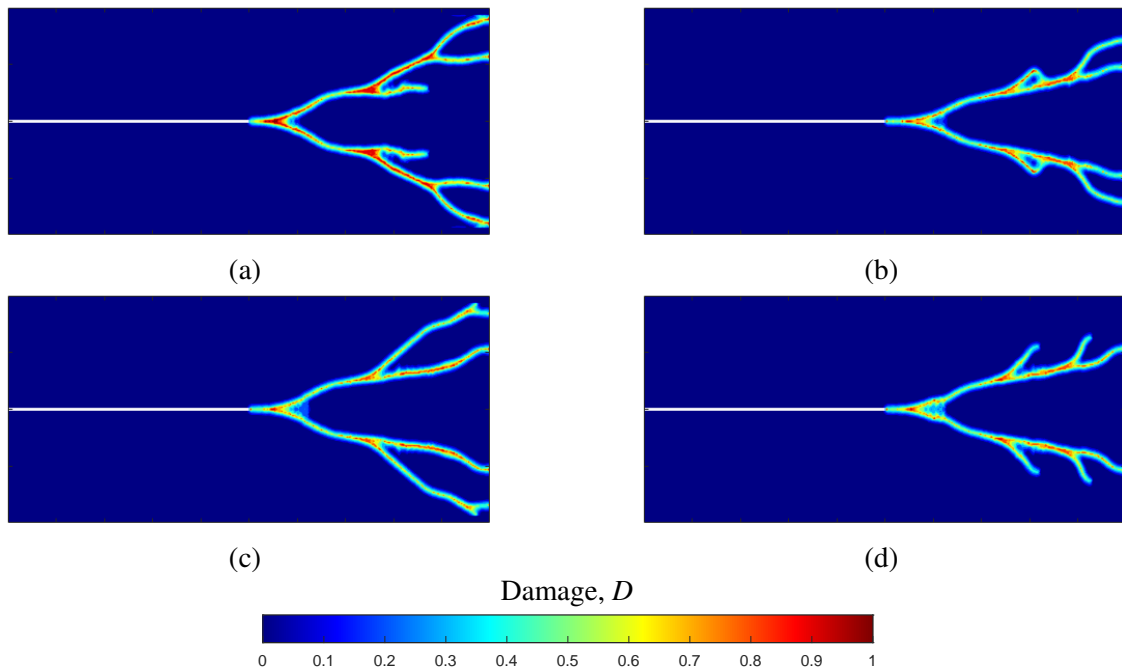


Figure 2.24: Comparison of crack paths under uniaxial dynamic loading of 30 MPa with (a) no correction, (b) Silling's, (c) Madenci's, and (d) Current discrete surface corrections, 400×160 , $\delta = 5h$

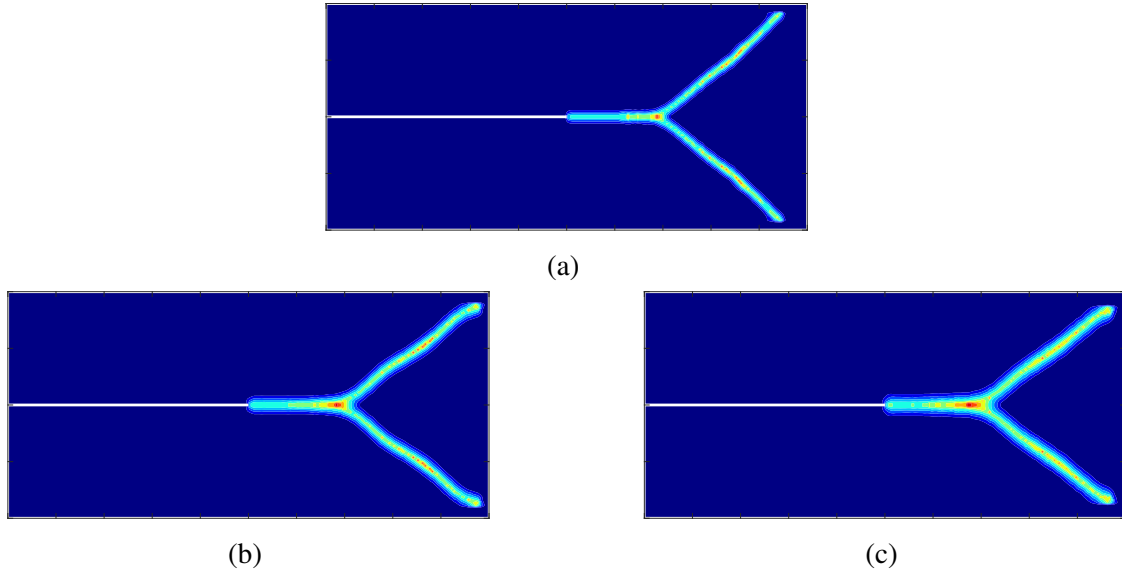


Figure 2.25: Crack paths results under uniaxial dynamic loading of 12 MPa for PD simulation with discrete surface correction and $\delta =$ (a) $3h$, (b) $4h$, and (c) $5h$ in a 200×80 grid

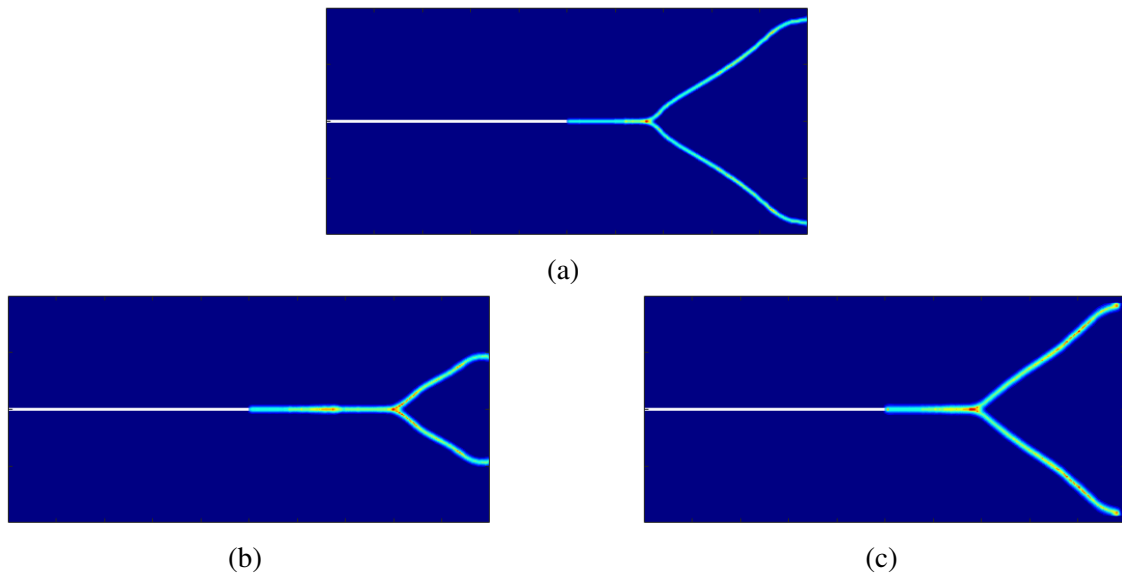


Figure 2.26: Crack paths results under uniaxial dynamic loading of 12 MPa for PD simulation with discrete surface correction and $\delta =$ (a) $3h$, (b) $4h$, and (c) $5h$ in a 400×160 grid

Figs. 2.27 and 2.28 show the crack paths obtained from the PD results with discrete surface correction method when the uniaxial dynamic loading is 30 MPa. For high-stress values such as 30 MPa, grid spacing greatly influences the crack branching results. In addition, coarser grid results, given in Fig. 2.27, and finer grid results, provided in Fig. 2.28, show that the crack paths are also affected by the horizon size.

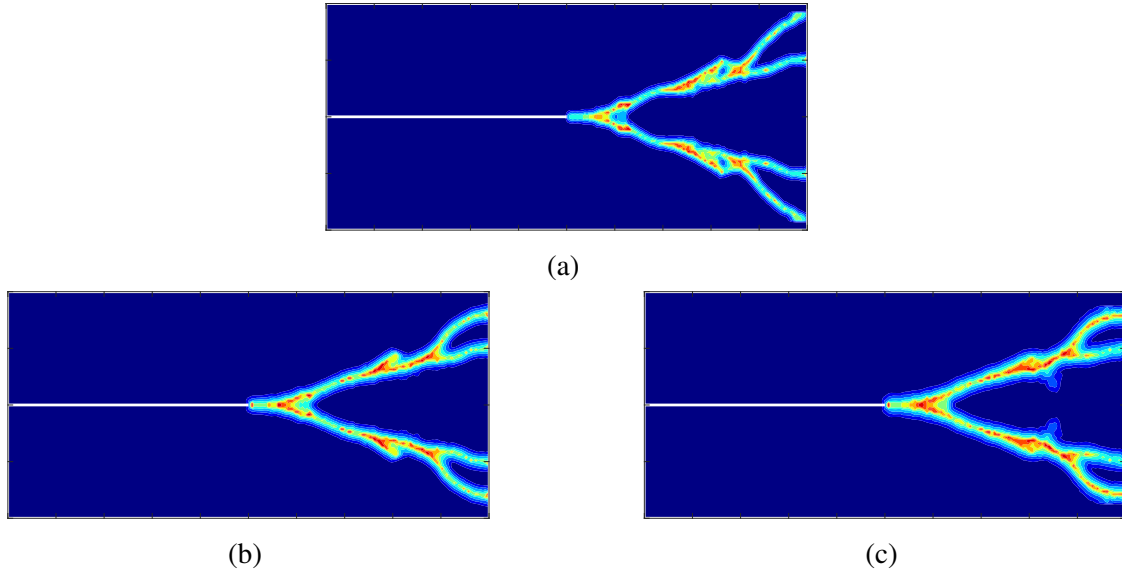


Figure 2.27: Crack paths results under uniaxial dynamic loading of 30 MPa for PD simulation with discrete surface correction and $\delta =$ (a) $3h$, (b) $4h$, and (c) $5h$ in a 200×80 grid

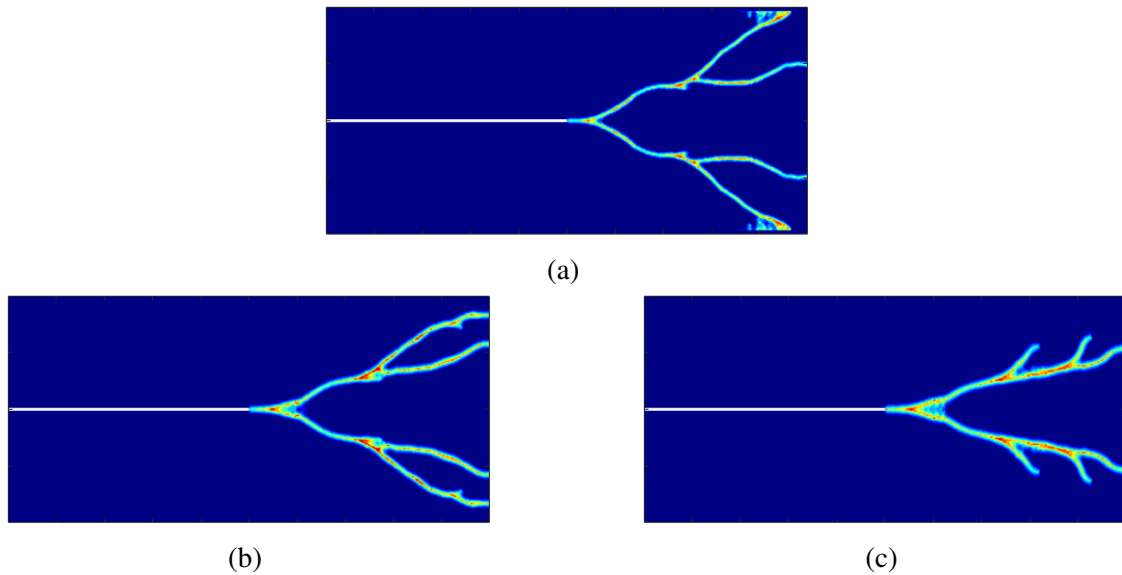


Figure 2.28: Crack paths results under uniaxial dynamic loading of 30 MPa for PD simulation with discrete surface correction and $\delta =$ (a) $3h$, (b) $4h$, and (c) $5h$ in a 400×160 grid

2.3.4 Kalthoff-Winkler's experiment

Kalthoff [110, 111] shows that the fracture type changes with the impact speed. While a brittle failure is observed at lower impact speed, failure mode changes to ductile failure at high impact speed [111]. This study focuses on the brittle failure.

Fig. 2.29 shows the geometry and the boundary conditions that are used in the numerical model. It is assumed that the contact velocity is 16.5 m/s and applied to one layer of nodes where impact happens and kept constant during the simulations.

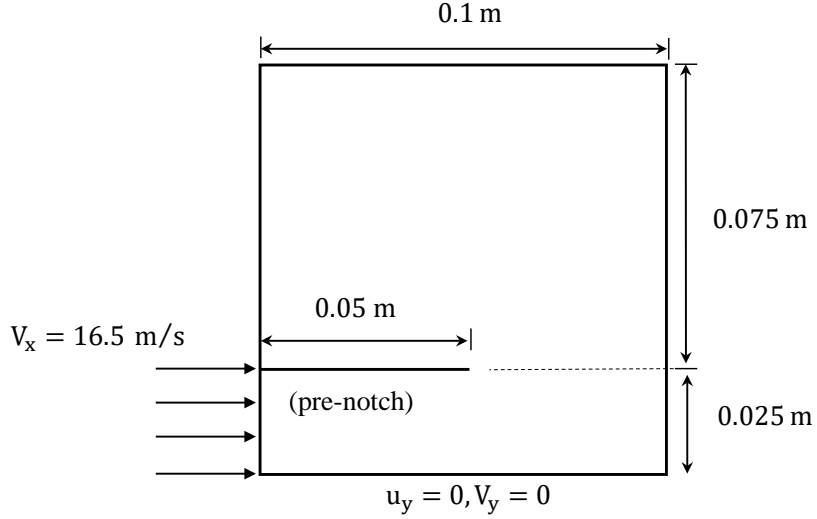


Figure 2.29: Numerical model to simulate Kalthoff-Winkler's experiment

The material's mechanical properties are Young's modulus is 190 GPa, mass density is 8,000 kg/m³ and fracture energy is 22,170 J/m². The Poisson's ratio is fixed to 1/3. The uniform grid spacing is used in this study. A stable constant time step is selected as 30 nanoseconds, and the total duration of the simulation is 90 microseconds. Similar to the previous example, the selected time step is smaller than the 70% of the critical time step calculated using Algorithm 2. To compare the maximum critical time step obtained by Courant–Friedrichs–Lewy (CFL) formula

$$\Delta t_{cr} = \frac{h}{c} \quad (2.39)$$

where h is the characteristic length depending on the discretization and c is the wave speed that can be calculated by

$$c = \sqrt{\frac{E}{\rho}} \quad (2.40)$$

which results in approximately 4875 m/s. Then, CFL formula yields 1.03×10^{-7} and 5.1×10^{-8} seconds for coarse and fine meshes respectively. Hence, the selected time step is smaller than the

resultant critical time steps that are needed for a wave to travel to the adjacent node.

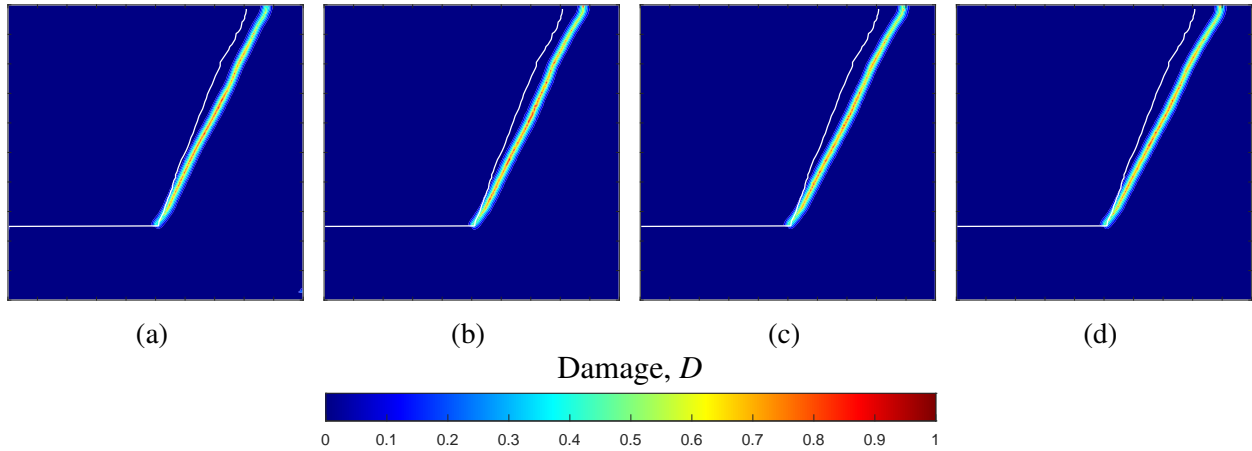


Figure 2.30: Comparison of crack paths with the experimental result (solid white line) and peridynamic simulation with (a) no correction, (b) Silling's, (c) Madenci's, and (d) Current discrete surface correction methods, 200×200 , $\delta = 5h$

The obtained crack paths from PD simulations are compared with the experimental one digitized from [112]. Fig. 2.30 shows the comparison of the crack paths with the experimental results when the uniform grid spacing is 0.5×10^{-3} , and the horizon is 2.5×10^{-3} m. PD simulations result in a single crack propagating from the pre-notch tip with an angle of 63° approximately.

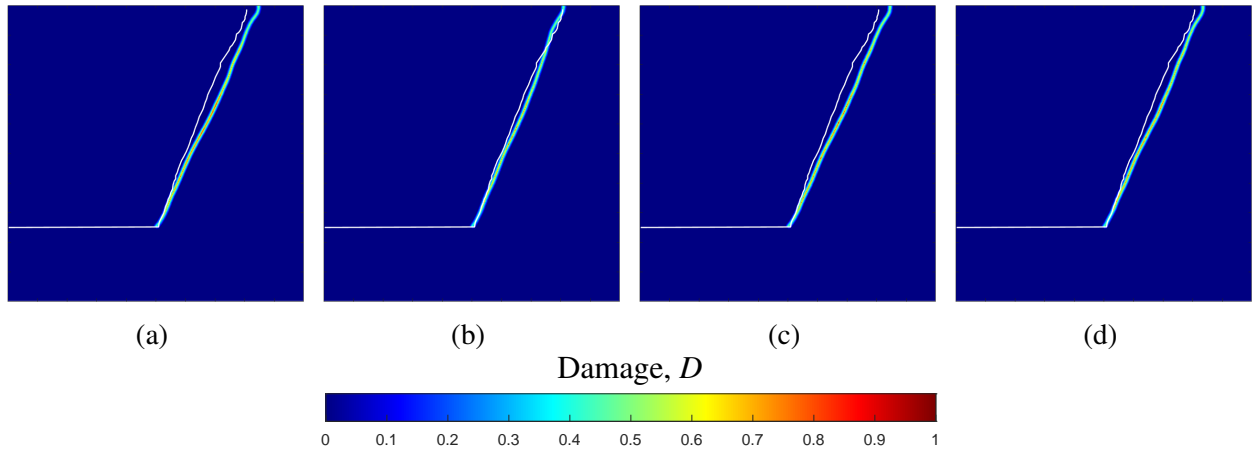


Figure 2.31: Comparison of crack paths with the experimental result (solid white line) and peridynamic simulation with (a) no correction, (b) Silling's, (c) Madenci's, and (d) Current discrete surface correction methods, 400×400 , $\delta = 5h$

Fig. 2.31 shows the comparison of the crack paths with the experimental results when the uniform grid spacing is 0.25×10^{-3} , and the horizon is 1.25×10^{-3} m. PD simulations result

in a single crack propagating from the pre-notch tip with an angle around 68° , which shows an excellent match with the experimental result.

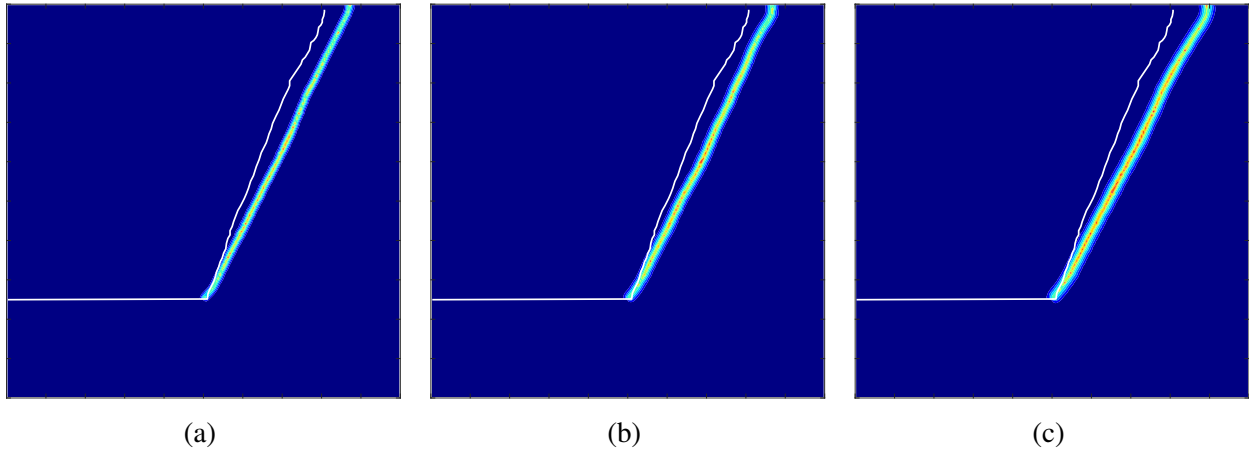


Figure 2.32: Comparison of crack paths with the experimental result (solid white line) and PD simulation with discrete surface correction and $\delta =$ (a) $3h$, (b) $4h$, and (c) $5h$ in a 200×200 grid

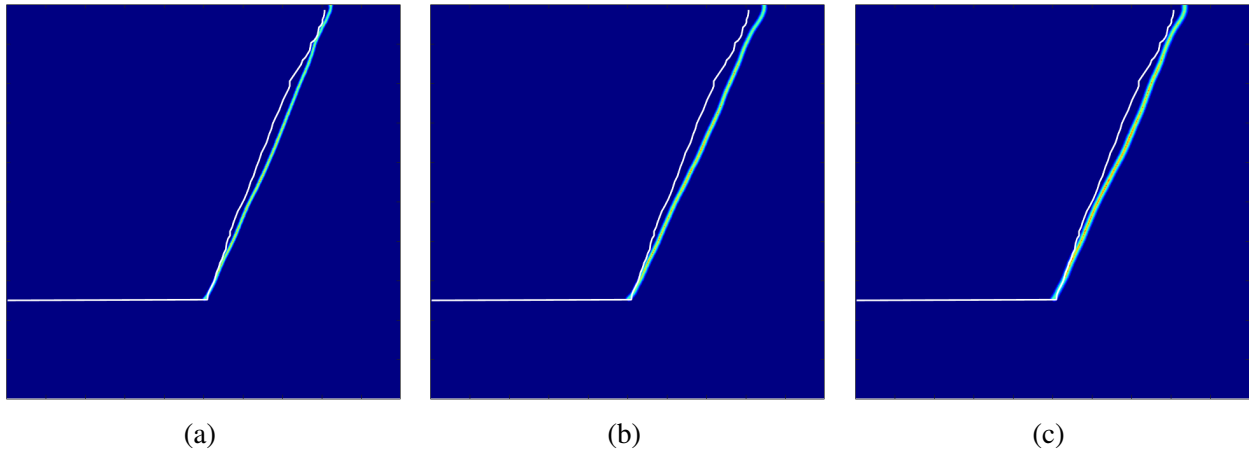


Figure 2.33: Comparison of crack paths with the experimental result (solid white line) and PD simulation with discrete surface correction and $\delta =$ (a) $3h$, (b) $4h$, and (c) $5h$ in a 400×400 grid

Figs. 2.32 and 2.33 compare the crack paths with the experimental and PD results with the discrete surface correction methods. The larger grid spacing shown in Fig. 2.32 shows that the crack angle is smaller than the one obtained from the experiment. However, solutions are improved by decreasing the grid spacing, as shown in Fig. 2.33. This time, all three simulations with different horizon sizes result in perfect agreement with the experimental results. Also, the solutions for the smaller grid size are not affected by the horizon size significantly.

2.4 Chapter Summary

In this chapter, the convergence and accuracy of the linear elastic bond-based PD model enhanced with the proposed surface correction are investigated. The proposed technique is named as the *discrete surface correction method*, where both PD material parameters, c and s_0 , are calculated in discrete form through the simulation. As a summary,

- In the static problems, it is obtained that the PD solutions enriched with the discrete surface correction method approach to CCM results when the horizon is increased from 3 to 5 times of the grid spacing.
- In crack propagation simulations, newly emerging boundaries can be successfully treated with the help of the discrete surface correction method.
- As in the continuum damage models, the micromodulus, or bond constant, is needed to be degraded if there is any damage at the material points connected by a bond.
- For the problems which include high crack tip instabilities with several crack branching, the effect of the horizon, which controls the degree of nonlocality, is predominant in the result of the simulations. Therefore, smaller grid spacing and a horizon size equivalent to five times grid spacing can be suggested for these problems.
- Both static and dynamic examples show that the proposed discrete surface correction provides better accuracy compared with other methods presented in the literature.

CHAPTER 3

NOSB-PD WITH ELECTROMECHANICAL COUPLING

3.1 A Brief Description of Non-Ordinary State-Based Peridynamics

In state-based peridynamics, the equation of motion is written as [8]

$$\rho \ddot{\mathbf{u}} = \int_{\mathcal{H}} \{ \underline{\mathbf{T}} \langle \mathbf{x}' - \mathbf{x} \rangle - \underline{\mathbf{T}}' \langle \mathbf{x} - \mathbf{x}' \rangle \} dV + \mathbf{b} \quad (3.1)$$

$\underline{\mathbf{T}} \langle \mathbf{x}' - \mathbf{x} \rangle$ is the force vector-state that particle \mathbf{x}' exerts on particle \mathbf{x} . A general state-based peridynamic constitutive model can be expressed as

$$\underline{\mathbf{T}} \langle \xi \rangle = \underline{\mathbf{T}}(\underline{\mathbf{Y}}) \langle \xi \rangle = \nabla W(\underline{\mathbf{Y}}), \quad (3.2)$$

where W is the strain energy density function and ∇W is its Frechet derivative, and $\underline{\mathbf{Y}}$ is the deformation vector-state defined by

$$\underline{\mathbf{Y}} \langle \xi \rangle = \mathbf{y}(\mathbf{x}') - \mathbf{y}(\mathbf{x}) = (\mathbf{x}' + \mathbf{u}(\mathbf{x}')) - (\mathbf{x} + \mathbf{u}(\mathbf{x})). \quad (3.3)$$

Suppose there is a strain energy density function in the classical theory U such that

$$\underline{\mathbf{Y}} \langle \xi \rangle = \mathbf{F} \xi \quad \text{and} \quad W(\underline{\mathbf{Y}}) = U(\mathbf{F}), \quad (3.4)$$

then, the PD constitutive model is called *correspondence* to the classical constitutive model at \mathbf{F} (the deformation gradient tensor). A corresponding deformation gradient, $\bar{\mathbf{F}}$ is found as

$$\bar{\mathbf{F}} = \left(\int_{\mathcal{H}} \omega(\underline{\mathbf{Y}} \otimes \xi) dV \right) \mathbf{K}^{-1} \quad (3.5)$$

where shape tensor \mathbf{K} is given as

$$\mathbf{K} = \underline{\mathbf{X}} * \underline{\mathbf{X}} = \int_{\mathcal{H}} \underline{\omega} \underline{\mathbf{X}} \otimes \underline{\mathbf{X}} dV = \int_{\mathcal{H}} \underline{\omega} \underline{\xi} \otimes \underline{\xi} dV. \quad (3.6)$$

Suppose a peridynamic correspondence material model is defined by

$$W(\underline{\mathbf{Y}}) = U(\bar{\mathbf{F}}(\underline{\mathbf{Y}})), \quad (3.7)$$

so that

$$\nabla W(\underline{\mathbf{Y}}) = \nabla U(\bar{\mathbf{F}}(\underline{\mathbf{Y}})) = \frac{\partial U}{\partial \bar{F}_{ij}} \nabla \bar{\mathbf{F}}(\underline{\mathbf{Y}}) = P_{ij} \bar{\mathbf{F}}(\underline{\mathbf{Y}}), \quad (3.8)$$

where P_{ij} is the component of the first Piola-Kirchhoff (PKI) stress \mathbf{P} , obtained from the approximate deformation gradient given in Eq. (3.5) based on the classical constitutive model. Silling [8] derived the force density vector-state as the following form:

$$\underline{\mathbf{T}}\langle \underline{\xi} \rangle = \underline{\mathcal{E}}(\mathbf{PK}^{-1}) = \underline{\omega} \mathbf{PK}^{-1} \underline{\xi} \quad (3.9)$$

3.1.1 Discrete equations of non-ordinary state-based peridynamics

The shape tensor evaluated at material point \mathbf{x}_j can be discretized as

$$\mathbf{K}(\mathbf{x}_j) = \sum_{n=1}^m \omega(|\mathbf{x}_n - \mathbf{x}_j|) (\mathbf{x}_n - \mathbf{x}_j) \otimes (\mathbf{x}_n - \mathbf{x}_j) V_n \quad (3.10)$$

where m is the number of material points in the neighborhood of \mathbf{x}_j , $\mathcal{H}_{\mathbf{x}_j}$. V_n is the volume associated with the material point n . Similarly, the discretized deformation gradient can be written as:

$$\mathbf{F}(\mathbf{x}_j) = \left[\sum_{n=1}^m \omega(|\mathbf{x}_n - \mathbf{x}_j|) \underline{\mathbf{Y}}\langle \mathbf{x}_n - \mathbf{x}_j \rangle \otimes (\mathbf{x}_n - \mathbf{x}_j) V_n \right] \mathbf{K}^{-1} \quad (3.11)$$

where the deformation vector-state is

$$\underline{\mathbf{Y}}\langle \mathbf{x}_n - \mathbf{x}_j \rangle = (\mathbf{u}_n - \mathbf{u}_j) + (\mathbf{x}_n - \mathbf{x}_j). \quad (3.12)$$

Inserting Eq. (3.12) into Eq. (3.11)

$$\begin{aligned}
\mathbf{F}(\mathbf{x}_j) &= \left[\sum_{n=1}^m \omega(|\mathbf{x}_n - \mathbf{x}_j|) [(\mathbf{u}_n - \mathbf{u}_j) + (\mathbf{x}_n - \mathbf{x}_j)] \otimes (\mathbf{x}_n - \mathbf{x}_j) V_n \right] \mathbf{K}^{-1} \\
&= \left[\sum_{n=1}^m \omega(|\mathbf{x}_n - \mathbf{x}_j|) (\mathbf{u}_n - \mathbf{u}_j) \otimes (\mathbf{x}_n - \mathbf{x}_j) V_n \right] \mathbf{K}^{-1} \\
&\quad + \left[\sum_{n=1}^m \omega(|\mathbf{x}_n - \mathbf{x}_j|) (\mathbf{x}_n - \mathbf{x}_j) \otimes (\mathbf{x}_n - \mathbf{x}_j) V_n \right] \mathbf{K}^{-1} \\
&= \left[\sum_{n=1}^m \omega(|\mathbf{x}_n - \mathbf{x}_j|) (\mathbf{u}_n - \mathbf{u}_j) \otimes (\mathbf{x}_n - \mathbf{x}_j) V_n \right] \mathbf{K}^{-1} + \mathbf{I}
\end{aligned} \tag{3.13}$$

where \mathbf{I} is the identity tensor.

In the classical continuum model, the displacement gradient is defined as

$$\nabla \mathbf{u} = \mathbf{F} - \mathbf{I}. \tag{3.14}$$

Hence, the nonlocal displacement gradient can be obtained as

$$\nabla \mathbf{u} = \mathbf{F}(\mathbf{x}_j) - \mathbf{I} = \left[\sum_{n=1}^m \omega(|\mathbf{x}_n - \mathbf{x}_j|) (\mathbf{u}_n - \mathbf{u}_j) \otimes (\mathbf{x}_n - \mathbf{x}_j) V_n \right] \mathbf{K}^{-1} \tag{3.15}$$

The small strain tensor then becomes

$$\boldsymbol{\varepsilon} = \frac{1}{2}(\nabla \mathbf{u} + \nabla \mathbf{u}^T) = \frac{1}{2}((\mathbf{F} - \mathbf{I}) + (\mathbf{F} - \mathbf{I})^T) = \frac{1}{2}(\mathbf{F} + \mathbf{F}^T) - \mathbf{I}. \tag{3.16}$$

Let us use $\mathbf{M} = \mathbf{K}^{-1}$

$$\mathbf{M} = \mathbf{K}^{-1} = \left[\sum_{n=1}^m \omega(|\mathbf{x}_n - \mathbf{x}_j|) (\mathbf{x}_n - \mathbf{x}_j) \otimes (\mathbf{x}_n - \mathbf{x}_j) V_n \right]^{-1} \tag{3.17}$$

$$\mathbf{A} = \sum_{n=1}^m \omega(|\mathbf{x}_n - \mathbf{x}_j|) (\mathbf{u}_n - \mathbf{u}_j) \otimes (\mathbf{x}_n - \mathbf{x}_j) V_n \tag{3.18}$$

where, the dyadic product of the relative displacement and position vector can be expanded as follows

$$(\mathbf{u}_n - \mathbf{u}_j) \otimes (\mathbf{x}_n - \mathbf{x}_j) = \begin{bmatrix} (u_{1n} - u_{1j})(x_{1n} - x_{1j}) & (u_{1n} - u_{1j})(x_{2n} - x_{2j}) & (u_{1n} - u_{1j})(x_{3n} - x_{3j}) \\ (u_{2n} - u_{2j})(x_{1n} - x_{1j}) & (u_{2n} - u_{2j})(x_{2n} - x_{2j}) & (u_{2n} - u_{2j})(x_{3n} - x_{3j}) \\ (u_{3n} - u_{3j})(x_{1n} - x_{1j}) & (u_{3n} - u_{3j})(x_{2n} - x_{2j}) & (u_{3n} - u_{3j})(x_{3n} - x_{3j}) \end{bmatrix} \quad (3.19)$$

Hence, Eq. (3.13) becomes

$$\mathbf{F} = \mathbf{A}\mathbf{M} + \mathbf{I} \quad (3.20)$$

Then, the transverse of the deformation gradient tensor can be rewritten as

$$\begin{aligned} \mathbf{F}^T &= (\mathbf{A}\mathbf{M})^T + \mathbf{I}^T \\ &= \mathbf{M}^T \mathbf{A}^T + \mathbf{I} \\ &= \mathbf{M}\mathbf{A}^T + \mathbf{I} \end{aligned} \quad (3.21)$$

where the symmetry property of the shape tensor is used. Then,

$$\mathbf{F}^T = \left[\sum_{n=1}^m \omega(|\mathbf{x}_n - \mathbf{x}_j|) (\mathbf{x}_n - \mathbf{x}_j) \otimes (\mathbf{x}_n - \mathbf{x}_j) V_n \right]^{-1} \left[\sum_{n=1}^m \omega(|\mathbf{x}_n - \mathbf{x}_j|) (\mathbf{x}_n - \mathbf{x}_j) \otimes (\mathbf{u}_n - \mathbf{u}_j) V_n \right] + \mathbf{I} \quad (3.22)$$

or,

$$\mathbf{F}^T = \mathbf{M} \left[\sum_{n=1}^m \omega(|\mathbf{x}_n - \mathbf{x}_j|) (\mathbf{x}_n - \mathbf{x}_j) \otimes (\mathbf{u}_n - \mathbf{u}_j) V_n \right] + \mathbf{I}. \quad (3.23)$$

Let us define

$$\mathbf{B} = \sum_{n=1}^m \omega(|\mathbf{x}_n - \mathbf{x}_j|) (\mathbf{x}_n - \mathbf{x}_j) \otimes (\mathbf{u}_n - \mathbf{u}_j) V_n \quad (3.24)$$

where,

$$(\mathbf{x}_n - \mathbf{x}_j) \otimes (\mathbf{u}_n - \mathbf{u}_j) = \begin{bmatrix} (x_{1n} - x_{1j})(u_{1n} - u_{1j}) & (x_{1n} - x_{1j})(u_{2n} - u_{2j}) & (x_{1n} - x_{1j})(u_{3n} - u_{3j}) \\ (x_{2n} - x_{2j})(u_{1n} - u_{1j}) & (x_{2n} - x_{2j})(u_{2n} - u_{2j}) & (x_{2n} - x_{2j})(u_{3n} - u_{3j}) \\ (x_{3n} - x_{3j})(u_{1n} - u_{1j}) & (x_{3n} - x_{3j})(u_{2n} - u_{2j}) & (x_{3n} - x_{3j})(u_{3n} - u_{3j}) \end{bmatrix}. \quad (3.25)$$

Then, transpose of the nonlocal deformation gradient becomes

$$\mathbf{F}^T = \mathbf{M}\mathbf{B} + \mathbf{I}. \quad (3.26)$$

Thus, the discretized nonlocal small strain tensor can be obtained as

$$\begin{aligned} \boldsymbol{\varepsilon} &= \frac{1}{2}(\mathbf{F} + \mathbf{F}^T) - \mathbf{I} \\ &= \frac{1}{2}((\mathbf{A}\mathbf{M} + \mathbf{I}) + (\mathbf{M}\mathbf{B} + \mathbf{I})) - \mathbf{I} \\ &= \frac{1}{2}(\mathbf{A}\mathbf{M} + \mathbf{M}\mathbf{B}). \end{aligned} \quad (3.27)$$

In two-dimensional space,

$$\begin{aligned} \begin{bmatrix} \varepsilon_{11} & \varepsilon_{12} \\ \varepsilon_{12} & \varepsilon_{22} \end{bmatrix} &= \frac{1}{2} \begin{bmatrix} A_{11} & A_{12} \\ A_{12} & A_{22} \end{bmatrix} \begin{bmatrix} M_{11} & M_{12} \\ M_{12} & M_{22} \end{bmatrix} + \frac{1}{2} \begin{bmatrix} M_{11} & M_{12} \\ M_{12} & M_{22} \end{bmatrix} \begin{bmatrix} B_{11} & B_{12} \\ B_{12} & B_{22} \end{bmatrix} \\ &= \frac{1}{2} \begin{bmatrix} A_{11}M_{11} + A_{12}M_{12} & A_{11}M_{12} + A_{12}M_{22} \\ A_{12}M_{11} + A_{22}M_{12} & A_{12}M_{12} + A_{22}M_{22} \end{bmatrix} \\ &\quad + \frac{1}{2} \begin{bmatrix} M_{11}B_{11} + M_{12}B_{12} & M_{11}B_{12} + M_{12}B_{22} \\ M_{12}B_{11} + M_{22}B_{12} & M_{12}B_{12} + M_{22}B_{22} \end{bmatrix}. \end{aligned}$$

Hence, the components of the small strain tensor can be obtained as:

$$\varepsilon_{11} = \frac{1}{2}(A_{11}M_{11} + A_{12}M_{12} + M_{11}B_{11} + M_{12}B_{12}) \quad (3.28a)$$

$$\varepsilon_{22} = \frac{1}{2}(A_{12}M_{12} + A_{22}M_{22} + M_{12}B_{12} + M_{22}B_{22}) \quad (3.28b)$$

$$\varepsilon_{12} = \frac{1}{2}(A_{11}M_{12} + A_{12}M_{22} + M_{11}B_{12} + M_{12}B_{22}). \quad (3.28c)$$

Under *plane stress* conditions, the stress tensor can be written as

$$\begin{bmatrix} \sigma_{11} \\ \sigma_{22} \\ \sigma_{12} \end{bmatrix} = \frac{E}{1-\nu^2} \begin{bmatrix} 1 & \nu & 0 \\ \nu & 1 & 0 \\ 0 & 0 & (1-\nu)/2 \end{bmatrix} \begin{bmatrix} \varepsilon_{11} \\ \varepsilon_{22} \\ 2\varepsilon_{12} \end{bmatrix}. \quad (3.29)$$

Under *plane strain* conditions, the stress tensor can be calculated as

$$\begin{bmatrix} \sigma_{11} \\ \sigma_{22} \\ \sigma_{12} \end{bmatrix} = \frac{E}{(1+\nu)(1-2\nu)} \begin{bmatrix} 1-\nu & \nu & 0 \\ \nu & 1-\nu & 0 \\ 0 & 0 & (1-2\nu)/2 \end{bmatrix} \begin{bmatrix} \varepsilon_{11} \\ \varepsilon_{22} \\ 2\varepsilon_{12} \end{bmatrix}. \quad (3.30)$$

Then, the first Piola-Kirchhoff stress tensor (PK1, \mathbf{P}) can be obtained by

$$\mathbf{P} = J\boldsymbol{\sigma}\mathbf{F}^{-T} \quad (3.31)$$

where J is the determinant of the deformation gradient.

3.2 Linear Piezoelectricity in Classical Continuum Mechanics

In this section, the constitutive equations and equation of motion of linear piezoelectricity in the classical continuum approach are presented. In the derivations of the governing equations, thermoelectrical coupling, known as the pyroelectric effect, is not considered. Also, higher-order coupling effects, as in the case of flexoelectricity, are neglected. In the following equations, the Einstein summation convention is used.

3.2.1 Constitutive equations

The sum of the mechanical and electric work done results in the total strain energy density, U , of the piezoelectric material. The differential form of the total strain energy density can be written in differential form as [113]

$$dU = \sigma_{ij}d\varepsilon_{ij} + E_m dD_m \quad (3.32)$$

where σ_{ij} and ε_{ij} are second-order mechanical stress and strain tensors, E_m is the electric field vector, and D_m is the electric displacement vector. The dielectric displacement vector is the total surface charge density that is induced in the material due to an applied electric field. The dielectric displacement field vector (represents a flux density), D_i , is obtained as

$$D_i = \varepsilon_0 E_i + P_i \quad (3.33)$$

where ε_0 is the vacuum permittivity equal to $8.854 \times 10^{-12} \text{ F/m}^2$ and P_i is the polarization vector induced by an applied electric field in a dielectric material. The unit of the polarization vector is coulombs per meter squared, $[\text{C/m}^2]$, and, for linear materials, it is given by

$$P_i = \mathcal{X}_{ij} E_j \quad (3.34)$$

where \mathcal{X}_{ij} is the dielectric susceptibility of the material, which is represented by a second-order tensor. Inserting Eq. (3.34) into (3.33) results in

$$D_i = \varepsilon_0 E_i + \mathcal{X}_{ij} E_j = (\varepsilon_0 \delta_{ij} + \mathcal{X}_{ij}) E_j = \chi_{ij} E_j \quad (3.35)$$

where δ_{ij} is Kronecker's delta and the dielectric permittivity of the material χ_{ij} is defined as

$$\chi_{ij} = \varepsilon_0 \delta_{ij} + \mathcal{X}_{ij}. \quad (3.36)$$

For most ferroelectric materials, the vacuum permittivity is much smaller than the dielectric susceptibility of the material, and hence $\chi_{ij} \approx \mathcal{X}_{ij}$. In practice, the relative dielectric permittivity κ_{ij} , or dielectric constant of the material, is more commonly used than dielectric permittivity χ_{ij} .

Due to electromechanical coupling, the stress field depends on the strain and the electric field; similarly, electrical displacement depends on the electric field as well as strain, i.e.

$$\sigma_{ij} = \sigma_{ij}(\varepsilon_{ij}, E_m) \quad (3.37a)$$

$$D_i = D_i(E_m, \varepsilon_{ij}) \quad (3.37b)$$

where the mechanical strain-displacement (u) and the electric field-potential (Φ) relations can be written as

$$\varepsilon_{ij} = \frac{1}{2} \left(\frac{\partial u_i}{\partial x_j} + \frac{\partial u_j}{\partial x_i} \right) \quad (3.38a)$$

$$E_i = -\frac{\partial \Phi}{\partial x_i} \quad (3.38b)$$

The differential stress and electric displacement can be expressed using a linear approximation as

$$d\sigma_{ij} = \left(\frac{\partial \sigma_{ij}}{\partial \varepsilon_{kl}} \right)_E d\varepsilon_{kl} + \left(\frac{\partial \sigma_{ij}}{\partial E_m} \right)_\varepsilon dE_m \quad (3.39a)$$

$$dD_m = \left(\frac{\partial D_m}{\partial \varepsilon_{kl}} \right)_E d\varepsilon_{kl} + \left(\frac{\partial D_m}{\partial E_k} \right)_\varepsilon dE_k \quad (3.39b)$$

where the first partial derivative term in the Eq. (3.39a) is the fourth-order elastic stiffness tensor, C_{ijkl} at a constant electric field, E . The second and the first partial derivatives in the Eqs. (3.39a) and (3.39b) are the third order piezoelectric coupling tensor, e_{ijm} . The second partial differential term in Eq. (3.39b) is the second-order dielectric permittivity tensor, χ_{mk} at a constant strain, ε . Hence, we have

$$\begin{aligned} \left(\frac{\partial \sigma_{ij}}{\partial \varepsilon_{kl}} \right)_E &= C_{ijkl} \\ \left(\frac{\partial \sigma_{ij}}{\partial E_m} \right)_\varepsilon &= - \left(\frac{\partial D_m}{\partial \varepsilon_{kl}} \right)_E = -e_{ijm} \\ \left(\frac{\partial D_m}{\partial E_k} \right)_\varepsilon &= \chi_{mk}. \end{aligned}$$

Integration of Eqs. (3.39a) and (3.39b) results in the constitutive equations of the linear piezoelectricity

$$\sigma_{ij} = C_{ijkl} \varepsilon_{kl} - e_{ijm} E_m \quad (3.40a)$$

$$D_m = e_{mij} \varepsilon_{ij} + \chi_{mk} E_k \quad (3.40b)$$

or in matrix form

$$\boldsymbol{\sigma} = \mathbb{C}^{\mathbf{E}} : \boldsymbol{\varepsilon} - \mathbf{e} \cdot \mathbf{E} \quad (3.41a)$$

$$\mathbf{D} = \mathbf{e} : \boldsymbol{\varepsilon} - \boldsymbol{\chi}^{\varepsilon} \cdot \mathbf{E}. \quad (3.41b)$$

While Eq. (3.40a) describes the converse or actuator effect where mechanical deformation occurs due to an applied electric field, Eq. (3.40b) describes the direct piezoelectric or sensor effect where an applied stress results in the polarization of the material and generating an electric field. Eq. (3.41) is called the stress-charge of the piezoelectric constitutive relations.

Alternatively, Eq. (3.41) can be written in its strain-charge form as

$$\varepsilon_{ij} = S_{ijkl}\sigma_{kl} + d_{ijm}E_m \quad (3.42a)$$

$$D_m = d_{mij}\sigma_{ij} + \chi_{mk}E_k \quad (3.42b)$$

or in matrix form

$$\boldsymbol{\varepsilon} = \mathbb{S}^{\mathbf{E}} : \boldsymbol{\sigma} + \mathbf{d} \cdot \mathbf{E} \quad (3.43a)$$

$$\mathbf{D} = \mathbf{d} : \boldsymbol{\sigma} + \boldsymbol{\chi}^{\sigma} \cdot \mathbf{E} \quad (3.43b)$$

where $\mathbb{S}^{\mathbf{E}}$ is the elastic compliance matrix under constant electric field, \mathbf{d} is the piezoelectric constants, and $\boldsymbol{\chi}^{\sigma}$ is the dielectric permittivity matrix under constant mechanical stresses. The material constants in between Eqs. (3.41) and (3.42) can be obtained by the following relations

$$\mathbb{S}^{\mathbf{E}} = (\mathbb{C}^{\mathbf{E}})^{-1} \quad (3.44a)$$

$$\mathbf{d} = \mathbf{e}(\mathbb{C}^{\mathbf{E}})^{-1} \quad (3.44b)$$

$$\boldsymbol{\chi}^{\sigma} = \boldsymbol{\chi}^{\varepsilon} + \mathbf{e}(\mathbb{C}^{\mathbf{E}})^{-1}(\mathbf{e})^T \quad (3.44c)$$

where $(\mathbf{e})^T$ is the transpose of the piezoelectric coupling tensor, and $(\mathbb{C}^{\mathbf{E}})^{-1}$ is the inverse of the elastic stiffness tensor.

Eq. (3.40) can be rewritten using Voight notation. In this notation pair of indices, ij are changed by a single index as follows

$$\begin{aligned}
11 &\rightarrow 1 \\
22 &\rightarrow 2 \\
33 &\rightarrow 3 \\
23 \text{ or } 32 &\rightarrow 4 \\
31 \text{ or } 13 &\rightarrow 5 \\
12 \text{ or } 21 &\rightarrow 6
\end{aligned}$$

So, Eq. (3.40) becomes [114]

$$\begin{bmatrix} \sigma_1 \\ \sigma_2 \\ \sigma_3 \\ \sigma_4 \\ \sigma_5 \\ \sigma_6 \end{bmatrix} = \begin{bmatrix} C_{11} & C_{12} & C_{13} & C_{14} & C_{15} & C_{16} \\ C_{21} & C_{22} & C_{23} & C_{24} & C_{25} & C_{26} \\ C_{31} & C_{32} & C_{33} & C_{34} & C_{35} & C_{36} \\ C_{41} & C_{42} & C_{43} & C_{44} & C_{45} & C_{46} \\ C_{51} & C_{52} & C_{53} & C_{54} & C_{55} & C_{56} \\ C_{61} & C_{62} & C_{63} & C_{64} & C_{65} & C_{66} \end{bmatrix} \begin{bmatrix} \varepsilon_1 \\ \varepsilon_2 \\ \varepsilon_3 \\ \varepsilon_4 \\ \varepsilon_5 \\ \varepsilon_6 \end{bmatrix} - \begin{bmatrix} e_{11} & e_{21} & e_{31} \\ e_{12} & e_{22} & e_{32} \\ e_{13} & e_{23} & e_{33} \\ e_{14} & e_{24} & e_{34} \\ e_{15} & e_{25} & e_{35} \\ e_{16} & e_{26} & e_{36} \end{bmatrix} \begin{bmatrix} E_1 \\ E_2 \\ E_3 \end{bmatrix} \quad (3.45a)$$

$$\begin{bmatrix} D_1 \\ D_2 \\ D_3 \end{bmatrix} = \begin{bmatrix} e_{11} & e_{12} & e_{13} & e_{14} & e_{15} & e_{16} \\ e_{21} & e_{22} & e_{23} & e_{24} & e_{25} & e_{26} \\ e_{31} & e_{32} & e_{33} & e_{34} & e_{35} & e_{36} \end{bmatrix} \begin{bmatrix} \varepsilon_1 \\ \varepsilon_2 \\ \varepsilon_3 \\ \varepsilon_4 \\ \varepsilon_5 \\ \varepsilon_6 \end{bmatrix} - \begin{bmatrix} \chi_{11} & \chi_{12} & \chi_{13} \\ \chi_{21} & \chi_{22} & \chi_{23} \\ \chi_{31} & \chi_{32} & \chi_{33} \end{bmatrix} \begin{bmatrix} E_1 \\ E_2 \\ E_3 \end{bmatrix} \quad (3.45b)$$

Polarized ceramics and hexagonal crystals in class 6mm are transversely isotropic [114], where the polling axis coincides with one of the material symmetry axes. Therefore, material properties in the directions perpendicular to the axis of isotropy are equal. For a transversely isotropic piezoelectric material, the number of independent material constants becomes 5, 3, and 2 for elastic, piezoelectric, and dielectric constants, respectively. For a ceramic poled in x_3 direction,

the material matrices in Eq. (3.45) yield [114]

$$\mathbf{C} = \begin{bmatrix} C_{11} & C_{12} & C_{13} & 0 & 0 & 0 \\ C_{21} & C_{11} & C_{13} & 0 & 0 & 0 \\ C_{31} & C_{31} & C_{33} & 0 & 0 & 0 \\ 0 & 0 & 0 & C_{44} & 0 & 0 \\ 0 & 0 & 0 & 0 & C_{44} & 0 \\ 0 & 0 & 0 & 0 & 0 & C_{66} \end{bmatrix}, \quad \text{where } C_{66} = \frac{C_{11} - C_{12}}{2} \quad (3.46a)$$

$$\mathbf{e} = \begin{bmatrix} 0 & 0 & 0 & 0 & e_{15} & 0 \\ 0 & 0 & 0 & e_{15} & 0 & 0 \\ e_{31} & e_{31} & e_{33} & 0 & 0 & 0 \end{bmatrix} \quad (3.46b)$$

$$\boldsymbol{\chi} = \begin{bmatrix} \chi_{11} & 0 & 0 \\ 0 & \chi_{11} & 0 \\ 0 & 0 & \chi_{33} \end{bmatrix} \quad (3.46c)$$

3.2.2 In-plane and anti-plane piezoelectric equations

Suppose that piezoelectric material has hexagonal symmetry with respect to x_3 axis and the poling axis is collinear with x_3 direction. Then, the material becomes isotropic on $x_1 - x_2$ plane.

Assume that there is an applied electric field or mechanical load on $x_1 - x_3$ plane, the nonzero electric fields are E_1, E_3 , and nonzero strain fields are $\epsilon_{11}, \epsilon_{33}, \epsilon_{13}$. Then, the constitutive relation reduces to the following form [113]

$$\begin{aligned} \sigma_{11} &= C_{11}u_{1,1} + C_{13}u_{1,3} - e_{31}E_3 \\ \sigma_{33} &= C_{13}u_{1,1} + C_{33}u_{1,3} - e_{33}E_3 \\ \sigma_{13} &= C_{44}u_{1,3} + C_{44}u_{3,1} - e_{15}E_1 \\ D_1 &= e_{15}u_{1,3} + e_{15}u_{3,1} + \chi_{11}E_1 \\ D_3 &= e_{31}u_{1,1} + e_{33}u_{3,3} + \chi_{33}E_3 \end{aligned} \quad (3.47)$$

In this case, it can be seen that both electric and mechanical displacement fields are in-plane.

This time, assume that the only nonzero mechanical displacement is u_3 , and the electric field is applied in $x_1 - x_2$ plane. Then, the constitutive relation becomes [113]

$$\begin{aligned}
 \sigma_{13} &= C_{44}u_{3,1} - e_{15}E_1 \\
 \sigma_{23} &= C_{44}u_{3,2} - e_{15}E_2 \\
 D_1 &= e_{15}u_{3,1} + \chi_{11}E_1 \\
 D_2 &= e_{15}u_{3,2} + \chi_{11}E_2
 \end{aligned} \tag{3.48}$$

This constitutive relation corresponds to the case where the displacement field is out of the plane, and the electric field is in the plane.

3.2.3 Governing equations of a piezoelectric continuum

It can be assumed that the electric field developed in piezoelectric materials is quasi-static because the velocity of elastic waves is much smaller than the velocity of electromagnetic waves [113]. Hence, the magnetic field caused by elastic waves can be neglected, which yields the time rate of change of the magnetic field as zero. From the Maxwell-Faraday equation, i.e.

$$\begin{aligned}
 \nabla \times \mathbf{E} &= -\frac{\partial \mathbf{B}}{\partial t} \\
 \nabla \times \mathbf{E} &= 0
 \end{aligned} \tag{3.49}$$

Because the electric field is irrotational, as shown in (3.49), it can be expressed as the gradient of a scalar electrostatic potential function, Φ . Moreover, the direction of the electric field is from high electric potential to low electric potential so that the electric field can be written as the negative of the gradient of the potential field, i.e.

$$\mathbf{E} = -\nabla\Phi \tag{3.50}$$

Therefore, the governing equations of a piezoelectric continuum can be written with the assumptions of the small deformations and quasi-electrostatic field as follows

$$\begin{aligned}\rho \ddot{\mathbf{u}} &= \nabla \cdot \boldsymbol{\sigma} + \mathbf{b} \\ \nabla \cdot \mathbf{D} &= q_{free}.\end{aligned}\tag{3.51}$$

where \mathbf{b} is the body force vector, ρ is the mass density, and q_{free} is the free electric volume charge.

3.3 Non-Ordinary State-Based Formulation for Linear Piezoelectricity

The electric potential scalar state is defined by

$$\underline{\Phi}[\mathbf{x}] \langle \xi \rangle = \phi' - \phi\tag{3.52}$$

The linear piezoelectricity peridynamics equations of equilibrium are obtained as

$$\int_{\mathcal{H}} \{ \underline{\mathbf{T}}[\mathbf{x}] \langle \xi \rangle - \underline{\mathbf{T}}[\mathbf{x}'] \langle \xi \rangle \} dV + \mathbf{b}(\mathbf{x}) = \mathbf{0}\tag{3.53a}$$

$$\int_{\mathcal{H}} \{ \underline{\mathbf{d}}[\mathbf{x}] \langle \xi \rangle - \underline{\mathbf{d}}[\mathbf{x}'] \langle \xi \rangle \} dV = 0\tag{3.53b}$$

where $\underline{\mathbf{T}}$ and $\underline{\mathbf{d}}$ are the PD force vector and electric displacement scalar states, respectively. The PD force vector state can be obtained through the Cauchy stress tensor and the PD electric displacement scalar state through the electric displacement vector. The Cauchy stress tensor and the electric displacement vectors are obtained using the constitutive relations presented for linear piezoelectricity as

$$\boldsymbol{\sigma} = \mathbb{C}^{\mathbf{E}} : \boldsymbol{\varepsilon} - \mathbf{e} \cdot \mathbf{E}\tag{3.54a}$$

$$\mathbf{D} = \mathbf{e} : \boldsymbol{\varepsilon} - \boldsymbol{\chi}^{\varepsilon} \cdot \mathbf{E}\tag{3.54b}$$

where $\mathbb{C}^{\mathbf{E}}$ is the fourth-order stiffness tensor at the constant electric field, \mathbf{e} is the piezoelectric coupling tensor, $\boldsymbol{\chi}^{\varepsilon}$ is the dielectric permittivity tensor at the constant strain field. The small strain tensor $\boldsymbol{\varepsilon}$ is given in (3.28a). The electric field vector \mathbf{E} is obtained by the nonlocal potential gradient (\mathbf{F}^{ϕ}), such that

$$\mathbf{E} = -\mathbf{F}^{\phi}\tag{3.55}$$

where

$$\mathbf{F}^\phi = \left(\int_{\mathcal{H}} \omega \underline{\Phi} \xi dV \right) \mathbf{K}^{-1} \quad (3.56)$$

Then, Eq. (3.56) can be discretized as

$$\mathbf{F}^\phi(\mathbf{x}_j) = \left[\sum_{n=1}^m \omega(|\mathbf{x}_n - \mathbf{x}_j|) \underline{\Phi}(\mathbf{x}_n - \mathbf{x}_j) \cdot (\mathbf{x}_n - \mathbf{x}_j) V_n \right] \mathbf{K}^{-1} \quad (3.57)$$

where m is the number of nodes in the neighborhood of \mathbf{x}_j , $\mathcal{H}_{\mathbf{x}_j}$. V_n is the volume associated with node n . The discrete version of the inverse of the shape tensor can be found in Eq. (3.17).

It is possible to rewrite Eqs. (3.54a) and (3.54b) in the following form

$$\boldsymbol{\sigma} = \boldsymbol{\sigma}_{uu} - \boldsymbol{\sigma}_{u\phi} \quad (3.58a)$$

$$\mathbf{D} = \mathbf{D}_{\phi u} - \mathbf{D}_{\phi\phi} \quad (3.58b)$$

which indicates the fully mechanical part of the stress ($\boldsymbol{\sigma}_{uu}$), the stress and the electric displacement components resulting from the electromechanical coupling ($\boldsymbol{\sigma}_{u\phi}$) and ($\mathbf{D}_{\phi u}$), respectively), and the fully electrical part of the electrical displacement vector ($\mathbf{D}_{\phi\phi}$).

Hence, the expressions for the PD vector state and for the PD electric displacement scalar state can be written as

$$\underline{\mathbf{T}}[\mathbf{x}]\langle \xi \rangle = \omega\langle \xi \rangle \boldsymbol{\sigma}_{uu}(\mathbf{x}) \mathbf{K}^{-1}(\mathbf{x}) \xi - \omega\langle \xi \rangle \boldsymbol{\sigma}_{u\phi}(\mathbf{x}) \mathbf{K}^{-1}(\mathbf{x}) \xi \quad (3.59a)$$

$$\underline{\mathbf{d}}[\mathbf{x}]\langle \xi \rangle = \omega\langle \xi \rangle (\mathbf{D}_{\phi u}(\mathbf{x}))^T (\mathbf{K}^{-1}(\mathbf{x}) \xi) - \omega\langle \xi \rangle (\mathbf{D}_{\phi\phi}(\mathbf{x}))^T (\mathbf{K}^{-1}(\mathbf{x}) \xi) \quad (3.59b)$$

The following algorithm provides a pseudo code to calculate global internal force vector for a linear piezoelectric solid.

Algorithm 4 Internal Force Calculation

```
1: ▷ Initialize the global force density to zero.
2: for each node  $i$  do
3:    $\mathbf{f}_i \leftarrow 0$ 
4: end for
5: ▷ Compute the pairwise contributions to the global force density vector.
6: for each node  $i$  do
7:   Calculate the shape tensor using Eq. (3.10) and calculate its inverse.
8:   Calculate the nonlocal deformation gradient tensor ( $\mathbf{F}$ ) using Eq. (3.13).
9:   Calculate the nonlocal potential gradient tensor ( $\mathbf{F}^\phi$ ) using Eq. (3.57).
10:   $\mathbf{E} \leftarrow -\mathbf{F}^\phi$ 
11:   $\boldsymbol{\varepsilon} \leftarrow \frac{1}{2}(\mathbf{F} + \mathbf{F}^T) - \mathbf{I}$ 
12:   $\sigma_{uu} \leftarrow \mathbb{C}^E : \boldsymbol{\varepsilon}$ 
13:   $\sigma_{u\phi} \leftarrow \mathbf{e} \cdot \mathbf{E}$ 
14:  for each neighbor node  $j$  for the node  $i$  do
15:     $\boldsymbol{\xi} \leftarrow \mathbf{x}_j - \mathbf{x}_i$ 
16:     $\boldsymbol{\eta} \leftarrow \mathbf{u}(\mathbf{x}_j) - \mathbf{u}(\mathbf{x}_i)$ 
17:    Calculate the nonuniform deformation state to use the stabilization technique [115]
18:     $\mathbf{z} \leftarrow \mathbf{Y} - \mathbf{F}\boldsymbol{\xi}$ 
19:     $\underline{\mathbf{T}}^s[\mathbf{x}]\langle\boldsymbol{\xi}\rangle \leftarrow \frac{1}{2}\omega\langle\boldsymbol{\xi}\rangle \mathbb{C} \mathbf{z}$ 
20:     $\underline{\mathbf{T}}[\mathbf{x}]\langle\boldsymbol{\xi}\rangle \leftarrow \omega\langle\boldsymbol{\xi}\rangle \sigma_{uu}(\mathbf{x}) \mathbf{K}^{-1}(\mathbf{x}) \boldsymbol{\xi} - \omega\langle\boldsymbol{\xi}\rangle \sigma_{u\phi}(\mathbf{x}) \mathbf{K}^{-1}(\mathbf{x}) \boldsymbol{\xi} + \underline{\mathbf{T}}^s[\mathbf{x}]\langle\boldsymbol{\xi}\rangle$ 
21:     $\underline{\mathbf{M}} \leftarrow \frac{\varepsilon + \eta}{|\varepsilon + \eta|}$ 
22:     $\mathbf{f}_i \leftarrow \mathbf{f}_i + \underline{\mathbf{T}} \underline{\mathbf{M}} V_j$ 
23:     $\mathbf{f}_j \leftarrow \mathbf{f}_j - \underline{\mathbf{T}} \underline{\mathbf{M}} V_i$ 
24:  end for
25: end for
```

3.4 An Implicit Formulation for Static Linear Piezoelectricity in Non-Ordinary State-Based Peridynamics

Eq. (3.53) can be solved in two different approaches. In the first case, an adaptive dynamic relaxation technique can be utilized to obtain the static response of the system. In the second case, an implicit formulation can be derived. Breitenfeld et al. [103] presented an implicit formulation of non-ordinary state-based peridynamic equations with only mechanical degrees of freedom. In 2021, Vieira and Araújo [102] extended this formulation for linear piezoelectricity problems. They used the bond-associated correspondence model developed by Chen [116] to prevent the zero-energy modes inherited from the non-ordinary state-based peridynamics. On the other hand, Littlewood [117] provided a detailed explanation of obtaining the tangent stiffness matrix for a nonlinear peridynamic system of equations. Here, this approach is extended to cover the linear piezoelectricity problems. The stabilized non-ordinary state-based peridynamic model proposed by Li et al. [115] is adopted in the force and electric displacement formulations.

The global system of linear equations can be written in the following form

$$\begin{bmatrix} K^{uu} & K^{u\phi} \\ K^{\phi u} & K^{\phi\phi} \end{bmatrix} \begin{bmatrix} \mathbf{u} \\ \phi \end{bmatrix} = - \begin{bmatrix} \mathbf{b} \\ 0 \end{bmatrix}. \quad (3.60)$$

The mechanical part of the tangent stiffness matrix, K^{uu} , provides the relation of the change in the global internal force with respect to an infinitesimal change of a displacement degree of freedom, i.e.

$$K_{ij}^{uu} = \frac{\partial f_i^{int}(\mathbf{u}, \phi)}{\partial u_j} \quad (3.61)$$

where K_{ij}^{uu} and f_i^{int} is the component of the tangent stiffness matrix's mechanical part and internal force, respectively. \mathbf{u} is the displacement vector, and u_j is its component. Littlewood [117] presents the central difference approximation of Eq. (3.61) as

$$K_{ij}^{uu} \approx \frac{f_i^{int}(\mathbf{u} + \gamma^j, \phi) - f_i^{int}(\mathbf{u} - \gamma^j, \phi)}{2\gamma} \quad (3.62)$$

where $f_i^{int}(\mathbf{u} + \gamma^j, \phi)$ is the component of the internal force due to a perturbed displacement vector

where a small number γ increases only its j^{th} component. Namely, $f_i^{\text{int}}(\mathbf{u} + \gamma^j, \phi)$ is the component of the internal force due to a positive perturbation of the j^{th} component of the displacement vector. Similarly, $f_i^{\text{int}}(\mathbf{u} - \gamma^j, \phi)$ is a component of the internal force vector resulting by a negative perturbation of the j^{th} component of the displacement vector. The amount of the perturbation, γ , is chosen as $1.0e^{-6}$ times the grid spacing.

The electrical part of the tangent stiffness matrix relates an infinitesimal change of an electric potential degree of freedom to the resulting change in the electric displacement vector. Hence, the electrical part of the tangent stiffness matrix can be obtained as

$$K_{ij}^{\phi\phi} \approx \frac{d_i^{\text{int}}(\mathbf{u}, \phi + \gamma^j) - d_i^{\text{int}}(\mathbf{u}, \phi - \gamma^j)}{2\gamma}. \quad (3.63)$$

In a similar way, the electromechanical coupling part of the tangent stiffness matrix is approximated as

$$K_{ij}^{u\phi} \approx \frac{f_i^{\text{int}}(\mathbf{u}, \phi + \gamma^j) - f_i^{\text{int}}(\mathbf{u}, \phi - \gamma^j)}{2\gamma}. \quad (3.64)$$

The applied loads are converted to body forces, \mathbf{b} , and inserted at the right-hand side of the Eq. (3.60). The essential boundary conditions are applied through a single layer of nodes and directly imposed on the global system of equations. The body forces are also applied to a single layer of peridynamic nodes. Eq. (3.60) is solved using a static condensation method for the unknown degrees of freedom.

3.5 Numerical Examples

In this section, two different electrostatic analyses are presented to demonstrate the capability of the coupled electromechanical formulation for non-ordinary state-based peridynamics. The previously mentioned in-house code is extended and used to solve the following problems. The size of the horizon is fixed to three times grid spacing through this section. Also, a third-order influence function is used within the internal force calculations in the following form

$$\omega(|\xi|) = 1 - 3 \left(\frac{|\xi|}{\delta} \right)^2 + 2 \left(\frac{|\xi|}{\delta} \right)^3. \quad (3.65)$$

3.5.1 A two-dimensional piezoelectric beam with an analytical solution

Fig. 3.1 presents a 2 mm by 1 mm rectangular piezoelectric strip exposed to bending and applied potential field. A transversely isotropic PZT-5 material has been polarized along its thickness direction (z-direction). The material properties are given in Table 3.1, where the components of the elastic compliance matrix under constant electric field and the dielectric permittivity under constant stress are shown with S^E and χ^σ , respectively. The material constants can be converted using Eq. (3.44) to obtain the constitutive relation in the stress-charge form.

Table 3.1: Material Properties of PZT-5 [69]

Elastic Compliance (mm ² /N)		Piezoelectric Constants (mm/C)		Dielectric Permittivity (N/V ²)	
S_{11}^E	16.4×10^{-6}	d_{31}	-172×10^{-9}	χ_{11}^σ	1.53105×10^{-8}
S_{13}^E	-7.22×10^{-6}	d_{33}	374×10^{-9}	χ_{33}^σ	1.505×10^{-7}
S_{33}^E	18.8×10^{-6}	d_{15}	584×10^{-9}		
S_{55}^E	47.5×10^{-6}				

As shown in Fig. 3.1, a voltage of $\phi = +10$ V is applied to the top surface. Whereas the bottom surfaces are subjected to a voltage of $\phi = -10$ V. A linearly varying bending stresses are applied to the sides of the problem domain in the following form

$$\sigma_x = \sigma_0 + \sigma_1 z \quad (3.66)$$

where $\sigma_0 = -5$ N/mm² and $\sigma_1 = 20$ N/mm³.

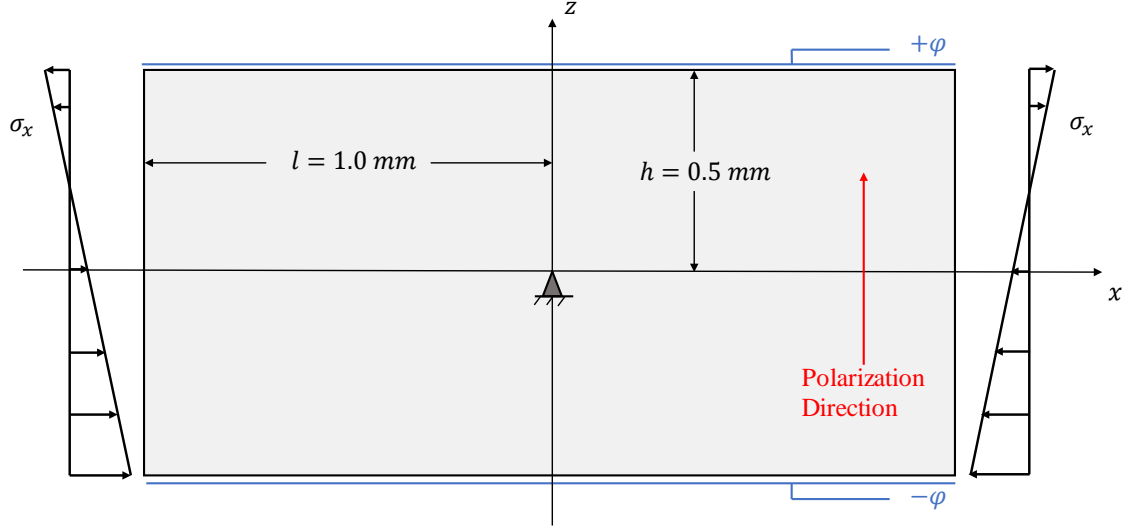


Figure 3.1: Problem setup: A two-dimensional PZT-5 strip. Adopted from [68].

The analytical solutions for the resulted displacements and potential field [69] are given as

$$u = S_{11}^E \left(\sigma_0 - \frac{d_{31}V_0}{S_{11}^E h} \right) + S_{11}^E \left(1 - \frac{d_{31}^2}{S_{11}^E \chi_{33}^\sigma} \right) \sigma_1 x z \quad (3.67a)$$

$$w = S_{13}^E \left(\sigma_0 - \frac{d_{33}V_0}{S_{13}^E h} \right) z + S_{13}^E \left(1 - \frac{d_{31}d_{33}}{S_{13}^E \chi_{33}^\sigma} \right) \sigma_1 \frac{z^2}{2} - S_{11}^E \left(1 - \frac{d_{31}^2}{S_{11}^E \chi_{33}^\sigma} \right) \sigma_1 \frac{x^2}{2} \quad (3.67b)$$

$$\phi = V_0 \frac{z}{h} - \frac{d_{31}\sigma_1}{2\chi_{33}^\sigma} (h^2 - z^2). \quad (3.67c)$$

Because the electric field is applied parallel with the poling axis, a shorting or elongation is expected depending on the direction of the applied electric field. The Poisson effect of this deformation also occurs in the horizon direction. In this case, the direction of the electric field is negative, resulting in a contraction in the vertical direction and expansion in the horizontal direction. The overall deformation of the piezoelectric strip is the superposition of deformation due to the applied mechanical stresses and the converse piezoelectric effects.

The mesh size used in this problem is 160×80 , and the horizon size is three times the grid spacing. The same grid and horizon size is used with [102] to compare our results with their PD results for the same problem.

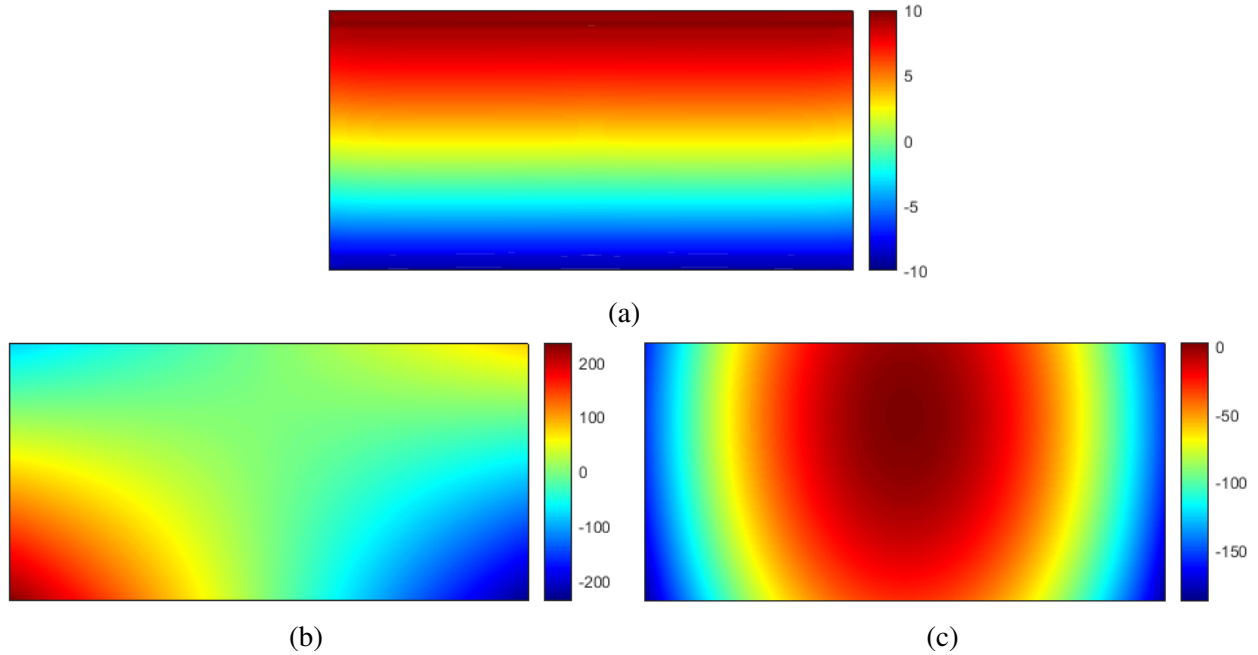


Figure 3.2: PD solutions for (a) ϕ [V], (b) u [nm], and (c) w [nm].

The electric potential distribution and horizontal and vertical displacement fields throughout the problem domain are illustrated in Fig. 3.2. Fig. 3.3 compares the comparison of the PD solutions of the current and Vieira and Araújo's [102] studies with the analytical ones along a vertical line of $x = 5$ mm. This study uses a single layer of nodes to apply both essential and natural boundary conditions. On the other hand, Vieira and Araújo [102] implement the essential boundary conditions within a thickness of the horizon layer of nodes. As a result, a slight deviation in both PD results is observed within the boundary zones.

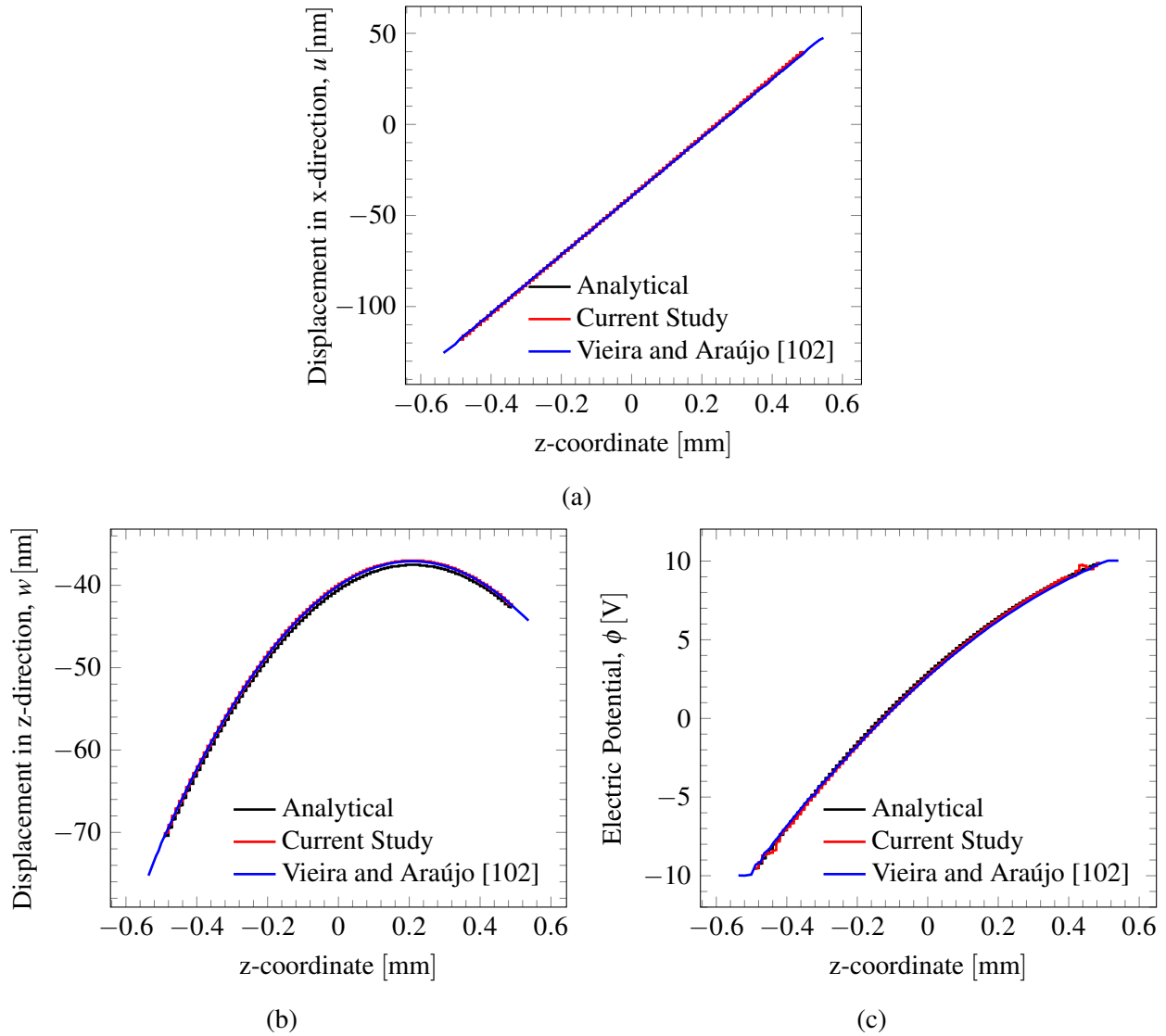


Figure 3.3: Comparison of the PD solutions along the $x = 0.5$ mm line (a) u , (b) w , and (c) ϕ

Fig. 3.4 compares the PD results with the analytical ones along the $0 \leq x \leq 0.5$ mm line. Electric potential results from the PD model show minor deviations from the analytical values. Due to the nonlocal nature of the PD modeling, a perfect match is not expected while comparing the results from the CCM. Although PD results converge to the ones from CCM as the horizon goes to zero, the horizon is selected as three times the grid spacing in the numerical computation. Moreover, the effect of the additional support located at the center of the plate affects the distribution of the electric potential along the $z = 0$ line. However, it is shown that both PD results agree well compared to the analytical solutions for the same size of mesh and horizon.

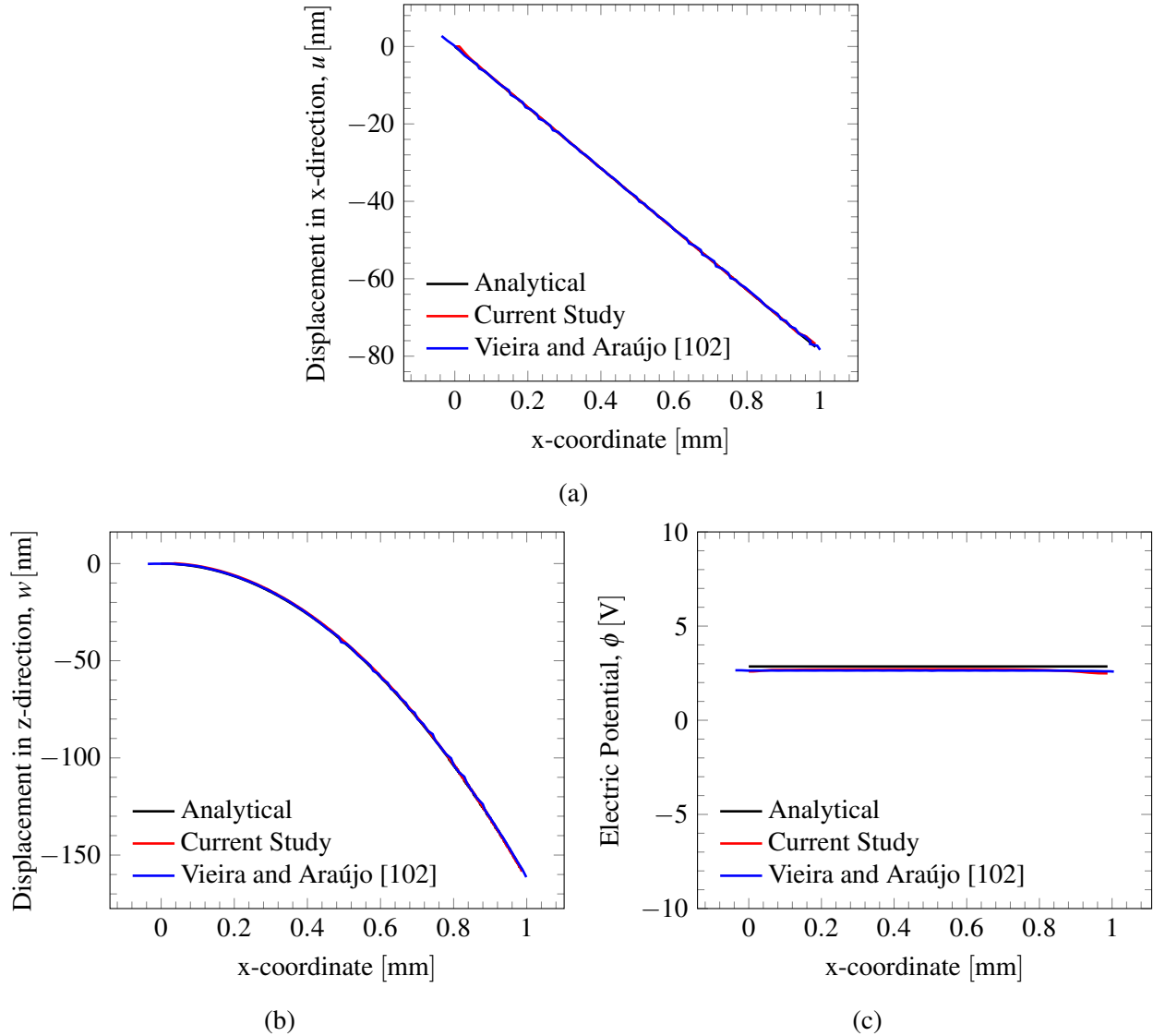


Figure 3.4: Comparison of the PD solutions along the $z = 0$ and $0 \leq x \leq 0.5$ mm line (a) u , (b) w , and (c) ϕ

3.5.2 A two-Dimensional piezoelectric strip with fixed-fixed boundaries

To further investigate the capabilities of the non-ordinary state-based peridynamic model for linear piezoelectricity, another two-dimensional piezoelectric domain, but this time with different boundary conditions, is investigated. Fig. 3.5 shows that 10 V electric potential is applied to the top surface of the domain, and zero potential is at the bottom. Both displacement components are fixed at the top and bottom surfaces. The material used for this example is PVDF, whose properties are given in Table 3.2. The resulted displacement fields and the potential are compared with the FEM results provided in [102].

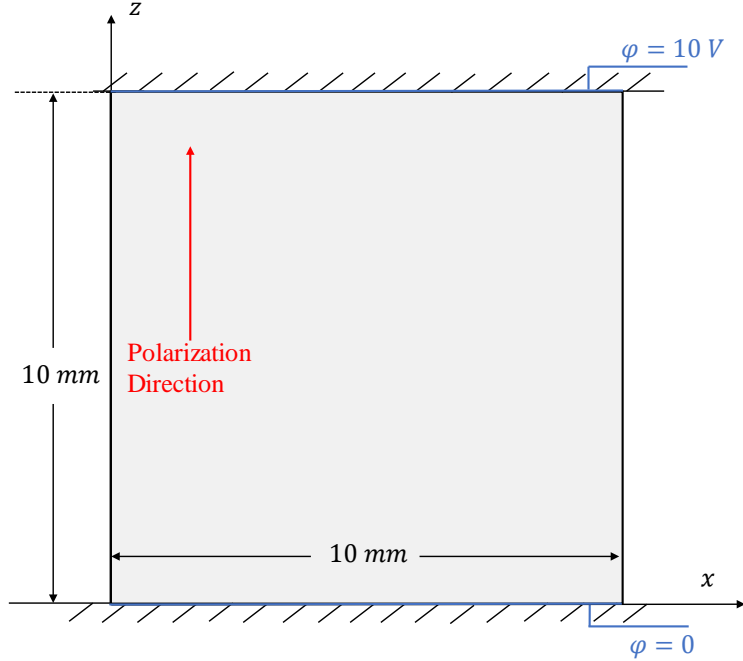


Figure 3.5: Problem setup: A two-dimensional PVDF strip. Adopted from [102].

Table 3.2: Material Properties of PVDF [102]

Elastic Constants [N/m ²]		Piezoelectric Coefficients [N/(V·m)]		Dielectric Permittivity [N/V ²]	
C_{11}^E	2.1836×10^9	e_{31}	-2.9042×10^{-2}	χ_{11}^E	1.0625×10^{-10}
C_{13}^E	6.3326×10^8	e_{33}	5.1578×10^{-2}	χ_{33}^E	1.0406×10^{-10}
C_{33}^E	2.1836×10^9				
C_{55}^E	7.7500×10^8				

The mesh size used in this problem is 80×80 nodes, and the horizon size is three times the grid spacing, which are same as the [102]. The electric potential, u , and w displacements distributions are presented in Fig. 3.6.

The comparison of the displacement fields along the $z = 2$ mm line is given in Fig. 3.7. Both PD results agrees very well with the FEM results for the horizontal displacement field. The current study results of the w -displacement along the $z = 2$ mm line shown in Fig. 3.7b have a better agreement than the PD results from [102]. However, a slight deviation from the FEM solutions is observed in the vertical displacement field results along the vertical line of $x = 5$ mm presented in Fig. 3.8a. The PD solution for the vertical displacement field provided by [102] exhibits strong oscillation close to the clamped boundaries. We suspect that either the zero-energy mode or the implicit formulation used in [102] may cause this oscillation problem. Our results shown with red

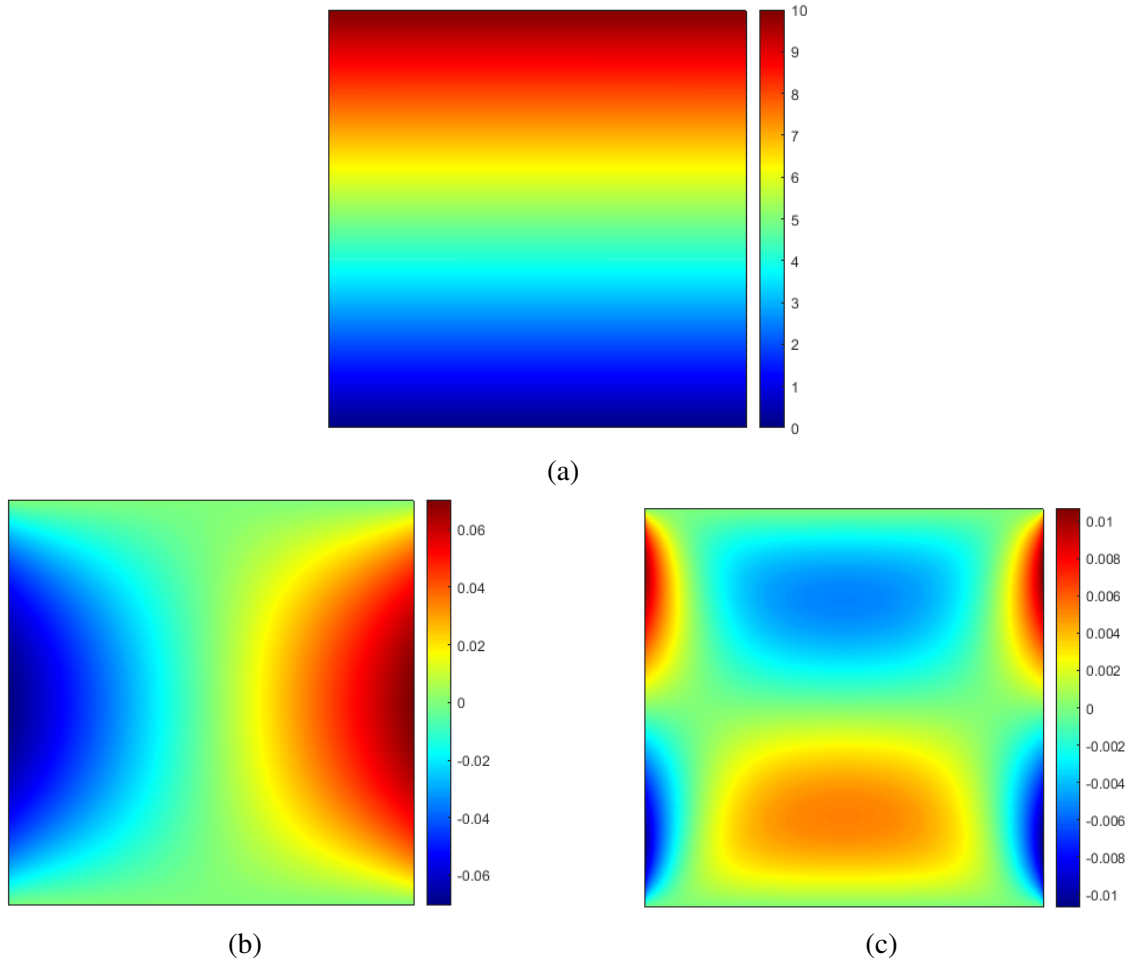


Figure 3.6: PD solutions for (a) ϕ [V], (b) u [nm], and (c) w [nm].

lines given in Fig. 3.8 do not exhibit oscillation close to the clamped boundaries. Furthermore, the electric potential field along the vertical lines agrees perfectly with each other, as shown in Fig. 3.8b.

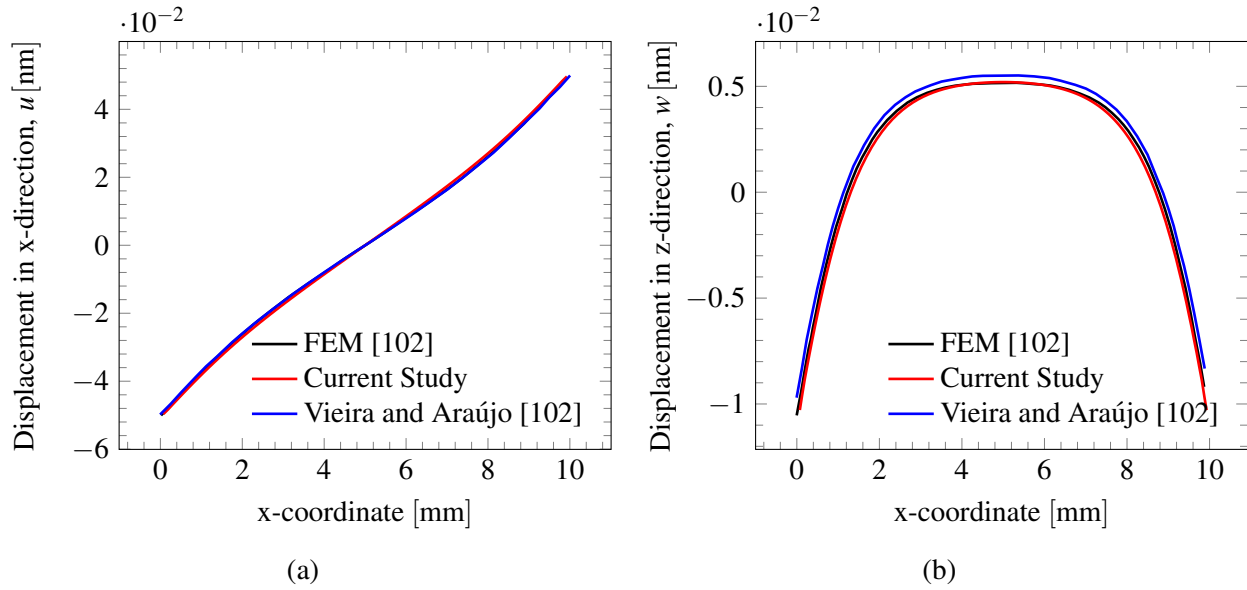


Figure 3.7: Comparison of the PD solutions along the $z = 2$ mm line (a) u , and (b) w .

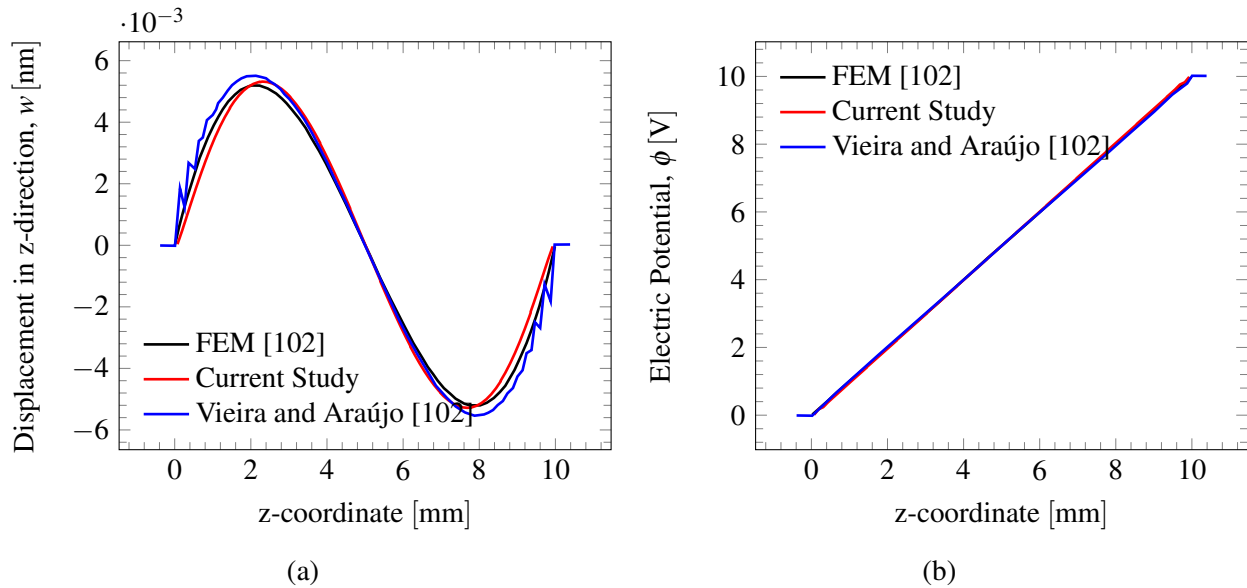


Figure 3.8: Comparison of the PD solutions along the $x = 5$ mm line (a) w , and (b) ϕ

3.5.3 A two-dimensional piezoelectric strip under compression and an applied electric field perpendicular to the poling axis

Fig. 3.9 shows a 1 mm by 1 mm rectangular PZT-5 strip under compressive stress along the vertical direction and an applied electric field along the horizontal direction. The material is polarized along the z -direction, as shown in Fig. 3.9, and its properties are provided in Table

3.1. Unlike the previous two examples, the applied electric field is perpendicular to the polarization direction, which causes a shear strain. Due to the uniform compression, the piezo strip is shortened in the z -direction and slightly expands in the x -direction due to Poisson's effect. Hence, the final deformation of the strip would be the superposition of the deformation due to shear strain and deformation caused by the compressive stress.

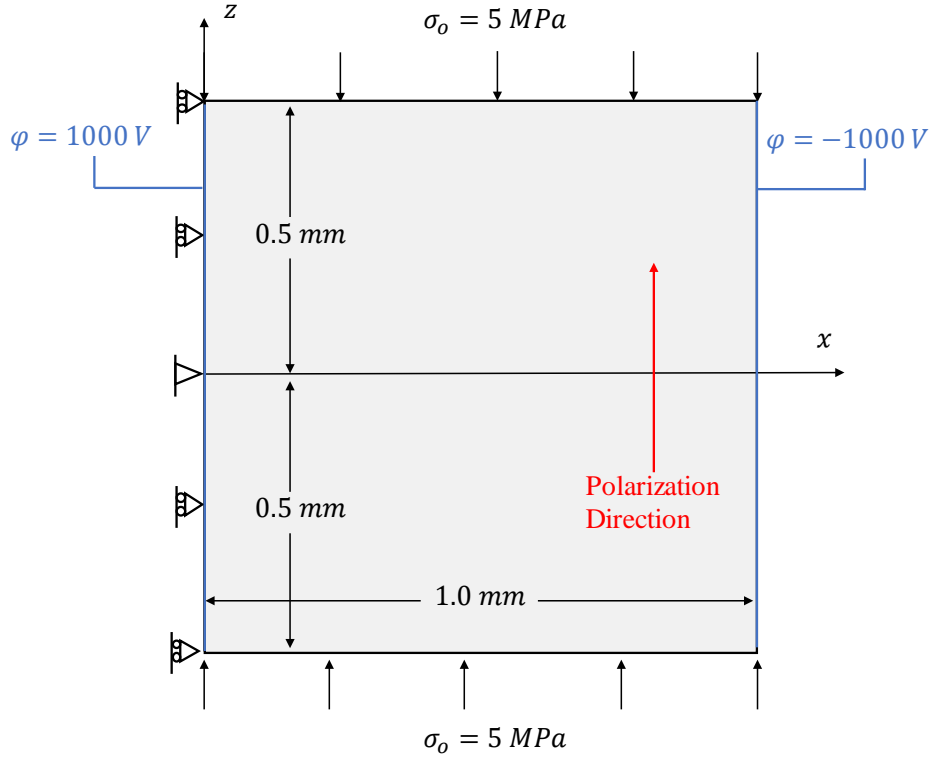


Figure 3.9: Problem setup: A two-dimensional PZT-5 strip under uniform compression. Adopted from [69].

The analytical solution of this problem is given as [69]

$$u = S_{13}^E \sigma_o x \quad (3.68a)$$

$$w = \frac{d_{15} V_0 x}{h} + S_{33}^E \sigma_o z \quad (3.68b)$$

$$\phi = V_0 \left(1 - 2 \frac{x}{L}\right) \quad (3.68c)$$

where $\sigma_o = -5 \text{ MPa}$, $V_0 = 1000 \text{ V}$, $h = 0.5 \text{ mm}$ and $L = 1 \text{ mm}$.

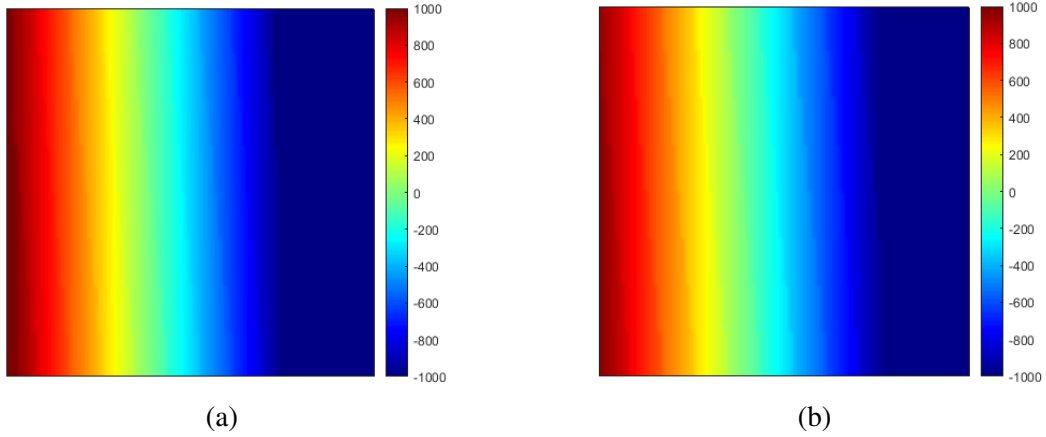


Figure 3.10: Distribution of (a) PD, and (b) exact solution for ϕ [V].

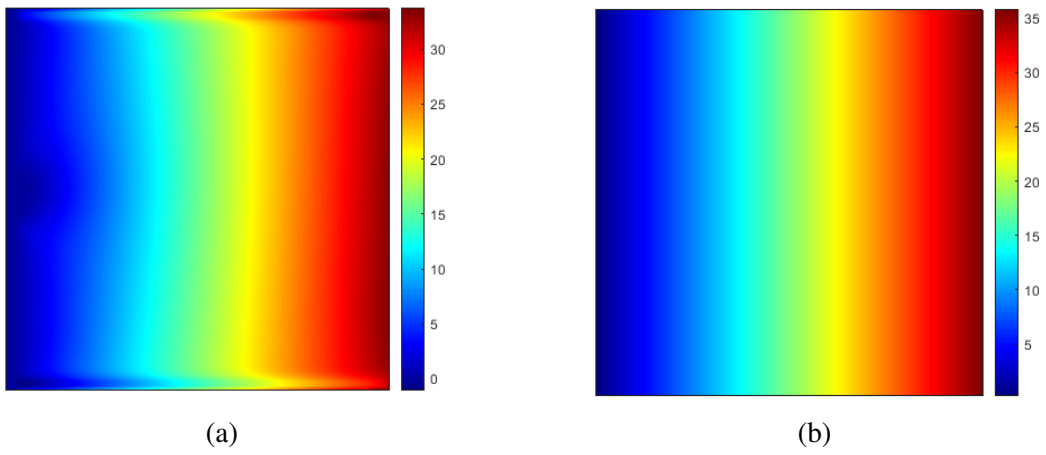


Figure 3.11: Distribution of (a) PD, and (b) exact solution for u [nm].

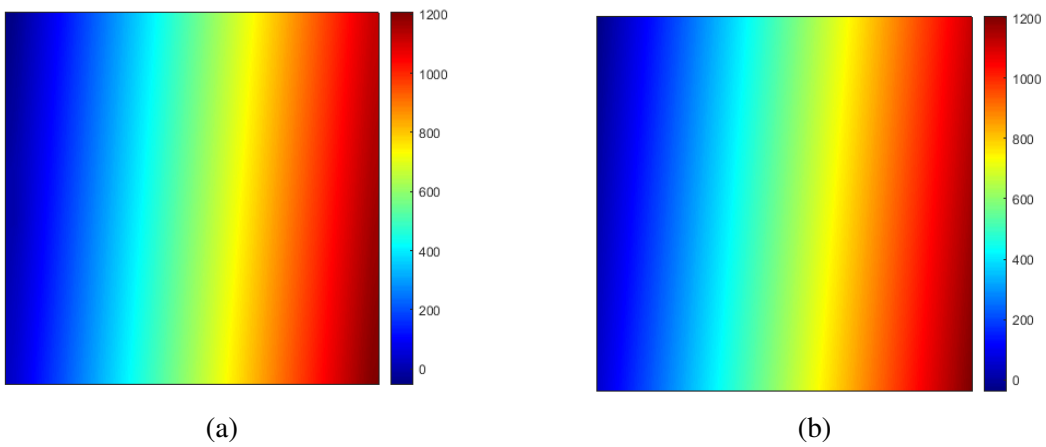


Figure 3.12: Distribution of (a) PD, and (b) exact solution for w [nm].

The PD and exact solutions of the electric potential, horizontal and vertical displacements

are shown in Figs. 3.10, 3.11, and 3.12, respectively. The hinge support located at point (0,0) is applied through a layer of horizon along the vertical axis in the PD simulation. Therefore, displacements around the origin are fixed through several nodes rather than a single node. The effect of this fixity is more visible in Fig. 3.11a. The magnitude of u -displacement is much smaller than the w -displacement because u -displacement results from the Poisson's effect of the compressive stress and the contribution of shearing from the applied electric field. Hence, it is apparent to see the effect of the boundary conditions in this case.

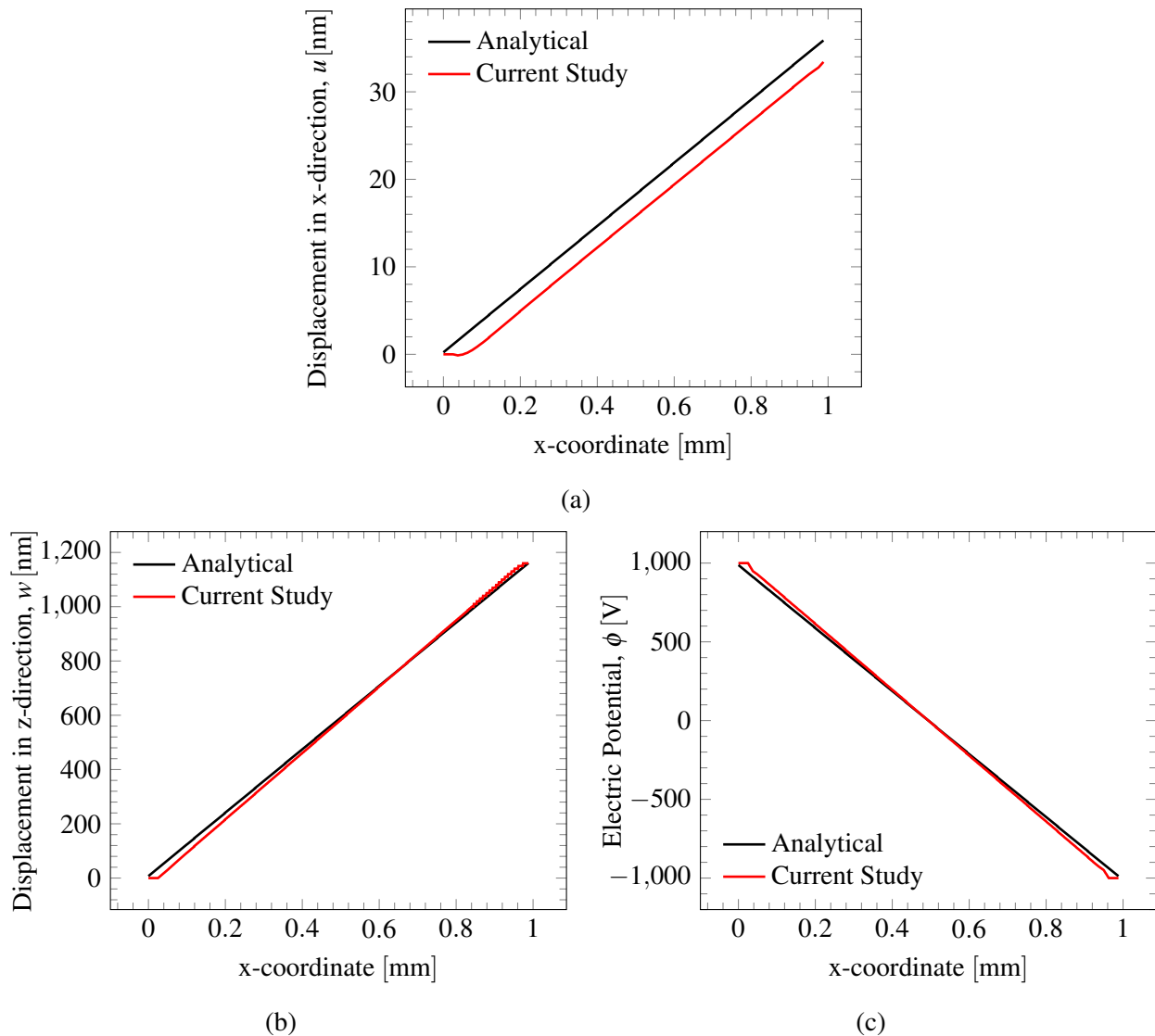


Figure 3.13: Comparison of the PD solutions along the $z = 0$ line (a) u , (b) w , and (c) ϕ

Fig. 3.13 and Fig. 3.14 present the PD and analytical results of ϕ , u , and w along the

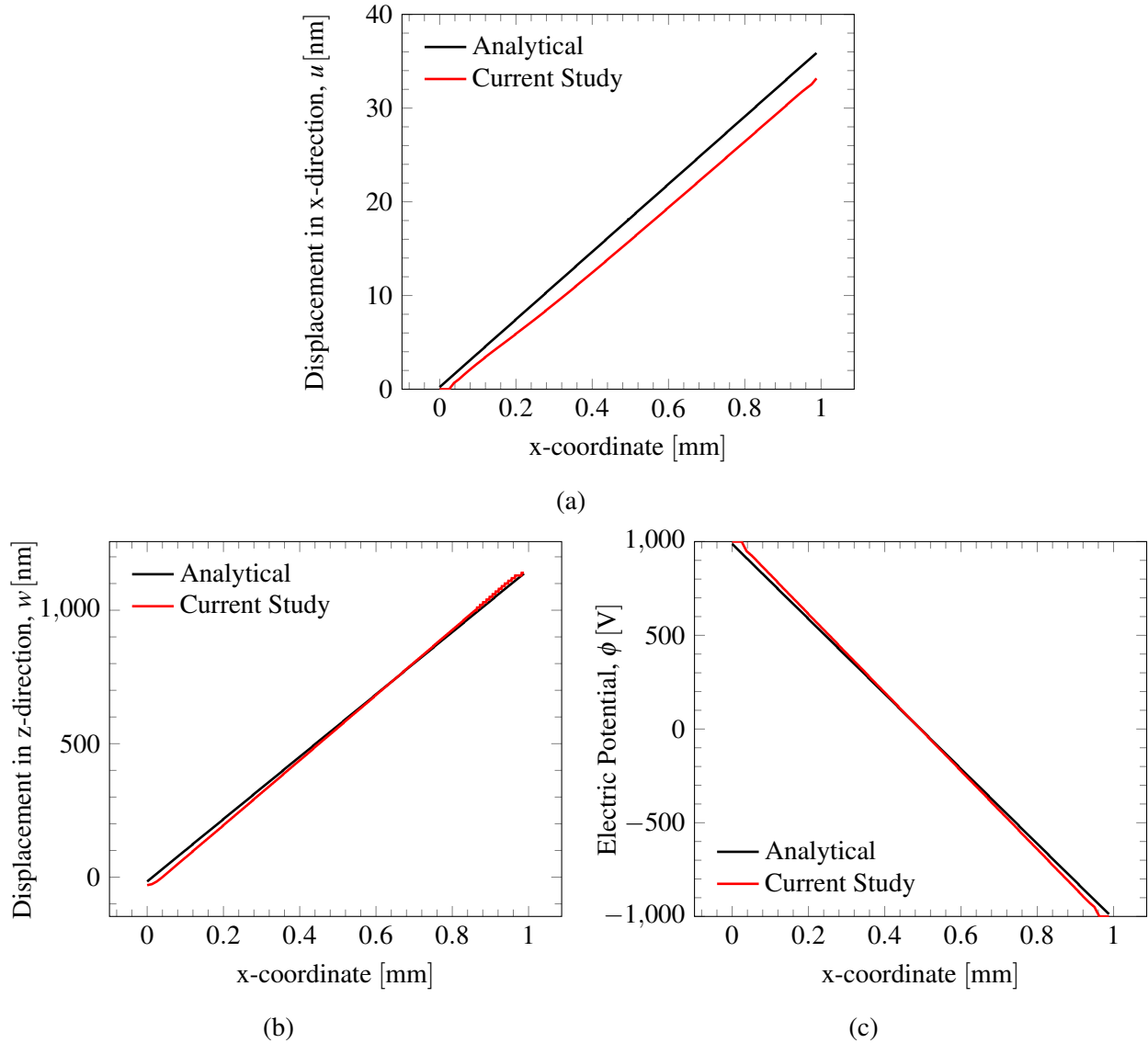


Figure 3.14: Comparison of the PD solutions along the $z = 0.25$ mm line (a) u , (b) w , and (c) ϕ

$z = 0$ and $z = 0.25$ mm lines, respectively. Due to the effects of boundary conditions explained in the previous paragraph, the horizontal displacements exhibit higher deviations from the analytical ones. However, it can be seen that the slopes of both PD and analytical distributions are pretty similar. The PD results are just shifted to the right due to the higher number of nodes fixed at the origin. On the other hand, the order of magnitudes of w -displacements is much higher than the u -displacement, and the PD results are in good agreement with the analytical ones. Similarly, electric potential distributions along two different horizon lines are shown in Figs. 3.13c and 3.14c match very well with the analytical results.

3.6 Chapter Summary

This chapter proposes an implicit formulation of non-ordinary state-based peridynamic for linear piezoelectricity. The tangent stiffness matrix is evaluated using a perturbation technique in this formulation. The capability of the proposed fully coupled electromechanical formulation is tested for three different numerical problems. In the first two problems, the electric field is applied parallel to the poling axis of the piezoelectric material, resulting in an axial strain in the poling direction as well as its Poisson effect in the transverse direction. In the last example, the electric field is applied perpendicular to the poling direction of the material, causing a shear strain. Furthermore, the different boundary conditions are selected for each problem to show the capability of the current model.

The PD solutions are compared with the reference solutions from the literature, either analytical or FEM, depending on which one is available. In addition, the results of the first two problems are also compared with another PD solution available in the literature. Those results show that the current implicit formulation agrees well with the analytical and FEM solutions. Hence, it is clearly shown that the current formulations can successfully model the fully coupled electromechanical behavior of piezoelectric structures.

CHAPTER 4

NOSB-PD WITH ELECTROMECHANICAL COUPLING FOR FRACTURE PROBLEMS

This chapter presents for the first time the fully coupled electromechanical simulations via NOSB-PD for crack propagation in brittle piezoelectric materials. For this purpose, an iterative solution procedure is followed to solve the coupled electromechanical system of equations. In this procedure, the electric potential field is obtained by utilizing the finite difference method which is explained in Chapter 4.2. Then, displacement fields are calculated by the adaptive dynamic relaxation (ADR) technique proposed by Kilic and Madenci [118]. The successive calculations for the potential and displacements fields continue until the convergence criteria is satisfied at each time step. The scope of this study is limited to covering the mode-I fracture.

4.1 A Brief Description of the Solution Procedure

The ADR technique provides a steady-state solution from the nonlinear system of equations by dampening the system. Therefore, an artificial mass and damping matrices are added to the system of equations such that

$$\mathcal{M}\ddot{\mathbf{u}} + c\mathcal{M}\dot{\mathbf{u}} = \mathbf{f} \quad (4.1)$$

where \mathbf{f} is the resultant force vector, \mathcal{M} is the fictitious diagonal density matrix and c is the damping coefficient that is changed adaptively at each time step. The details of the internal force calculations are provided in Algorithm 4. Using the central difference explicit integration, the displacements and velocities are obtained for the next iteration ($n + 1$) as

$$\dot{\mathbf{u}}^{n+1/2} = \left[(2 - c^n \Delta t) \dot{\mathbf{u}}^{n-1/2} + 2\Delta t \mathcal{M}^{-1} \mathbf{f}^n \right] / (2 + c^n \Delta t) \quad (4.2)$$

$$\mathbf{u}^{n+1} = \mathbf{u}^n + \Delta t \dot{\mathbf{u}}^{n+1/2} \quad (4.3)$$

$$c^{n+1} = 2 \sqrt{\frac{(\mathbf{u}^{n+1})^T [(\mathbf{f}^n - \mathbf{f}^{n+1}) \mathcal{M}^{-1} / (\Delta t \dot{\mathbf{u}}^{n+1/2})] \mathbf{u}^{n+1}}{(\mathbf{u}^{n+1})^T \mathbf{u}^{n+1}}}. \quad (4.4)$$

The first integration is started with

$$\dot{\mathbf{u}}^{1/2} = \Delta t \mathcal{M}^{-1} \mathbf{f}^0 / 2, \quad (4.5)$$

and $c^1 = 0$ due to unknown velocities at $t^{-1/}$. In addition, the damping coefficient is set to zero to avoid the division by zero that happens when we encounter zero velocity or displacement. Here, the time increment does not reflect a physical time because the mass and the damping matrices are also fictitious. Therefore, the time step size is preferred to be used as 1 for convenience [118].

The flowchart summarizing the iterative solution procedure at each time step is given in Fig. 4.1.

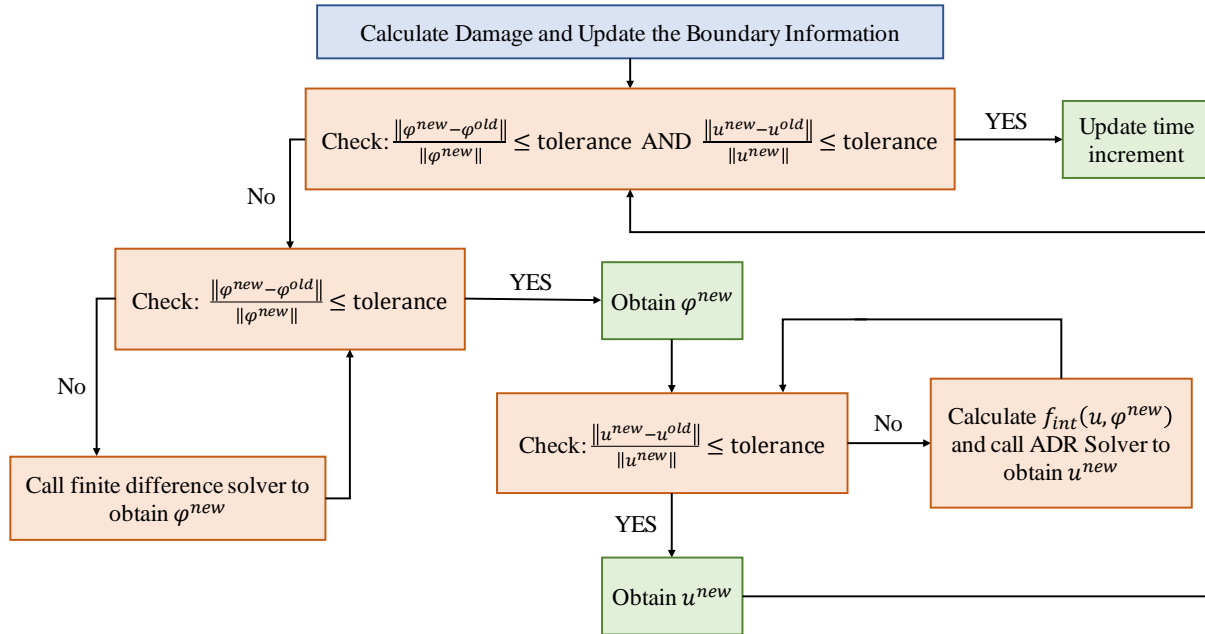


Figure 4.1: Implementation of the iterative solution at each time step for electromechanical system including fracture.

In this study, the critical stretch damage criteria given in Eq. (2.4) is used and the local damage at each node is calculated by using Eq. (2.5).

The boundary information stated in flowchart given in Fig. 4.1 includes the applied boundary conditions. In addition, as the crack extends, the new boundary nodes emerge. Because the crack surface is assumed to be electrically impermeable, the new crack surface is treated differently than the inner nodes, as explained in Chapter 4.2.

4.2 Finite Difference Discretization of Electrical Equilibrium Equation

For a piezoelectric material has hexagonal symmetry with respect to x_3 axis and the poling axis is collinear with this direction, the electric field can be written as:

$$\mathbf{E} = -\nabla\phi \quad \rightarrow \quad \begin{bmatrix} E_1 \\ E_3 \end{bmatrix} = - \begin{bmatrix} \frac{\partial\phi}{\partial x_1} \\ \frac{\partial\phi}{\partial x_3} \end{bmatrix} \quad (4.6)$$

Equation of the electrical equilibrium for a linear piezoelectric material then becomes:

$$\nabla \cdot \mathbf{D} = 0 \quad (4.7)$$

$$\frac{\partial D_1}{\partial x_1} + \frac{\partial D_3}{\partial x_3} = 0 \quad (4.8)$$

where the electrical displacement vector \mathbf{D} can be obtained as:

$$\mathbf{D} = \mathbf{e} : \boldsymbol{\varepsilon} + \boldsymbol{\chi}^\varepsilon \cdot \mathbf{E} \quad (4.9)$$

$$\begin{bmatrix} D_1 \\ D_3 \end{bmatrix} = \begin{bmatrix} 0 & 0 & e_{15} \\ e_{31} & e_{33} & 0 \end{bmatrix} \begin{bmatrix} \varepsilon_{11} \\ \varepsilon_{33} \\ \gamma_{13} \end{bmatrix} + \begin{bmatrix} \chi_{11}^\varepsilon & 0 \\ 0 & \chi_{33}^\varepsilon \end{bmatrix} \begin{bmatrix} E_1 \\ E_3 \end{bmatrix} \quad (4.10)$$

where \mathbf{E} , $\boldsymbol{\varepsilon}$, \mathbf{e} , and $\boldsymbol{\chi}^\varepsilon$ are represented as electric field, mechanical strain, piezoelectric coupling tensor and dielectric permittivity tensor under constant mechanical strains, respectively.

Inserting Eq. (4.6) into Eq. (4.10) results in

$$D_1 = e_{15}\gamma_{13} - \chi_{11}\frac{\partial\phi}{\partial x_1} \quad (4.11a)$$

$$D_3 = e_{31}\varepsilon_{11} + e_{33}\varepsilon_{33} - \chi_{33}\frac{\partial\phi}{\partial x_3} \quad (4.11b)$$

Then, Eq. (4.8) becomes

$$\left(e_{15}\frac{\partial\gamma_{13}}{\partial x_1} - \chi_{11}\frac{\partial^2\phi}{\partial x_1^2}\right) + \left(e_{31}\frac{\partial\varepsilon_{11}}{\partial x_3} + e_{33}\frac{\partial\varepsilon_{33}}{\partial x_3} - \chi_{33}\frac{\partial^2\phi}{\partial x_3^2}\right) = 0 \quad (4.12)$$

where

$$\frac{\partial D_1}{\partial x_1} = e_{15}\frac{\partial\gamma_{13}}{\partial x_1} - \chi_{11}\frac{\partial^2\phi}{\partial x_1^2} \quad (4.13a)$$

$$\frac{\partial D_3}{\partial x_3} = e_{31}\frac{\partial\varepsilon_{11}}{\partial x_3} + e_{33}\frac{\partial\varepsilon_{33}}{\partial x_3} - \chi_{33}\frac{\partial^2\phi}{\partial x_3^2} \quad (4.13b)$$

Hence, Eq. (4.8) can be rewritten as

$$\chi_{11}\frac{\partial^2\phi}{\partial x_1^2} + \chi_{33}\frac{\partial^2\phi}{\partial x_3^2} = e_{15}\frac{\partial\gamma_{13}}{\partial x_1} + e_{31}\frac{\partial\varepsilon_{11}}{\partial x_3} + e_{33}\frac{\partial\varepsilon_{33}}{\partial x_3} \quad (4.14)$$

Furthermore, the strain fields can be written in terms of displacements such that

$$\varepsilon_{11} = \frac{\partial u}{\partial x_1} \quad (4.15)$$

$$\varepsilon_{33} = \frac{\partial w}{\partial x_3} \quad (4.16)$$

$$\gamma_{13} = \left(\frac{\partial u}{\partial x_3} + \frac{\partial w}{\partial x_1}\right) \quad (4.17)$$

where u and w are the displacement fields in x_1 and x_3 directions, respectively. So, Eq. (4.14) can be expanded as

$$\chi_{11}\frac{\partial^2\phi}{\partial x_1^2} + \chi_{33}\frac{\partial^2\phi}{\partial x_3^2} = e_{15}\left(\frac{\partial^2 u}{\partial x_1\partial x_3} + \frac{\partial^2 w}{\partial x_1^2}\right) + e_{31}\frac{\partial^2 u}{\partial x_3\partial x_1} + e_{33}\frac{\partial^2 w}{\partial x_3^2} \quad (4.18)$$

A finite difference algorithm can be used to discretize the electrical equilibrium equation

given in Eq. (4.18). Central difference formula can be adopted to obtain using the grid given in Figure 4.2.

$$\frac{\partial^2 \phi}{\partial x_1^2} \approx \frac{1}{\Delta x_1 \Delta x_1} [\phi_{i+1,k} - 2\phi_{i,k} + \phi_{i-1,k}] \quad (4.19)$$

$$\frac{\partial^2 \phi}{\partial x_3^2} \approx \frac{1}{\Delta x_3 \Delta x_3} [\phi_{i,k+1} - 2\phi_{i,k} + \phi_{i,k-1}] \quad (4.20)$$

$$\frac{\partial^2 u}{\partial x_1 \partial x_3} \approx \frac{1}{4\Delta x_1 \Delta x_3} [u_{i+1,k+1} + u_{i-1,k-1} - u_{i+1,k-1} - u_{i-1,k+1}] \quad (4.21)$$

$$\frac{\partial^2 w}{\partial x_1^2} \approx \frac{1}{\Delta x_1 \Delta x_1} [w_{i+1,k} - 2w_{i,k} + w_{i-1,k}] \quad (4.22)$$

$$\frac{\partial^2 w}{\partial x_3^2} \approx \frac{1}{\Delta x_3 \Delta x_3} [w_{i,k+1} - 2w_{i,k} + w_{i,k-1}] \quad (4.23)$$

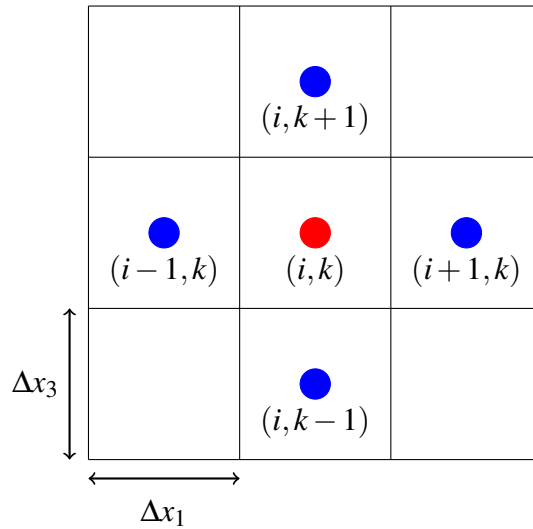


Figure 4.2: Mesh grid for finite difference stencil

Hence, for the **inner nodes** such as the node shown in red dot in Figure 4.2, the following equation holds:

$$\begin{aligned}
& \frac{\chi_{11}}{\Delta x_1 \Delta x_1} [\phi_{i+1,k} - 2\phi_{i,k} + \phi_{i-1,k}] + \frac{\chi_{22}}{\Delta x_3 \Delta x_3} [\phi_{i,k+1} - 2\phi_{i,k} + \phi_{i,k-1}] \\
&= \frac{e_{15}}{4\Delta x_1 \Delta x_3} [u_{i+1,k+1} + u_{i-1,k-1} - u_{i+1,k-1} - u_{i-1,k+1}] + \frac{e_{15}}{\Delta x_1 \Delta x_1} [w_{i+1,k} - 2w_{i,k} + w_{i-1,k}] \\
&+ \frac{e_{31}}{4\Delta x_1 \Delta x_3} [u_{i+1,k+1} + u_{i-1,k-1} - u_{i+1,k-1} - u_{i-1,k+1}] + \frac{e_{33}}{\Delta x_3 \Delta x_3} [w_{i,k+1} - 2w_{i,k} + w_{i,k-1}]
\end{aligned} \tag{4.24}$$

which can written as:

$$\begin{aligned}
\left(\frac{2\chi_{11}}{\Delta x_1 \Delta x_1} + \frac{2\chi_{33}}{\Delta x_3 \Delta x_3} \right) \phi_{i,k} &= \frac{\chi_{11}}{\Delta x_1 \Delta x_1} [\phi_{i+1,k} + \phi_{i-1,k}] + \frac{\chi_{33}}{\Delta x_3 \Delta x_3} [\phi_{i,k+1} + \phi_{i,k-1}] \\
&- \frac{e_{15}}{4\Delta x_1 \Delta x_3} [u_{i+1,k+1} + u_{i-1,k-1} - u_{i+1,k-1} - u_{i-1,k+1}] \\
&- \frac{e_{15}}{\Delta x_1 \Delta x_1} [w_{i+1,k} - 2w_{i,k} + w_{i-1,k}] \\
&- \frac{e_{31}}{4\Delta x_1 \Delta x_3} [u_{i+1,k+1} + u_{i-1,k-1} - u_{i+1,k-1} - u_{i-1,j+1}] \\
&- \frac{e_{33}}{\Delta x_3 \Delta x_3} [w_{i,k+1} - 2w_{i,k} + w_{i,k-1}].
\end{aligned} \tag{4.25}$$

Let's call the contribution of the strain field resulted in the right hand side of the Eq. 4.25 as the forcing term $F(i, k)$, i.e.

$$\begin{aligned}
F(i, k) &= \frac{e_{15}}{4\Delta x_1 \Delta x_3} [u_{i+1,k+1} + u_{i-1,k-1} - u_{i+1,k-1} - u_{i-1,k+1}] + \frac{e_{15}}{\Delta x_1 \Delta x_1} [w_{i+1,k} - 2w_{i,k} + w_{i-1,k}] \\
&+ \frac{e_{31}}{4\Delta x_1 \Delta x_3} [u_{i+1,k+1} + u_{i-1,k-1} - u_{i+1,k-1} - u_{i-1,j+1}] + \frac{e_{33}}{\Delta x_3 \Delta x_3} [w_{i,k+1} - 2w_{i,k} + w_{i,k-1}]
\end{aligned} \tag{4.26}$$

Hence, Eq. 4.25 becomes

$$\left(\frac{2\chi_{11}}{\Delta x_1 \Delta x_1} + \frac{2\chi_{33}}{\Delta x_3 \Delta x_3} \right) \phi_{i,k} = \frac{\chi_{11}}{\Delta x_1 \Delta x_1} [\phi_{i+1,k} + \phi_{i-1,k}] + \frac{\chi_{33}}{\Delta x_3 \Delta x_3} [\phi_{i,k+1} + \phi_{i,k-1}] - F(i, k) \tag{4.27}$$

There is no need to solve any equations for the nodes where essential boundary conditions are applied. The values of the electric potentials are directly used as they are given. On the other hand, if there exists any natural boundary conditions, additional equations are written and can be discretized using appropriate finite difference method. Let's consider the following problem:

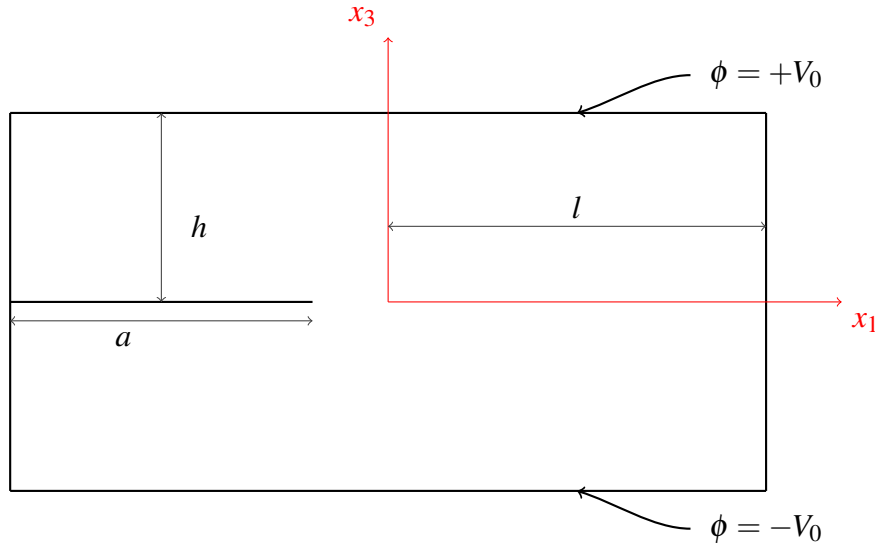


Figure 4.3: Pre-notched rectangular plate

The following boundary conditions apply for the problem:

At $x_3 = \pm h$, $\phi = \pm V_0$

At $x_1 = \pm l$, $D_1 = 0$

Along the pre-notch, $D_3 = 0$

As shown in Figure 4.3, the essential boundary conditions are given along the top and the bottom edges. Therefore, the electric potential values are directly assigned to the values given above. Along the left and the right edges as well as along the pre-notch, the given natural boundary conditions can be used to derive the required equations to solve the potentials along those locations.

Horizontal component of the electric displacement vector is obtained as:

$$D_1 = e_{15}\gamma_{13} - \chi_{11} \frac{\partial \phi}{\partial x_1} \quad (4.28)$$

Inserting the shear strain yields

$$D_1 = e_{15} \left(\frac{\partial u}{\partial x_3} + \frac{\partial w}{\partial x_1} \right) - \chi_{11} \frac{\partial \phi}{\partial x_1} \quad (4.29)$$

Now, we can discretization of the Eq. (4.29) using finite difference stencil. Along the left edge of the problem domain, i.e. $x_1 = -l$ and $-h \leq x_3 \leq h$:

$$\frac{\partial u}{\partial x_3} \approx \frac{u_{i,k+1} - u_{i,k-1}}{2\Delta x_3} \quad (4.30)$$

$$\frac{\partial w}{\partial x_1} \approx \frac{w_{i+1,k} - w_{i,k}}{\Delta x_1} \quad (4.31)$$

$$\frac{\partial \phi}{\partial x_1} \approx \frac{\phi_{i+1,k} - \phi_{i,k}}{\Delta x_1} \quad (4.32)$$

where first derivative of the vertical displacement field with respect to x_3 is approximated using the central difference; whereas the first derivative of the horizontal displacement field and the electric potential with respect to horizontal axis is approximated by the forward finite difference. Therefore, Eq. (4.29) becomes

$$D_1 = e_{15} \left(\frac{u_{i,k+1} - u_{i,k-1}}{2\Delta x_3} + \frac{w_{i+1,k} - w_{i,k}}{\Delta x_1} \right) - \chi_{11} \frac{\phi_{i+1,k} - \phi_{i,k}}{\Delta x_1} \quad (4.33)$$

which results in

$$\phi_{i,k} = \phi_{i+1,k} - \frac{\Delta x_1}{\chi_{11}} \left[e_{15} \left(\frac{u_{i,k+1} - u_{i,k-1}}{2\Delta x_3} + \frac{w_{i+1,k} - w_{i,k}}{\Delta x_1} \right) - D_1 \right] \quad (4.34)$$

where $D_1 = 0$. The second term of the Eq. 4.34 can be called as a forcing term. Then, forcing term for a left edge node becomes

$$F(i,k) = e_{15} \left(\frac{u_{i,k+1} - u_{i,k-1}}{2\Delta x_3} + \frac{w_{i+1,k} - w_{i,k}}{\Delta x_1} \right) - D_1. \quad (4.35)$$

Similarly, along the right edge of the problem domain, i.e. $x_1 = l$ and $-h \leq x_3 \leq h$, the first order derivatives can be approximated as:

$$\frac{\partial u}{\partial x_3} \approx \frac{u_{i,k+1} - u_{i,k-1}}{2\Delta x_3} \quad (4.36)$$

$$\frac{\partial w}{\partial x_1} \approx \frac{w_{i,k} - w_{i-1,k}}{\Delta x_1} \quad (4.37)$$

$$\frac{\partial \phi}{\partial x_1} \approx \frac{\phi_{i,k} - \phi_{i-1,k}}{\Delta x_1} \quad (4.38)$$

where first derivative of the vertical displacement field with respect to x_3 is approximated using the central difference; whereas the first derivative of the horizontal displacement field and the electric potential with respect to horizontal axis is approximated by the backward finite difference. Therefore, Eq. (4.29) becomes

$$D_1 = e_{15} \left(\frac{u_{i,k+1} - u_{i,k-1}}{2\Delta x_3} + \frac{w_{i,k} - w_{i-1,k}}{\Delta x_1} \right) - \chi_{11} \frac{\phi_{i,k} - \phi_{i-1,k}}{\Delta x_1} \quad (4.39)$$

which results in

$$\phi_{i,k} = \phi_{i-1,k} + \frac{\Delta x_1}{\chi_{11}} \left[e_{15} \left(\frac{u_{i,k+1} - u_{i,k-1}}{2\Delta x_3} + \frac{w_{i,k} - w_{i-1,k}}{\Delta x_1} \right) - D_1 \right] \quad (4.40)$$

where $D_1 = 0$. The last term of the Eq. 4.40 can be called as a forcing term. Then, forcing term for a right edge node becomes

$$F(i,k) = e_{15} \left(\frac{u_{i,k+1} - u_{i,k-1}}{2\Delta x_3} + \frac{w_{i,k} - w_{i-1,k}}{\Delta x_1} \right) - D_1. \quad (4.41)$$

The electric displacement in x_3 -direction shall be discretized to obtain the equations for electric potential along the prenotch. As given in Eq. (4.11b);

$$D_3 = e_{31}\epsilon_{11} + e_{33}\epsilon_{33} - \chi_{33} \frac{\partial \phi}{\partial x_3} \quad (4.42)$$

Inserting the normal strains in 1 and 3 directions yields

$$D_3 = e_{31} \frac{\partial u}{\partial x_1} + e_{33} \frac{\partial w}{\partial x_3} - \chi_{33} \frac{\partial \phi}{\partial x_3} \quad (4.43)$$

Along the top edge of the prenotch, the first order derivatives can be expressed as:

$$\frac{\partial u}{\partial x_1} \approx \frac{u_{i+1,k} - u_{i-1,k}}{2\Delta x_1} \quad (4.44)$$

$$\frac{\partial w}{\partial x_3} \approx \frac{w_{i,k+1} - w_{i,k}}{\Delta x_3} \quad (4.45)$$

$$\frac{\partial \phi}{\partial x_3} \approx \frac{\phi_{i,k+1} - \phi_{i,k}}{\Delta x_3} \quad (4.46)$$

where first derivatives of the variables w and ϕ with respect to vertical axis are calculate using forward finite difference, on the other hand the first derivative of the horizontal displacement field with respect to x_1 is approximated using central difference. Therefore, Eq. (4.43) becomes

$$D_3 = e_{31} \frac{u_{i+1,k} - u_{i-1,k}}{2\Delta x_1} + e_{33} \frac{w_{i,k+1} - w_{i,k}}{\Delta x_3} - \chi_{33} \frac{\phi_{i,k+1} - \phi_{i,k}}{\Delta x_3} \quad (4.47)$$

which results in

$$\phi_{i,k} = \phi_{i,k+1} - \frac{\Delta x_3}{\chi_{33}} \left[e_{31} \frac{u_{i+1,k} - u_{i-1,k}}{2\Delta x_1} + e_{33} \frac{w_{i,k+1} - w_{i,k}}{\Delta x_3} - D_3 \right] \quad (4.48)$$

where $D_3 = 0$. Then, forcing term for a bottom edge node becomes

$$F(i,k) = e_{31} \frac{u_{i+1,k} - u_{i-1,k}}{2\Delta x_1} + e_{33} \frac{w_{i,k+1} - w_{i,k}}{\Delta x_3} - D_3. \quad (4.49)$$

In a similar fashion, along the bottom edge of the pre-notch, first order derivatives can be approximated as:

$$\frac{\partial u}{\partial x_1} \approx \frac{u_{i+1,k} - u_{i-1,k}}{2\Delta x_1} \quad (4.50)$$

$$\frac{\partial w}{\partial x_3} \approx \frac{w_{i,k} - w_{i,kj-1}}{\Delta x_3} \quad (4.51)$$

$$\frac{\partial \phi}{\partial x_1} \approx \frac{\phi_{i,k} - \phi_{i,k-1}}{\Delta x_3} \quad (4.52)$$

where first derivatives of the variables w and ϕ with respect to vertical axis are calculated using backward finite difference, on the other hand the first derivative of the horizontal displacement

field with respect to x_1 is approximated using central difference. Therefore, Eq. (4.43) becomes

$$D_3 = e_{31} \frac{u_{i+1,k} - u_{i-1,k}}{2\Delta x_1} + e_{33} \frac{w_{i,k} - w_{i,k-1}}{\Delta x_3} - \chi_{33} \frac{\phi_{i,k} - \phi_{i,k-1}}{\Delta x_3} \quad (4.53)$$

which yield:

$$\phi_{i,k} = \phi_{i,k-1} + \frac{\Delta x_3}{\chi_{33}} \left[e_{31} \frac{u_{i+1,k} - u_{i-1,k}}{2\Delta x_1} + e_{33} \frac{w_{i,k} - w_{i,k-1}}{\Delta x_3} - D_3 \right] \quad (4.54)$$

where $D_3 = 0$. So, forcing term for a top edge node becomes

$$F(i,k) = e_{31} \frac{u_{i+1,k} - u_{i-1,k}}{2\Delta x_1} + e_{33} \frac{w_{i,k} - w_{i,k-1}}{\Delta x_3} - D_3. \quad (4.55)$$

4.2.1 Iterative solution technique for the electric potential field

Electric equilibrium equations can be solved using iterative techniques which are usually preferred to obtain a solution from a large system of simultaneous equations. Jacobi iteration, Gauss-Seidel and successive over-relaxation (SOR) methods are the most common iterative solution techniques that can also be used for this purpose. SOR method is chosen for faster convergence compared to others [119].

To apply SOR technique to Eq. (4.27), let's first write the equation in the following form

$$\phi_{i,k} = \frac{c_2}{c_1} (\phi_{i+1,k} + \phi_{i-1,k}) + \frac{c_3}{c_1} (\phi_{i,k+1} + \phi_{i,k-1}) - \frac{F(i,k)}{c_1} \quad (4.56)$$

where

$$c_1 = \left(\frac{2\chi_{11}}{\Delta x_1 \Delta x_1} + \frac{2\chi_{33}}{\Delta x_3 \Delta x_3} \right) \quad (4.57)$$

$$c_2 = \frac{\chi_{11}}{\Delta x_1 \Delta x_1} \quad (4.58)$$

$$c_3 = \frac{\chi_{33}}{\Delta x_3 \Delta x_3}. \quad (4.59)$$

Then, the residual at node (i,k) can be defined as:

$$R(i, k) = \frac{c_2}{c_1} (\phi_{i+1, k} + \phi_{i-1, k}) + \frac{c_3}{c_1} (\phi_{i, k+1} + \phi_{i, k-1}) - \frac{F(i, k)}{c_1} - \phi_{i, k} \quad (4.60)$$

where the forcing term for an inner node is given in Eq. (4.26).

As the residual approaches to zero, the results from the previous iteration step converge to the correct value at the new step. So, the residual given in Eq. (4.60) can be used as a correction term to find the new values of the potential field at node (i, k) . In the successive relaxation technique, the residual is multiplied with a factor called relaxation parameter, ω , and added to $\phi_{i, k}$ at the n^{th} iteration to obtain its value at the $(n+1)^{th}$ iteration with an increased rate of convergence.

$$\phi_{i, k}^{n+1} = \phi_{i, k}^n + \omega R^n(i, k) \quad (4.61)$$

The value of the relaxation parameter is selected in between 1 and 2, then this technique is called as *over-relaxation*. It is also possible to select the ω smaller than 1, this time the technique is known as *under-relaxation*.

Inserting Eq. 4.60 into 4.61 results in

$$\phi_{i, k}^{n+1} = \phi_{i, k}^n + \omega \left[\frac{c_2}{c_1} (\phi_{i+1, k}^n + \phi_{i-1, k}^n) + \frac{c_3}{c_1} (\phi_{i, k+1}^n + \phi_{i, k-1}^n) - \frac{F^n(i, k)}{c_1} - \phi_{i, k}^n \right] \quad (4.62)$$

which yields

$$\phi_{i, k}^{n+1} = (1 - \omega) \phi_{i, k}^n + \omega \left[\frac{c_2}{c_1} (\phi_{i+1, k}^n + \phi_{i-1, k}^n) + \frac{c_3}{c_1} (\phi_{i, k+1}^n + \phi_{i, k-1}^n) - \frac{F^n(i, k)}{c_1} \right] \quad (4.63)$$

Eq. 4.63 is then used while calculating the electric potentials for the inner nodes.

For the left edge nodes:

$$\phi_{i, k} = \phi_{i+1, k} - \frac{\Delta x_1}{\chi_{11}} F(i, k) \quad (4.64)$$

which makes the residual as:

$$R(i, k) = \phi_{i+1, k} - \frac{\Delta x_1}{\chi_{11}} F(i, k) - \phi_{i, k} \quad (4.65)$$

where the forcing term for a left edge node is given in Eq. (4.35). Inserting Eq. (4.65) into (4.61)

$$\phi_{i, k}^{n+1} = \phi_{i, k}^n + \omega \left(\phi_{i+1, k}^n - \frac{\Delta x_1}{\chi_{11}} F^n(i, k) - \phi_{i, k}^n \right) \quad (4.66)$$

or,

$$\phi_{i, k}^{n+1} = (1 - \omega) \phi_{i, k}^n + \omega \left[\phi_{i+1, k}^n - \frac{\Delta x_1}{\chi_{11}} F^n(i, k) \right] \quad (4.67)$$

which is the equation required to find the electric potentials along the left edge. Similar procedure is followed to find the required set of equations for the nodes where natural boundary conditions were assigned.

Along the right edge:

$$\phi_{i, k}^{n+1} = (1 - \omega) \phi_{i, k}^n + \omega \left[\phi_{i-1, k}^{n+1} + \frac{\Delta x_1}{\chi_{11}} F^n(i, k) \right] \quad (4.68)$$

where $F^n(i, k)$ is given in Eq. (4.41) for a right edge node.

Along the bottom edge:

$$\phi_{i, k}^{n+1} = (1 - \omega) \phi_{i, k}^n + \omega \left[\phi_{i, k+1}^n - \frac{\Delta x_3}{\chi_{33}} F^n(i, k) \right] \quad (4.69)$$

where $F^n(i, k)$ is given in Eq. (4.49) for a bottom edge node.

Along the top edge:

$$\phi_{i, k}^{n+1} = (1 - \omega) \phi_{i, k}^n + \omega \left[\phi_{i, k-1}^{n+1} + \frac{\Delta x_3}{\chi_{33}} F^n(i, k) \right] \quad (4.70)$$

where $F^n(i, k)$ is given in Eq. (4.55) for a top edge node.

For corner nodes, a simple averaging is used for finding the electric potentials. For a bottom left corner node;

$$\phi_{i, k}^{n+1} = (1 - \omega) \phi_{i, k}^n + \omega \left[\frac{\chi_{11} \phi_{i+1, k}^n + \chi_{33} \phi_{i, k+1}^n}{\chi_{11} + \chi_{33}} \right]. \quad (4.71)$$

For a bottom right corner node;

$$\phi_{i,k}^{n+1} = (1 - \omega)\phi_{i,k}^n + \omega \left[\frac{\chi_{11}\phi_{i-1,k}^{n+1} + \chi_{33}\phi_{i,k+1}^n}{\chi_{11} + \chi_{33}} \right]. \quad (4.72)$$

For a top left corner node;

$$\phi_{i,k}^{n+1} = (1 - \omega)\phi_{i,k}^n + \omega \left[\frac{\chi_{11}\phi_{i+1,k}^n + \chi_{33}\phi_{i,k-1}^{n+1}}{\chi_{11} + \chi_{33}} \right]. \quad (4.73)$$

For a top right corner node;

$$\phi_{i,k}^{n+1} = (1 - \omega)\phi_{i,k}^n + \omega \left[\frac{\chi_{11}\phi_{i-1,k}^{n+1} + \chi_{33}\phi_{i,k-1}^{n+1}}{\chi_{11} + \chi_{33}} \right]. \quad (4.74)$$

A detailed description of the potential field calculation is provided in Algorithm 5.

Algorithm 5 Calculation of the Electric Potential Field

```
1: procedure ITERATIVE CALCULATION FOR ELECTRIC POTENTIAL FIELD USING FINITE
   DIFFERENCE ALGORITHM
2:   Gather the displacement fields:  $u_1$  and  $u_3$ 
3:   Calculate forcing terms at each non-damaged node  $(i,k)$ :  $F(i,k)$  using Eqs. (4.26), (4.49),
   (4.55), (4.35), and Eq. (4.41).
4:   Apply electric essential boundaries.
5:   Define a relative error tolerance:  $\text{eps} = 1 \times 10^{-6}$ 
6:   Define an iteration error:  $\text{error} = 2 \times \text{eps}$ 
7:   while  $\text{error} \geq \text{eps}$  do
8:     Calculate the potential field  $\phi^{n+1}$  for the nodes  $(i,k)$  without a prescribed electric es-
   sential boundary condition.
9:     for node  $i \leftarrow 1$  to  $N_1$  do
10:      for node  $k \leftarrow 1$  to  $N_3$  do
11:        if node  $(i,k)$  is an inner node then
12:          Calculate  $\phi^{n+1}$  using Eq. (4.63).
13:        else if node  $(i,k)$  is a bottom edge node then
14:          Calculate  $\phi^{n+1}$  using Eq. (4.69).
15:        else if node  $(i,k)$  is a top edge node then
16:          Calculate  $\phi^{n+1}$  using Eq. (4.70).
17:        else if node  $(i,k)$  is a left edge node then
18:          Calculate  $\phi^{n+1}$  using Eq. (4.67).
19:        else if node  $(i,k)$  is a right edge node then
20:          Calculate  $\phi^{n+1}$  using Eq. (4.68).
21:        else if node  $(i,k)$  is a bottom left corner node then
22:          Calculate  $\phi^{n+1}$  using Eq. (4.71).
23:        else if node  $(i,k)$  is a bottom right corner node then
24:          Calculate  $\phi^{n+1}$  using Eq. (4.72).
25:        else if node  $(i,k)$  is a top left corner node then
26:          Calculate  $\phi^{n+1}$  using Eq. (4.73).
27:        else if node  $(i,k)$  is a top right corner node then
28:          Calculate  $\phi^{n+1}$  using Eq. (4.74).
29:        end if
30:      end for
31:    end for
32:    Calculate the L2-norm of the potential field
33:     $\text{error} = \sqrt{\frac{\sum |\phi^{n+1} - \phi^n|^2}{\sum |\phi^n|^2}}$ 
34:    Update potential field
35:     $\phi_{i,k}^n = \phi_{i,k}^{n+1}$ 
36:  end while
37: end procedure
```

4.3 Mode-I Fracture Problem

This section presents the mode-I fracture problem simulation of a pre-notched PZT-4 ceramic plate shown in Fig. 4.4. The applied displacement loading illustrated in Fig. 4.4 is increased from zero to 2×10^{-10} m at each time step in the adaptive dynamic relaxation solver. The final value of the applied displacement is set to 5×10^{-6} m. The material is poled along the positive vertical axis, and its properties are provided in Table 4.1.

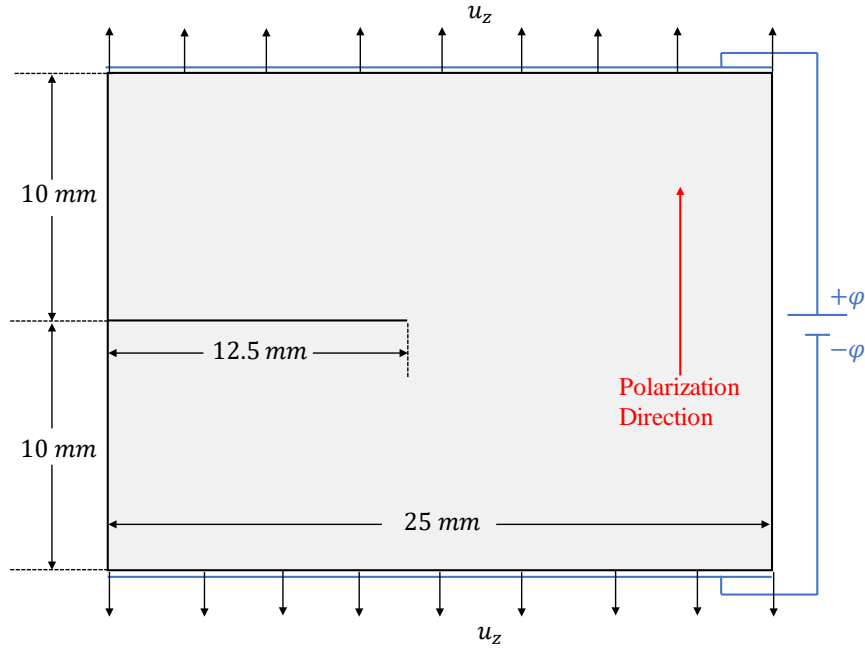


Figure 4.4: Problem setup: A pre-notched PZT-4 plate under tension and applied electric field.

Table 4.1: Material Properties of PZT-4 [13]

Elastic Constants [N/m ²]		Piezoelectric Coefficients [N/(V·m)]		Dielectric Permittivity [N/V ²]	
C_{11}^E	13.9×10^{10}	e_{31}	-6.98	χ_{11}^e	6.00×10^{-9}
C_{13}^E	7.43×10^{10}	e_{33}	13.84	χ_{33}^e	5.47×10^{-9}
C_{33}^E	11.3×10^{10}	e_{15}	13.44		
C_{55}^E	2.56×10^{10}				

The electric potentials are assigned to the top and bottom surfaces of the plate, creating an applied electric field parallel to the poling axis of the material. These potentials are applied in a ramp fashion and reach their maximum values when the applied displacement reaches to 5×10^{-7} m. The crack surface is assumed to be impermeable, and the medium within the crack is not

considered.

Sun and Park [120] reports the elastic modulus of the PZT-4 in the isotropic plane is 82 GPa, and static tensile strength of the material is 75.8 MPa. The critical bond stretch is obtained by the ultimate tensile strain of the material, which is taken as 9.24×10^{-4} . When the bond between material points is broken, it loses the electrical conductivity. In addition, it is not used any other failure criterion that governs the electrical failure. Hence, the failure process is assumed as a fully mechanical phenomenon. The relaxation parameter (see Eq. (4.61)) used in the SOR algorithm is selected as 1.2. Two different horizon values and the mesh densities are considered here. The uniform grid mesh, h , becomes 0.25 mm in the coarse mesh and 0.125 mm for the fine mesh densities, respectively.

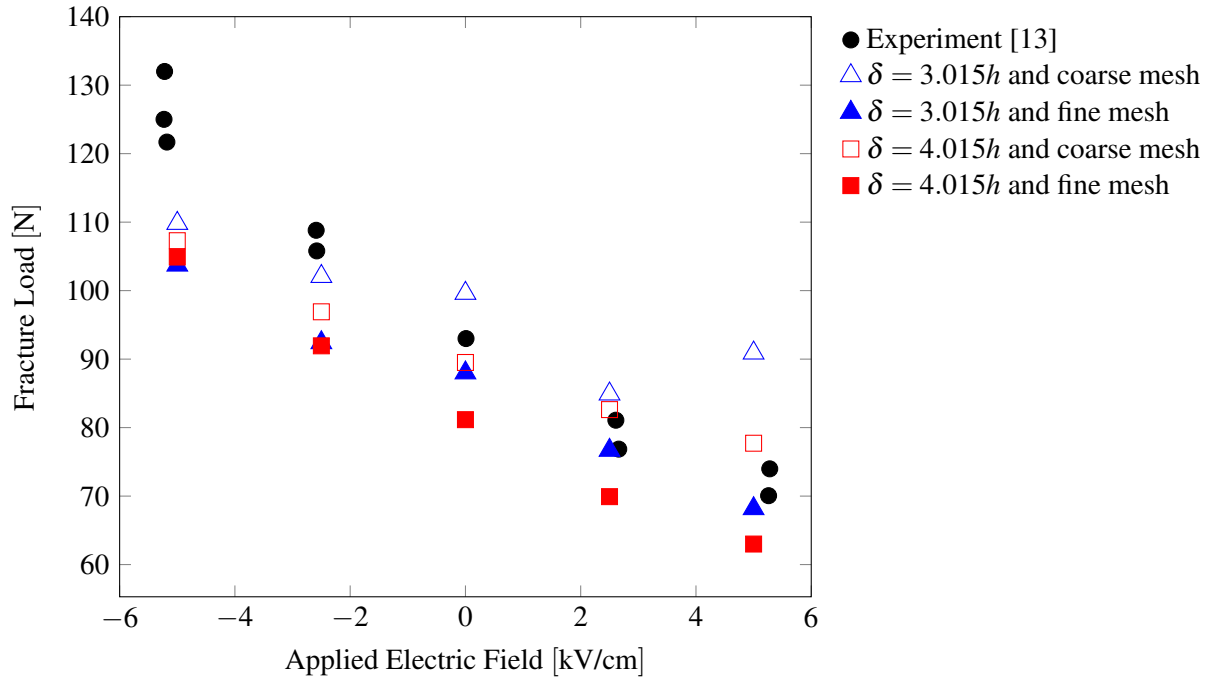


Figure 4.5: Comparison of the fracture load versus applied electric field with the PD results and the experimental data [13].

Fig. 4.5 compares the fracture loads versus the applied electric fields from the PD analysis and the experimental data [13]. The fracture loads are taken as the maximum value of the polynomial equation best fitted to the reaction force versus applied displacement curves given in Figs. 4.6 and 4.7. On the other hand, the reaction forces are calculated by summing the internal forces in the vertical direction at the top layer of the nodes where the displacements are imposed. The

PD simulation captures the key experimental finding, which is the dependence of the fracture load on the applied electric field for the poled piezoelectric ceramics. When the applied electric field is parallel to the polarization direction, the positive electric field creates tension in the vertical direction and aids the crack opening. As a result, the fracture load reduces depending on the magnitude of the electric field. On the other hand, the negative electric fields create compression and impede the crack opening. Hence, we obtain higher fracture load values than those with a positive applied electric field.

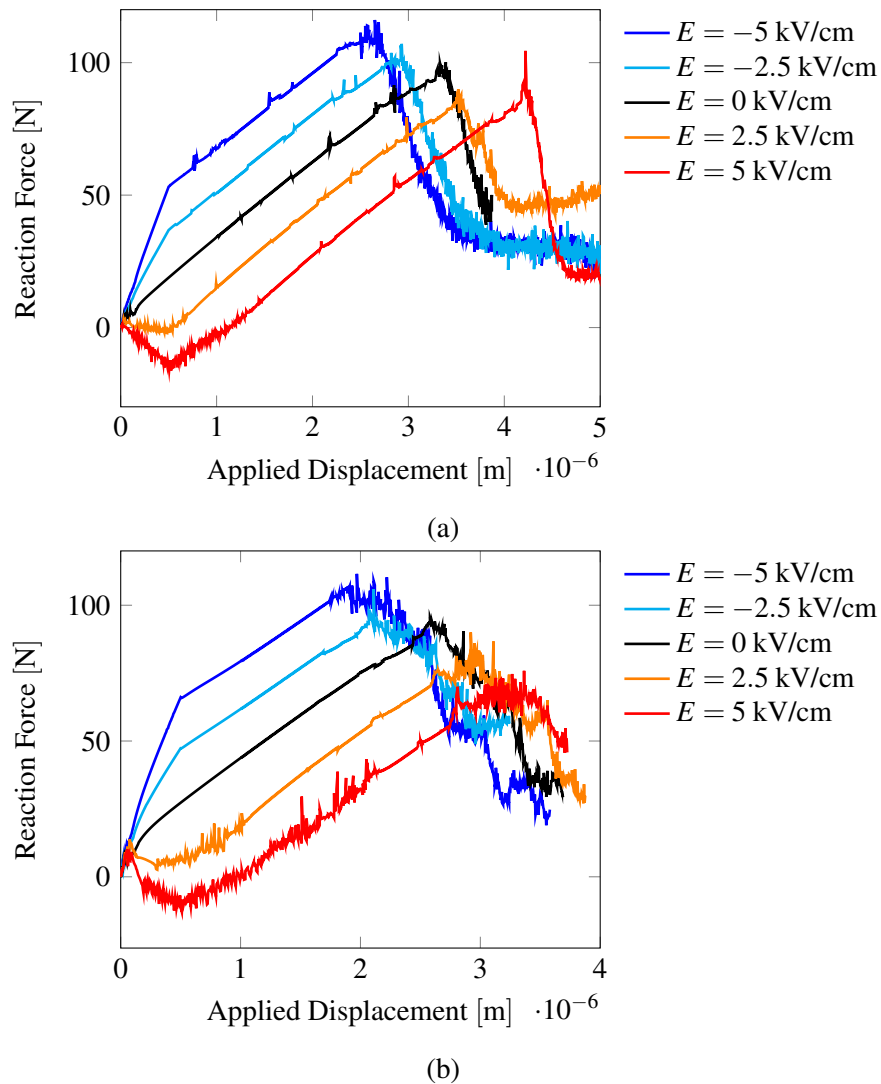


Figure 4.6: Reaction force versus applied displacement results for (a) coarse, and (b) fine meshes with $\delta = 3.015h$.

Figs. 4.6 and 4.7 present the structural response of the pre-notched PZT-4 plate under

uniaxial tension. Strong oscillations are observed for several reasons that can cause that. One reason can be the selected tolerance value, 0.1%, may not be small enough, primarily when the electric fields work in favor of crack opening. In addition, it is observed that tensile stresses along the crack surfaces are not vanishing as the crack propagates. We tried to degrade the material properties when the local damage exceeds a specific value to prevent this behavior. Unfortunately, the degradation of the material properties did not work well at the initial tip of the pre-notch, although the stresses along the crack surface are improved. Therefore, we address a solution for this problem as a future study.

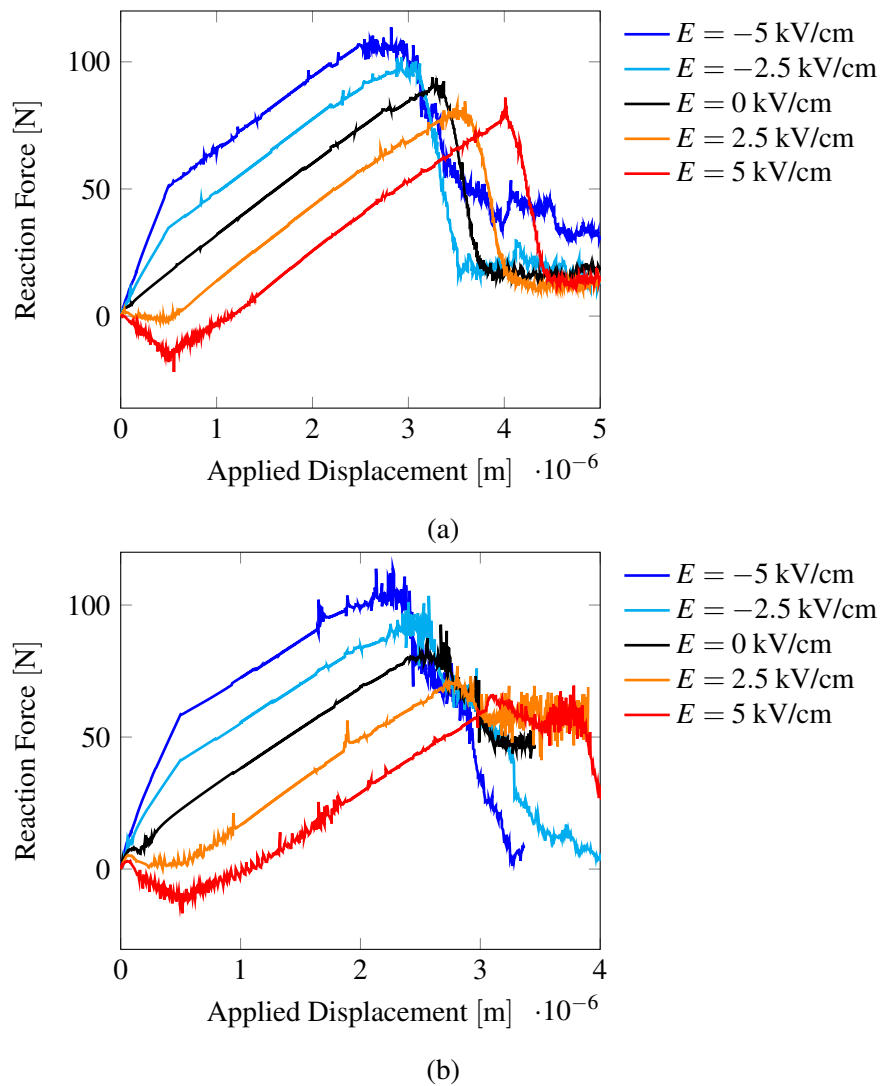


Figure 4.7: Reaction force versus applied displacement results for (a) coarse, and (b) fine meshes with $\delta = 4.015h$.

Figs. 4.9 to 4.16 provide the distribution of the local damage, vertical displacement, and potential field for different crack lengths and applied electric fields. In these plots, the PD simulations with fine mesh and $3.015h$ horizon size are used. Although the mode-I failure is successfully achieved, the electric potential fields deviates from the expectation as the crack extend its length.

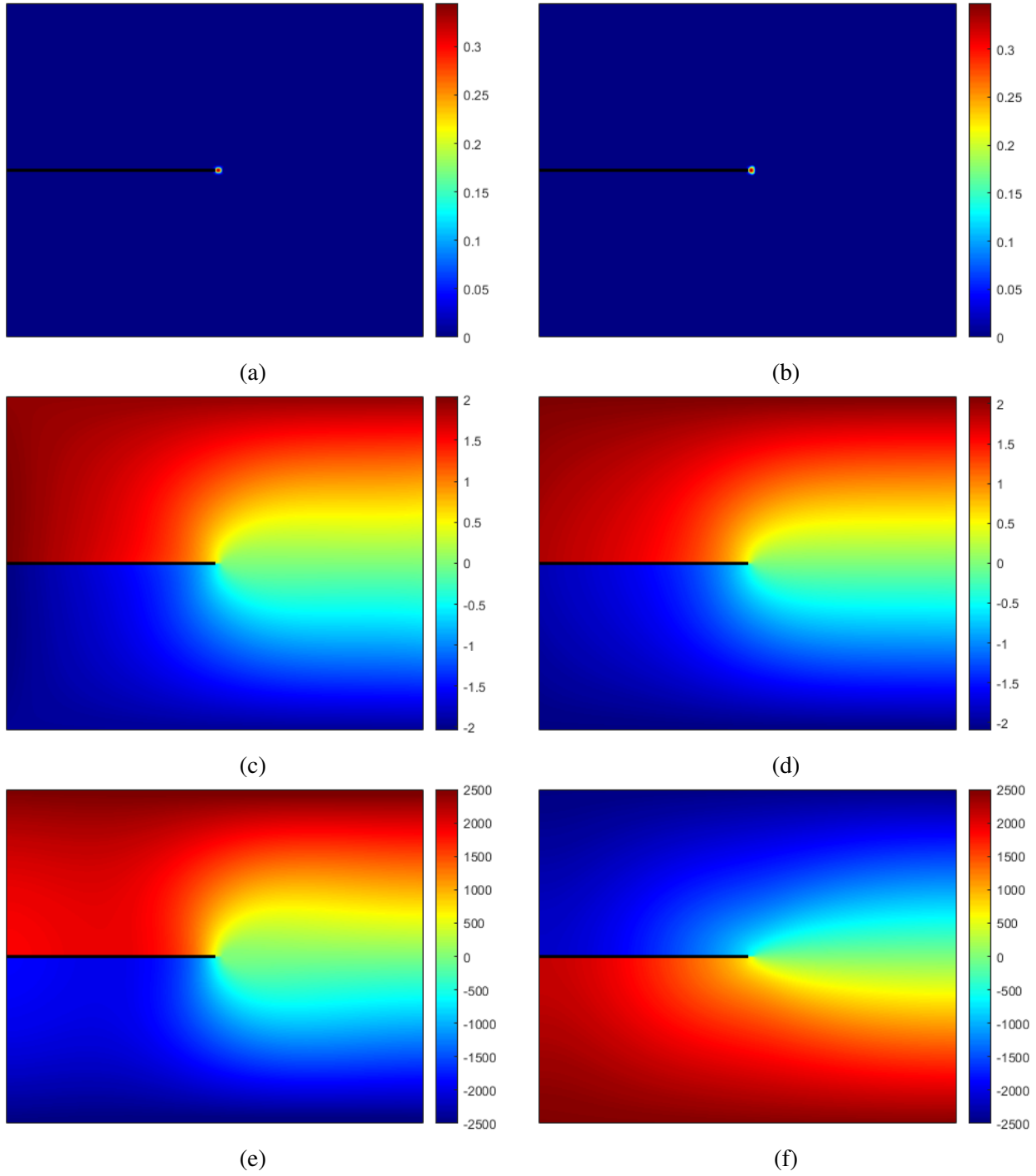


Figure 4.8: (a-b) Damage, (c-d) w [μm], and (e-f) ϕ [V] distributions at the crack opening for an applied electric field of -2.5 kV/m at the left and $+2.5$ kV/m at the right.

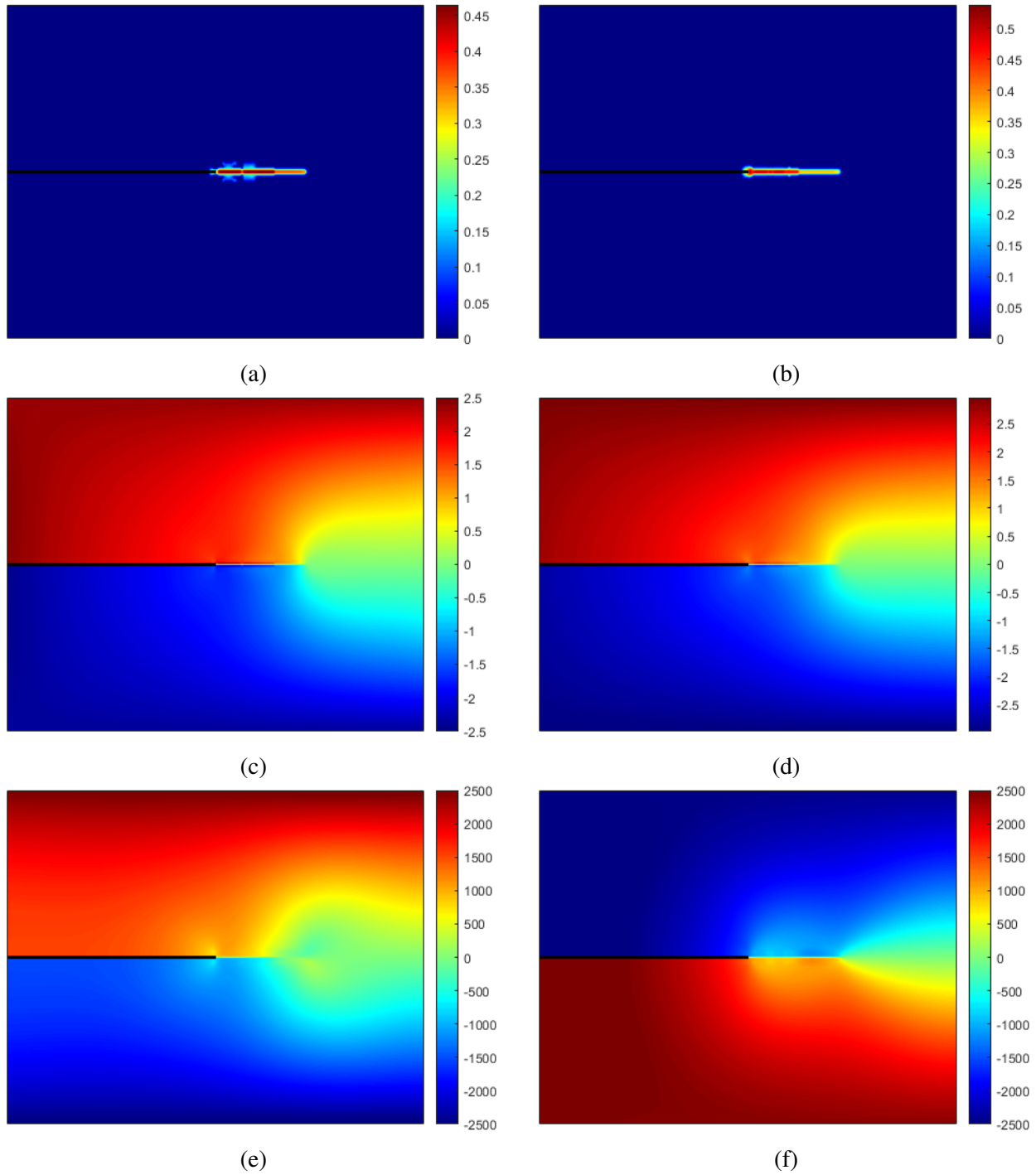


Figure 4.9: (a-b) Damage, (c-d) w [μm], and (e-f) ϕ [V] distributions when the crack reaches approximately 18 mm for an applied electric field of -2.5 kV/m at the left and $+2.5$ kV/m at the right.

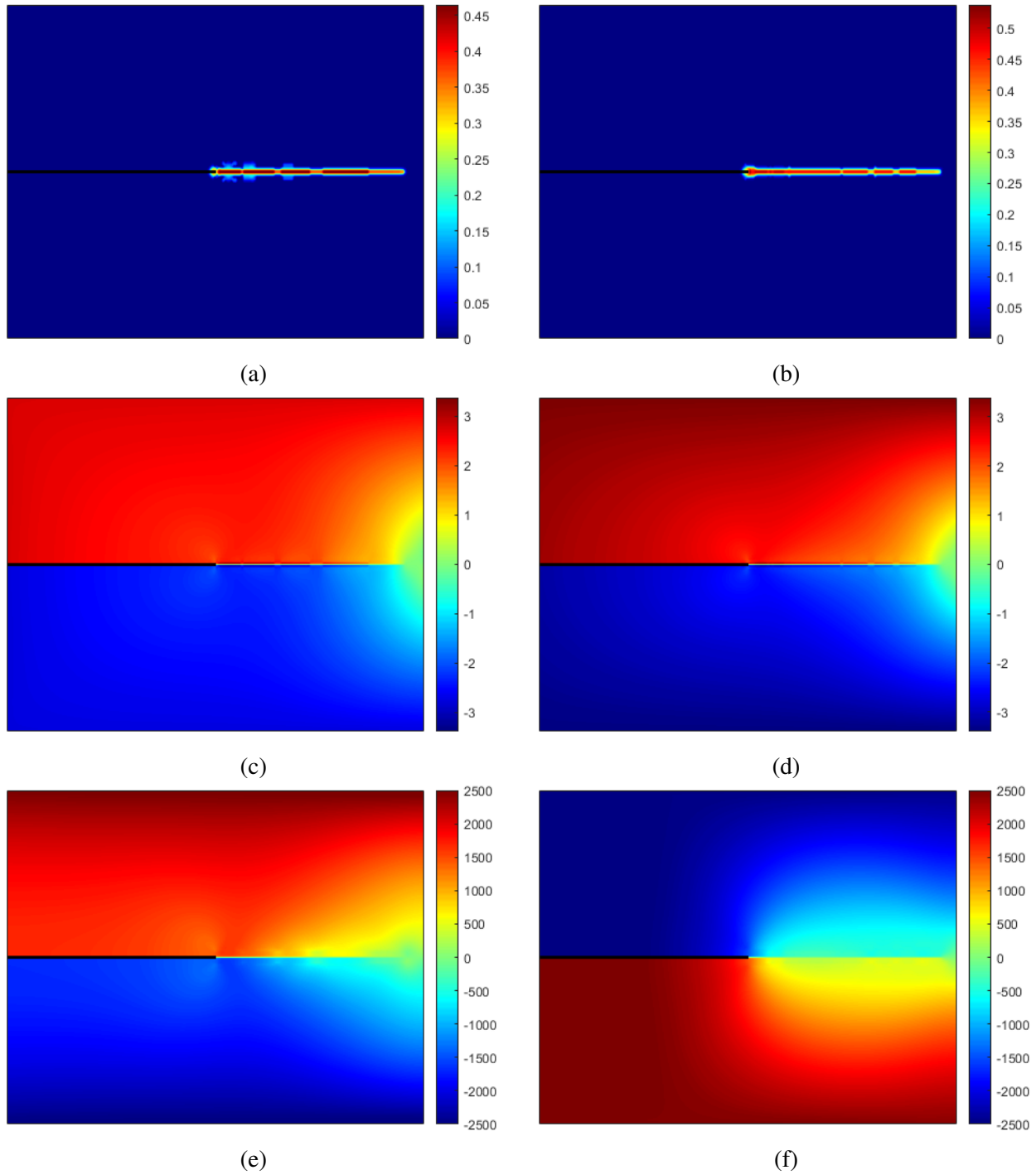


Figure 4.10: (a-b) Damage, (c-d) w [μm], and (e-f) ϕ [V] distributions when the crack reaches approximately 24 mm for an applied electric field of -2.5 kV/m at the left and $+2.5$ kV/m at the right.

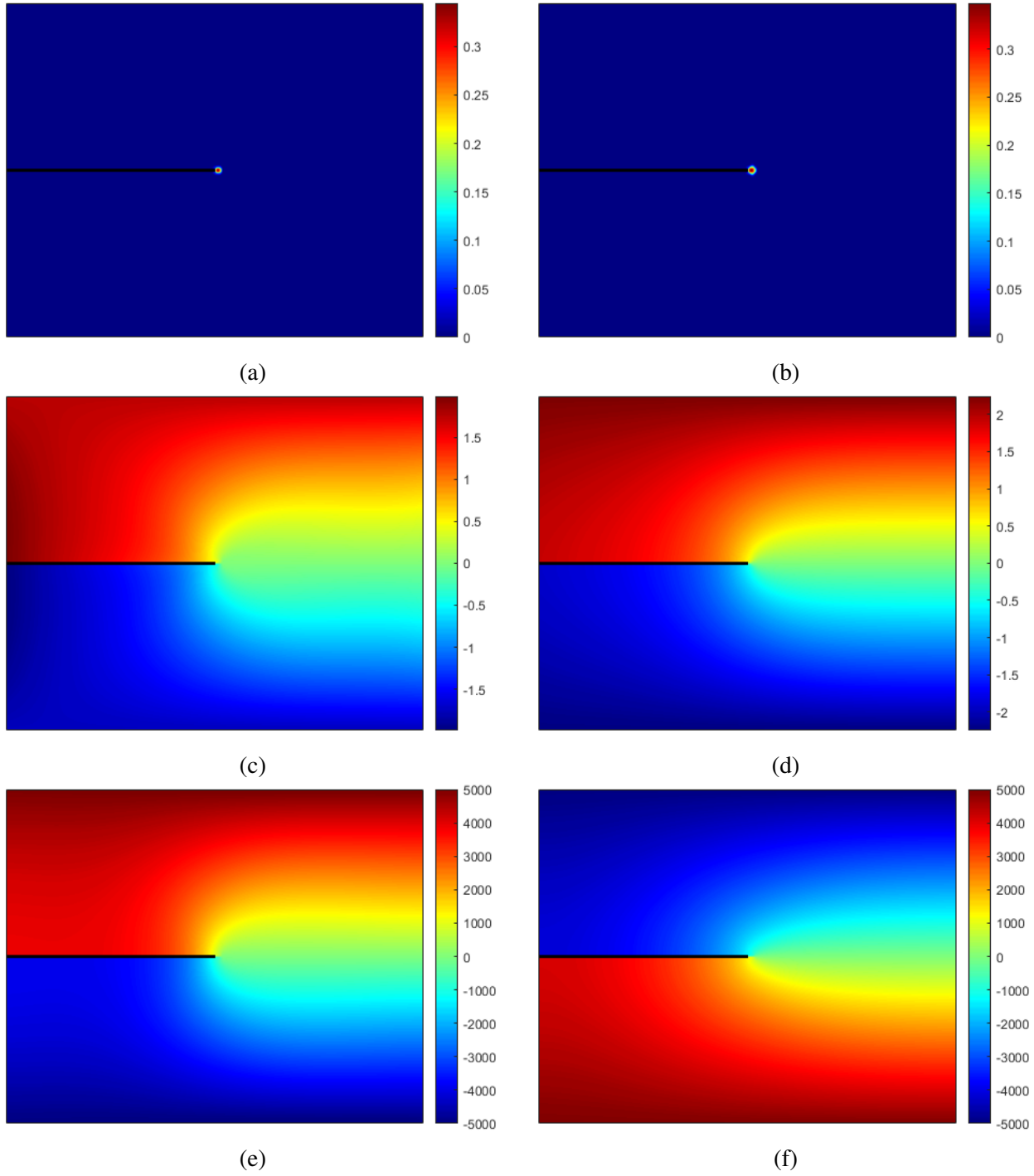


Figure 4.11: (a-b) Damage, (c-d) w [μm], and (e-f) ϕ [V] distributions at the crack opening for an applied electric field of -5 kV/m at the left and $+5$ kV/m at the right.

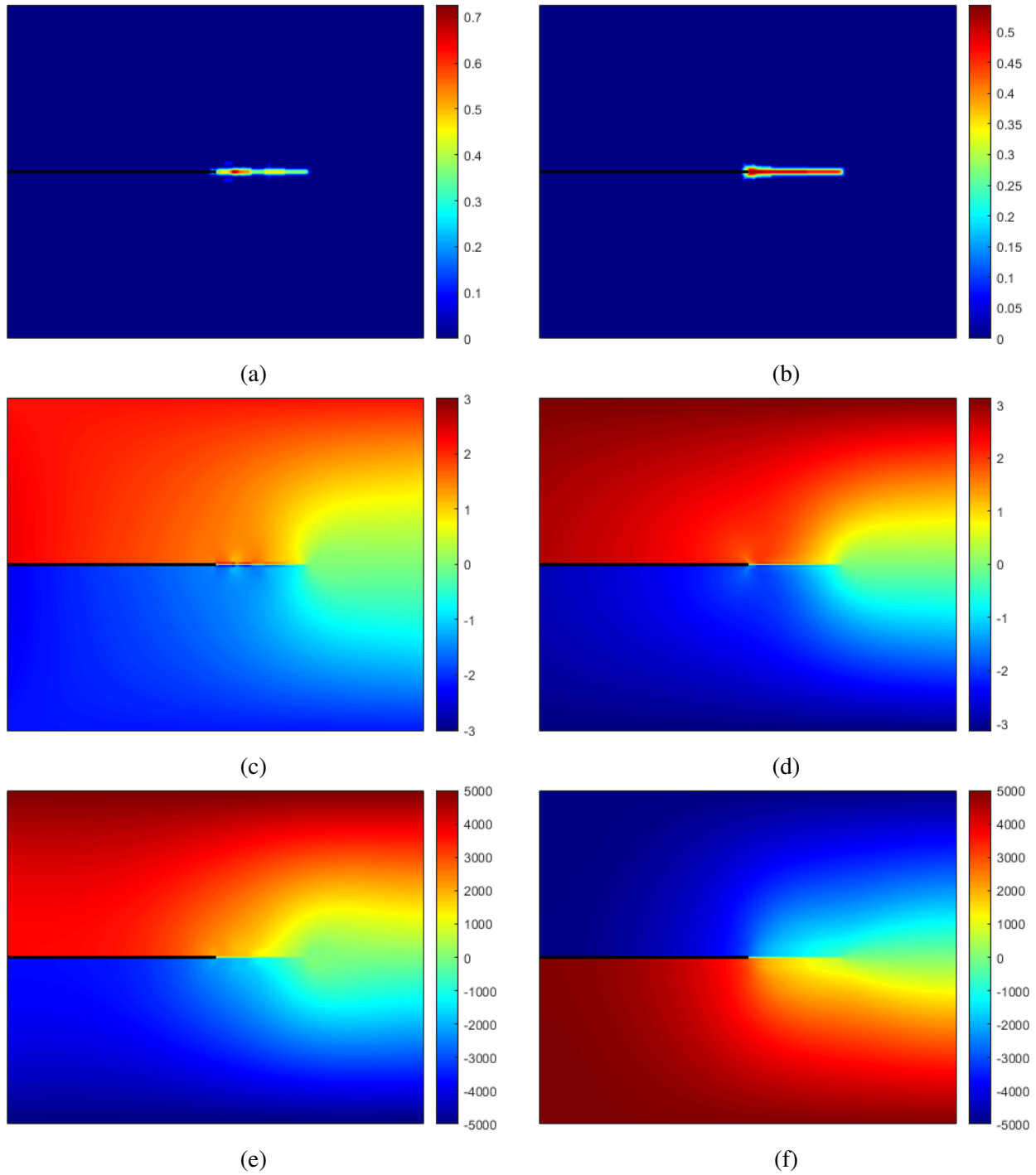


Figure 4.12: (a-b) Damage, (c-d) w [μm], and (e-f) ϕ [V] distributions when the crack reaches approximately 18 mm for an applied electric field of -5 kV/m at the left and +5 kV/m at the right.

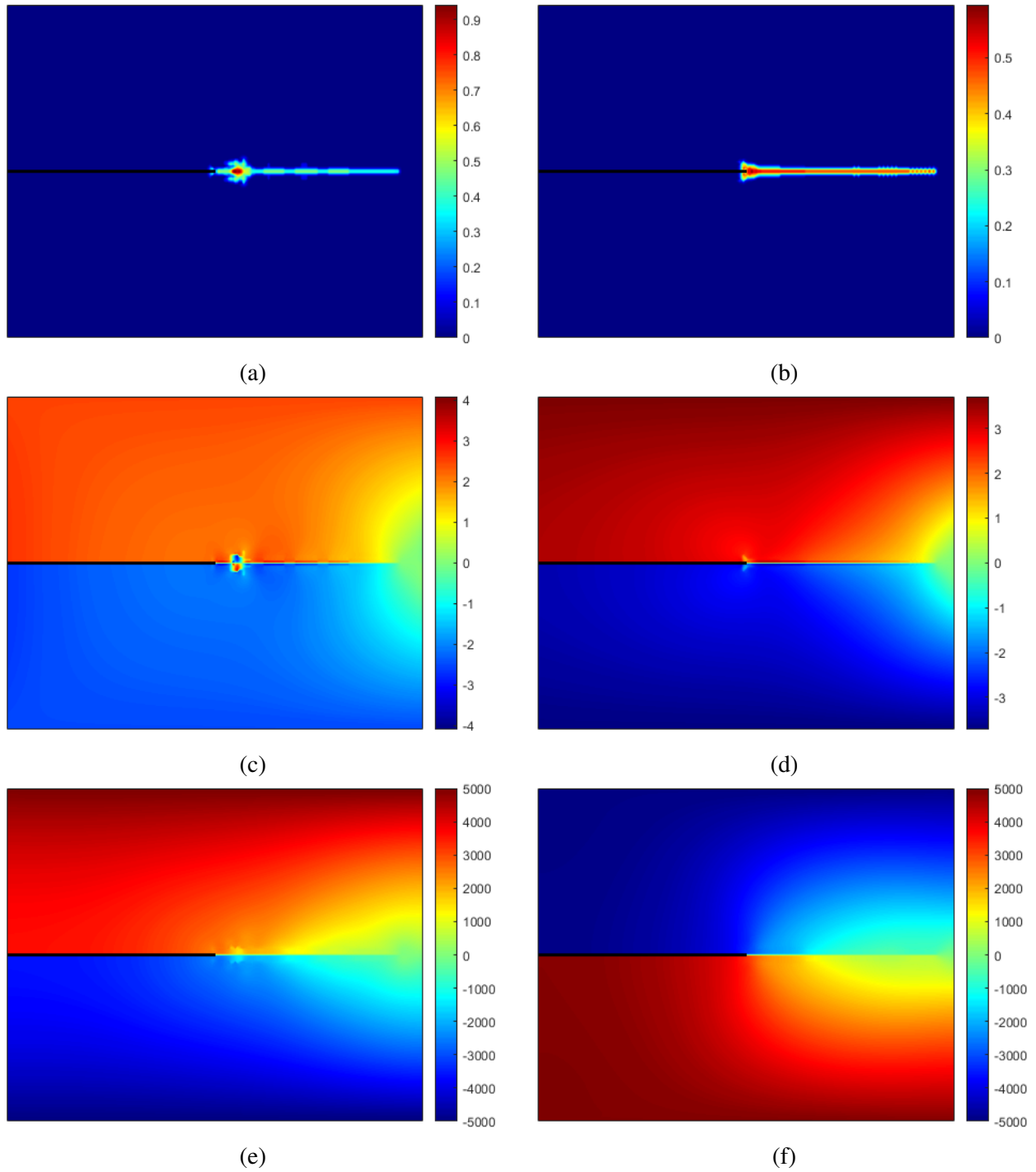


Figure 4.13: (a-b) Damage, (c-d) w [μm], and (e-f) ϕ [V] distributions when the crack reaches approximately 24 mm for an applied electric field of -5 kV/m at the left and +5 kV/m at the right.

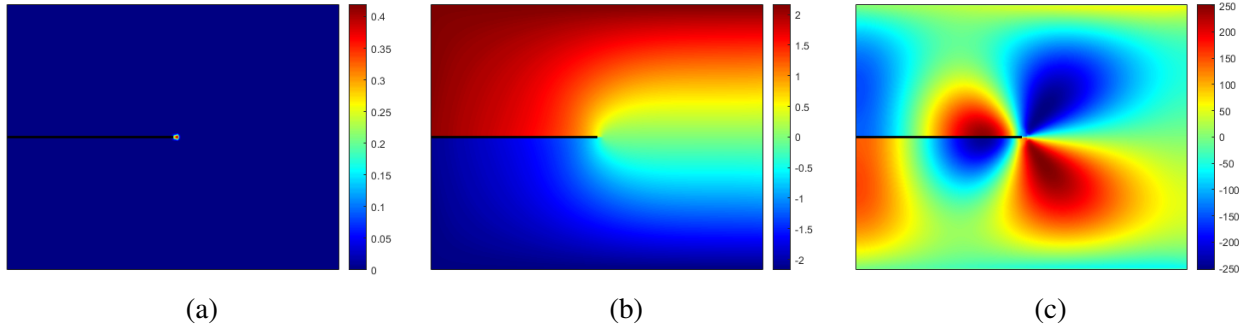


Figure 4.14: (a) Damage, (b) w [μm], and (c) ϕ [V] distributions at the crack opening without an applied electric field.

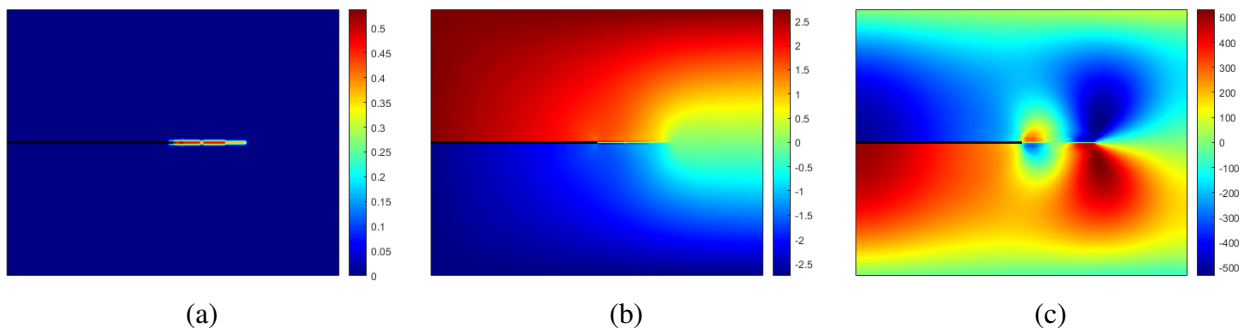


Figure 4.15: (a) Damage, (b) w [μm], and (c) ϕ [V] distributions when the crack reaches approximately 18 mm without an applied electric field.

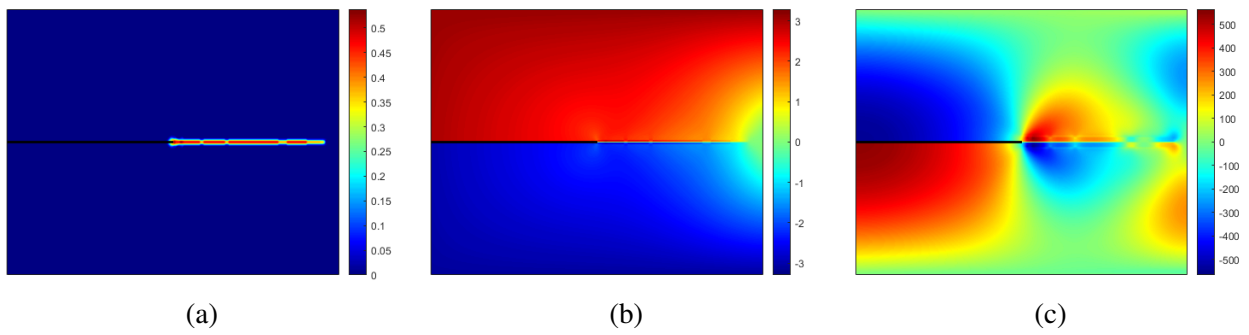


Figure 4.16: (a) Damage, (b) w [μm], and (c) ϕ [V] distributions when the crack reaches approximately 24 mm without an applied electric field.

4.4 Chapter Summary

This chapter presents the NOSB-PD modeling to analyze the mode-I fracture of a pre-notched PZT-4 plate. An iterative solution algorithm is utilized to couple the electrical and mechanical variables. While the electric-potential field is calculated by the finite-difference algorithm, the mechanical displacements are obtained by the explicit ADR technique at each iteration.

The numerical simulations show that the effect of the applied electric field on the fracture load is captured successfully. Namely, an applied negative electric field works against the crack opening and increases the fracture load for a poled PZT-4 perpendicular to the crack surfaces. On the other hand, a positive electric field works in favor of crack opening, resulting in a decrease in the fracture load. Moreover, the expected crack opening for the mode-I fracture is achieved for all cases where the electric field is applied in different magnitudes and directions.

CHAPTER 5

CONCLUSIONS AND FUTURE WORKS

One of the main objectives of this work is to enhance the convergence and accuracy of the linear elastic bond-based PD model. For this purpose, a surface correction method for bond-based peridynamics is presented, including the discretely calculated peridynamic material parameters. During the numerical simulation, the discretely calculated peridynamic material parameters can easily account for the effect of newly formed free surfaces, i.e., crack surfaces. The results obtained by utilizing the proposed surface correction method are compared with the surface correction methods available in the literature. It is shown that the proposed surface correction method is more accurate in the static with uniform deformation and dynamic crack propagation problems by considering the missing neighbors along the problem boundaries and the newly emerging boundaries.

The second main objective is to develop a framework of an implicit formulation of non-ordinary state-based peridynamic for linear piezoelectricity. Thus, a perturbation technique is employed to construct the tangent stiffness matrix of the electromechanical system of equations. Then, various problems with different loading and boundary conditions are solved. Finally, these solutions are compared with those from the literature, either analytical or FEM. These comparisons reveal that the proposed fully-coupled PD formulation can capture the structural response of the transversely isotropic piezoelectric materials.

The third and last objective of this study is to explore the fracture analysis of the piezoelectric ceramics within the peridynamic framework. An iterative solution procedure is followed to couple the electric potentials and mechanical displacement within a specified tolerance. Mode-I fracture simulation of a pre-notched PZT-4 plate subjected to various electric fields is performed to show the capability of the proposed NOSB-PD formulation for linear piezoelectricity. The expected crack pattern is successfully obtained. Moreover, the fracture loads obtained from the nu-

merical simulations agree with the experimental results. In addition, our results exhibit the effect of the applied electric field on the fracture load. Similar to the experimental findings, the positive electric field helps the crack opening and decreases the fracture load. On the other hand, the negative electric field is working against the crack opening, increasing the fracture load. However, we observe that the stress-free boundary condition is not held as the crack extends its length, creating strong oscillations once the loads exceed the fracture loads.

In conclusion, peridynamics is a powerful method to study fracture analysis of brittle materials and can also be extended to cover the multiphysics analyses. This thesis presents the peridynamic simulations of the fully-coupled electromechanical mode-I crack opening within transversely isotropic piezoelectric ceramics. Nevertheless, still, much more research is needed to expand this study.

5.1 Future Works

The following future studies can be listed to be done as an extension of this work to demonstrate the linear piezoelectricity capability of the proposed NOSB-PD:

- Establishing the stress-free boundary conditions along the crack faces,
- Investigating the performance of the different damage criteria, and
- Performing the mixed-mode fracture simulations.

REFERENCES

- [1] Ted L Anderson. *Fracture mechanics: fundamentals and applications*. CRC press, 2017.
- [2] S. A. Silling. Reformulation of elasticity theory for discontinuities and long-range forces. *Journal of the Mechanics and Physics of Solids*, 48:175–209, 2000.
- [3] S. A. Silling and F. Bobaru. Peridynamic modeling of membranes and fibers. *International Journal of Non-Linear Mechanics*, 40:395–409, 2005.
- [4] M. L. Parks, R. B. Lehoucq, S. J. Plimpton, and S. A. Silling. Implementing peridynamics within a molecular dynamics code. *Computer Physics Communications*, 179:777–783, 2008.
- [5] B. Alali and R. Lipton. Multiscale dynamics of heterogeneous media in the peridynamic formulation. *Journal of Elasticity*, 106:71–103, 2012.
- [6] P. D. Seleson. *Peridynamic Multiscale Models for the Mechanics of Materials : Constitutive Relations , Upscaling from Atomistic Systems , and Interface Problems*. PhD thesis, Florida State University, 2010.
- [7] J. Zhao, Z. Chen, J. Mehrmashhadi, and F. Bobaru. A stochastic multiscale peridynamic model for corrosion-induced fracture in reinforced concrete. *Engineering Fracture Mechanics*, 229:106969, 2020.
- [8] S. A. Silling, M. Epton, O. Weckner, J. Xu, and E. Askari. Peridynamic states and constitutive modeling. *Journal of Elasticity*, 88:151–184, 2007.
- [9] Yao Fu, Erol C. Harvey, and Muradlidhar K. Ghantasala. Piezoelectric polymer PVDF microactuators. In *Smart Materials*, pages 31–1–31–7. CRC press, 2009.

- [10] Fuqian Yang. Fracture mechanics for a Mode I crack in piezoelectric materials. *International Journal of Solids and Structures*, 38(21):3813–3830, 2001.
- [11] A.L. Kholkin, D.A. Kiselev, L.A. Kholkina, and A. Safari. Piezoelectric and electrostatic ceramics transducers and actuators. In *Smart Materials*, pages 9–1–9–27. CRC press, 2009.
- [12] Tong-Yi Zhang and C.F. Gao. Fracture behaviors of piezoelectric materials. *Theoretical and applied fracture mechanics*, 41(1-3):339–379, 2004.
- [13] Seungbae Park and Chin-Teh Sun. Fracture criteria for piezoelectric ceramics. *Journal of the american ceramic society*, 78(6):1475–1480, 1995.
- [14] Xinhua Yang, Chuanyao Chen, Yuantai Hu, and Cheng Wang. Damage analysis and fracture criteria for piezoelectric ceramics. *International Journal of Non-Linear Mechanics*, 40(9):1204–1213, 2005.
- [15] E. Emmrich and O. Weckner. The peridynamic equation and its spatial discretisation. *Mathematical Modelling and Analysis*, 12:17–27, 2007.
- [16] X. Chen and M. Gunzburger. Continuous and discontinuous finite element methods for a peridynamics model of mechanics. *Computer Methods in Applied Mechanics and Engineering*, 200:1237–1250, 2011.
- [17] T. Bode, C. Weißenfels, and P. Wriggers. Peridynamic Petrov-Galerkin method: a generalization of the peridynamic theory of correspondence materials. *Computer Methods in Applied Mechanics and Engineering*, 358:112636, 2020.
- [18] P. Seleson and D. J. Littlewood. Convergence studies in meshfree peridynamic simulations. *Computers and Mathematics with Applications*, 71:2432–2448, 2016.
- [19] S. A. Silling and E. Askari. A meshfree method based on the peridynamic model of solid mechanics. *Computers and Structures*, 83:1526–1535, 2005.
- [20] M. L. Parks, P. Seleson, S. J. Plimpton, R. B. Lehoucq, and S. A. Silling. Peridynamics with lammps : A user guide. Technical report, Sandia National Laboratory, Albuquerque, New Mexico, 2008.

- [21] W. Hu, Y. D. Ha, and F. Bobaru. Numerical integration in peridynamics. Technical report, University of Nebraska-Lincoln, 2010.
- [22] K. Yu, X. J. Xin, and K. B. Lease. A new adaptive integration method for the peridynamic theory. *Modelling and Simulation in Materials Science and Engineering*, 19:045003, 2011.
- [23] P. Seleson. Improved one-point quadrature algorithms for two-dimensional peridynamic models based on analytical calculations. *Computer Methods in Applied Mechanics and Engineering*, 282:184–217, 2014.
- [24] W. H. Gerstle, N. Sau, and S. A. Silling. Peridynamic modeling of concrete structures. *Nuclear engineering and design*, 237:1250–1258, 2007.
- [25] W. H. Gerstle. *Introduction to practical peridynamics: computational solid mechanics without stress and strain*. World Scientific Publishing Company, 2015.
- [26] V. Diana and S. Casolo. A bond-based micropolar peridynamic model with shear deformability: Elasticity, failure properties and initial yield domains. *International Journal of Solids and Structures*, 160:201–231, 2019.
- [27] Q.-Z. Zhu and T. Ni. Peridynamic formulations enriched with bond rotation effects. *International journal of engineering science*, 121:118–129, 2017.
- [28] W.-J. Li, Q.-Z. Zhu, and T. Ni. A local strain-based implementation strategy for the extended peridynamic model with bond rotation. *Computer Methods in Applied Mechanics and Engineering*, 358:112625, 2020.
- [29] E. Madenci, A. Barut, and N. Phan. Bond-based peridynamics with stretch and rotation kinematics for opening and shearing modes of fracture. *Journal of Peridynamics and Non-local Modeling*, 3:211–254, 2021.
- [30] E. Madenci and E. Oterkus. *Peridynamic theory and its applications*. New York: Springer, 2014.
- [31] S. Oterkus, E. Madenci, and A.I Agwai. Peridynamic thermal diffusion. *Journal of Computational Physics*, 265:71–96, 2014.

- [32] S. Oterkus. *Peridynamics for the solution of multiphysics problems*. PhD thesis, The University of Arizona, 2015.
- [33] E. Oterkus. *Peridynamic theory for modeling three-dimensional damage growth in metallic and composite structures*. PhD thesis, The University of Arizona, 2010.
- [34] R. W. Macek and S. A. Silling. Peridynamics via finite element analysis. *Finite Elements in Analysis and Design*, 43:1169–1178, 2007.
- [35] E. Madenci and E. Oterkus. Coupling of the peridynamic theory and finite element method. In *Peridynamic Theory and Its Applications*, pages 191–202. Springer, 2014.
- [36] J. Mitchell, S. A. Silling, and D. Littlewood. A position-aware linear solid constitutive model for peridynamics. *Journal of Mechanics of Materials and Structures*, 10:539–557, 2015.
- [37] S. A. Silling. Introduction to peridynamics. In *Handbook of peridynamic modeling*, pages 63–98. Chapman and Hall/CRC, 2016.
- [38] Q. V. Le and F. Bobaru. Surface corrections for peridynamic models in elasticity and fracture. *Computational Mechanics*, 61:499–518, 2018.
- [39] G. C. Ganzenmüller, S. Hiermaier, and M. May. Improvements to the prototype micro-brittle model of peridynamics. In *Meshfree methods for partial differential equations VII*, pages 163–183. Springer, 2015.
- [40] P. Diehl, F. Franzelin, D. Pflüger, and G. C. Ganzenmüller. Bond-based peridynamics: a quantitative study of Mode I crack opening. *International Journal of Fracture*, 201:157–170, 2016.
- [41] Woldemar Voigt. *Lehrbuch der kristallphysik:(mit ausschluss der kristallographik)*, volume 34. BG Teubner, 1910.
- [42] Shaul Katzir. Who knew piezoelectricity? Rutherford and Langevin on submarine detection and the invention of sonar. *Notes and Records of the Royal Society*, 66(2):141–157, 2012.

- [43] Gerold A. Schneider. Influence of electric field and mechanical stresses on the fracture of ferroelectrics. *Annu. Rev. Mater. Res.*, 37:491–538, 2007.
- [44] T. Yamamoto, H. Igarashi, and K. Okazaki. Internal stress anisotropies induced by electric field in lanthanum modified PbTiO₃ ceramics. *Ferroelectrics*, 50(1):273–278, 1983.
- [45] Kiyoshi Okazaki. Mechanical behavior of ferroelectric ceramics. *American Ceramic Society Bulletin*, 63(9):1150–1157, 1984.
- [46] G.G. Pisarenko, V.M. Chushko, and S.P. Kovalev. Anisotropy of fracture toughness of piezoelectric ceramics. *Journal of the American Ceramic Society*, 68(5):259–265, 1985.
- [47] Yi-Heng Chen and Norio Hasebe. Current understanding on fracture behaviors of ferroelectric/piezoelectric materials. *Journal of intelligent material systems and structures*, 16(7-8):673–687, 2005.
- [48] A.G. Tobin and Eugene Pak. Effect of electric fields on fracture behavior of PZT ceramics. In *Smart Structures and Materials 1993: Smart Materials*, volume 1916, pages 78–86. SPIE, 1993.
- [49] Seungbae Park and Chin-Teh Sun. Effect of electric field on fracture of piezoelectric ceramics. *International Journal of Fracture*, 70(3):203–216, 1993.
- [50] Chin-Teh Sun and Seungbae Park. Determination of fracture toughness of piezoceramics under the influence of electric field using Vickers indentation. In *Smart Structures and Materials 1995: Smart Materials*, volume 2441, pages 213–222. SPIE, 1995.
- [51] H. Balke, J. Drescher, and G. Kemmer. Investigation of the mechanical strain energy release rate with respect to a fracture criterion for piezoelectric ceramics. *International journal of fracture*, 89(4):L59–L64, 1998.
- [52] Y. Shindo, M. Oka, and K. Horiguchi. Analysis and testing of indentation fracture behavior of piezoelectric ceramics under an electric field. *J. Eng. Mater. Technol.*, 123(3):293–300, 2001.

- [53] L.Z. Jiang and C.T. Sun. Analysis of indentation cracking in piezoceramics. *International journal of solids and structures*, 38(10-13):1903–1918, 2001.
- [54] Y. Eugene Pak. Crack extension force in a piezoelectric material. *Journal of Applied Mechanics*, 57(3):647–653, 1990.
- [55] Horacio A. Sosa and Y. Eugene Pak. Three-dimensional eigenfunction analysis of a crack in a piezoelectric material. *International Journal of Solids and Structures*, 26(1):1–15, 1990.
- [56] Y.E. Pak. Linear electro-elastic fracture mechanics of piezoelectric materials. *International Journal of Fracture*, 54(1):79–100, 1992.
- [57] G.A. Schneider and V. Heyer. Influence of the electric field on Vickers indentation crack growth in BaTiO_3 . *Journal of the European Ceramic Society*, 19(6-7):1299–1306, 1999.
- [58] G.A. Schneider, F. Felten, and R.M. McMeeking. The electrical potential difference across cracks in PZT measured by Kelvin Probe Microscopy and the implications for fracture. *Acta materialia*, 51(8):2235–2241, 2003.
- [59] M.Y. Chung and T.C.T. Ting. Piezoelectric solid with an elliptic inclusion or hole. *International Journal of Solids and Structures*, 33(23):3343–3361, 1996.
- [60] Susmit Kumar and Raj N. Singh. Crack propagation in piezoelectric materials under combined mechanical and electrical loadings. *Acta materialia*, 44(1):173–200, 1996.
- [61] Susmit Kumar and Raj N. Singh. Effect of the mechanical boundary condition at the crack surfaces on the stress distribution at the crack tip in piezoelectric materials. *Materials Science and Engineering: A*, 252(1):64–77, 1998.
- [62] Y. Shindo, K. Watanabe, and F. Narita. Electroelastic analysis of a piezoelectric ceramic strip with a central crack. *International Journal of Engineering Science*, 38(1):1–19, 2000.
- [63] Yi-Heng Chen and Tian Jian Lu. Cracks and fracture in piezoelectrics. *Advances in applied mechanics*, 39:122–217, 2003.

- [64] Jun Lei and Chuanzeng Zhang. A simplified evaluation of the mechanical energy release rate of kinked cracks in piezoelectric materials using the boundary element method. *Engineering Fracture Mechanics*, 188:36–57, 2018.
- [65] Chandler C. Fulton and Huajian Gao. Electrical nonlinearity in fracture of piezoelectric ceramics. *Applied Mechanics Reviews*, 50:S56–S63, 1997.
- [66] Daining Fang, Zhen-Ke Zhang, Ai Kah Soh, and Kwok Lun Lee. Fracture criteria of piezoelectric ceramics with defects. *Mechanics of Materials*, 36(10):917–928, 2004.
- [67] Amir Abdollahi and Irene Arias. Phase-field modeling of crack propagation in piezoelectric and ferroelectric materials with different electromechanical crack conditions. *Journal of the Mechanics and Physics of Solids*, 60(12):2100–2126, 2012.
- [68] Paolo Gaudenzi and Klaus-Jurgen Bathe. An iterative finite element procedure for the analysis of piezoelectric continua. *Journal of Intelligent Material Systems and Structures*, 6:266–273, 1995.
- [69] R. R. Ohs and N. R. Aluru. Meshless analysis of piezoelectric devices. *Computational Mechanics*, 27:23–36, 2001.
- [70] Christian Miehe, Fabian Welschinger, and Martina Hofacker. A phase field model of electromechanical fracture. *Journal of the Mechanics and Physics of Solids*, 58(10):1716–1740, 2010.
- [71] Shaswat Mohanty, Pramod Yallappa Kumbhar, Narasimhan Swaminathan, and Ratnakumar Annabattula. A phase-field model for crack growth in electro-mechanically coupled functionally graded piezo ceramics. *Smart Materials and Structures*, 29(4):045005, 2020.
- [72] A. Sridhar and M.-A. Keip. A phase-field model for anisotropic brittle fracturing of piezoelectric ceramics. *International Journal of Fracture*, 220(2):221–242, 2019.
- [73] Zachary A. Wilson, Michael J. Borden, and Chad M. Landis. A phase-field model for fracture in piezoelectric ceramics. *International Journal of Fracture*, 183(2):135–153, 2013.

- [74] Christian Linder, D. Rosato, and C. Miehe. New finite elements with embedded strong discontinuities for the modeling of failure in electromechanical coupled solids. *Computer Methods in Applied Mechanics and Engineering*, 200(1-4):141–161, 2011.
- [75] Ł. Jański and M. Kuna. Adaptive finite element modeling of stationary and propagating cracks in piezoelectric structures. *Archives of Mechanics*, 63(5-6):599–619, 2011.
- [76] Ruizhi Wang, Enling Tang, Guolai Yang, Yafei Han, and Chuang Chen. Dynamic fracture behavior of piezoelectric ceramics under impact: Force-electric response and electrical breakdown. *Journal of the European Ceramic Society*, 41(16):139–150, 2021.
- [77] M. Kuna. Finite element analyses of cracks in piezoelectric structures: a survey. *Archive of Applied Mechanics*, 76(11):725–745, 2006.
- [78] Eric Béchet, Matthias Scherzer, and Meinhard Kuna. Application of the X-FEM to the fracture of piezoelectric materials. *International Journal for Numerical Methods in Engineering*, 77(11):1535–1565, 2009.
- [79] R.R. Bhargava and Kuldeep Sharma. A study of finite size effects on cracked 2-d piezoelectric media using extended finite element method. *Computational Materials Science*, 50(6):1834–1845, 2011.
- [80] Tinh Quoc Bui and Chuanzeng Zhang. Extended finite element simulation of stationary dynamic cracks in piezoelectric solids under impact loading. *Computational Materials Science*, 62:243–257, 2012.
- [81] Peng Liu, Tiantang Yu, Tinh Quoc Bui, and Chuanzeng Zhang. Transient dynamic crack analysis in non-homogeneous functionally graded piezoelectric materials by the X-FEM. *Computational Materials Science*, 69:542–558, 2013.
- [82] Peng Liu, Tiantang Yu, Tinh Quoc Bui, Chuanzeng Zhang, Yepeng Xu, and Chee Wah Lim. Transient thermal shock fracture analysis of functionally graded piezoelectric materials by the extended finite element method. *International journal of solids and structures*, 51(11-12):2167–2182, 2014.

- [83] Kuldeep Sharma, Tinh Quoc Bui, Ch. Zhang, and RR Bhargava. Analysis of a subinterface crack in piezoelectric bimetals with the extended finite element method. *Engineering Fracture Mechanics*, 104:114–139, 2013.
- [84] Tiantang Yu, Tinh Quoc Bui, Peng Liu, Chuanzeng Zhang, and Sohichi Hirose. Interfacial dynamic impermeable cracks analysis in dissimilar piezoelectric materials under coupled electromechanical loading with the extended finite element method. *International Journal of Solids and Structures*, 67:205–218, 2015.
- [85] Felipe García-Sánchez, Chuanzeng Zhang, and Andrés Sáez. 2-d transient dynamic analysis of cracked piezoelectric solids by a time-domain BEM. *Computer Methods in Applied Mechanics and Engineering*, 197(33-40):3108–3121, 2008.
- [86] Jun Lei, Lili Yun, and Tinh Quoc Bui. Numerical simulation of crack growth in piezoelectric structures by bem. *Engineering Analysis with Boundary Elements*, 85:30–42, 2017.
- [87] Tinh Quoc Bui. Extended isogeometric dynamic and static fracture analysis for cracks in piezoelectric materials using nurbs. *Computer Methods in Applied Mechanics and Engineering*, 295:470–509, 2015.
- [88] Tinh Quoc Bui, Sohichi Hirose, Chuanzeng Zhang, Timon Rabczuk, Cheng-Tang Wu, Takahiro Saitoh, and Jun Lei. Extended isogeometric analysis for dynamic fracture in multi-phase piezoelectric/piezomagnetic composites. *Mechanics of Materials*, 97:135–163, 2016.
- [89] Raymond Wildman and George Gazonas. A dynamic electro-thermo-mechanical model of dielectric breakdown in solids using peridynamics. *Journal of Mechanics of Materials and Structures*, 10(5):613–630, 2015.
- [90] Jacob M. Wernik and Shaker A. Meguid. Recent developments in multifunctional nanocomposites using carbon nanotubes. *Applied Mechanics Reviews*, 63(5), 2010.
- [91] Amin Salehi-Khojin, Soumen Jana, and Wei-Hong Zhong. Thermal-mechanical properties of a graphitic-nanofibers reinforced epoxy. *Journal of nanoscience and nanotechnology*, 7(3):898–906, 2007.

- [92] Qing Hua Li and Jian Hua Zhang. Effects of nano fillers on the conductivity, adhesion strength and reliability of isotropic conductive adhesives (ICAs). In *Key Engineering Materials*, volume 353, pages 2879–2882. Trans Tech Publ, 2007.
- [93] Byung Chul Kim, Sang Wook Park, and Dai Gil Lee. Fracture toughness of the nano-particle reinforced epoxy composite. *Composite structures*, 86(1-3):69–77, 2008.
- [94] Naveen Prakash and Gary D. Seidel. Electromechanical peridynamics modeling of piezoresistive response of carbon nanotube nanocomposites. *Computational Materials Science*, 113:154–170, 2016.
- [95] Florin Bobaru and Monchai Duangpanya. The peridynamic formulation for transient heat conduction. *International Journal of Heat and Mass Transfer*, 53(19-20):4047–4059, 2010.
- [96] Florin Bobaru and Monchai Duangpanya. A peridynamic formulation for transient heat conduction in bodies with evolving discontinuities. *Journal of Computational Physics*, 231(7):2764–2785, 2012.
- [97] N. Prakash. *Coupled electromechanical peridynamics modeling of strain and damage sensing in carbon nanotube reinforced polymer nanocomposites*. PhD thesis, Virginia Tech, 2017.
- [98] Naveen Prakash and Gary D. Seidel. Computational electromechanical peridynamics modeling of strain and damage sensing in nanocomposite bonded explosive materials (NCBX). *Engineering Fracture Mechanics*, 177:180–202, 2017.
- [99] Naveen Prakash and Gary D Seidel. Coupled electromechanical peridynamic modeling of strain and damage sensing in granular energetic materials. In *58th AIAA/ASCE/AHS/ASC Structures, Structural Dynamics, and Materials Conference*, page 0126, 2017.
- [100] Vito Diana and Valter Carvelli. An electromechanical micropolar peridynamic model. *Computer Methods in Applied Mechanics and Engineering*, 365:112998, 2020.
- [101] Pranesh Roy and Debasish Roy. Peridynamics model for flexoelectricity and damage. *Applied Mathematical Modelling*, 68:82–112, 2019.

- [102] Francisco S. Vieira and Aurélio L. Araújo. Implicit non-ordinary state-based peridynamics model for linear piezoelectricity. *Mechanics of Advanced Materials and Structures*, pages 1–22, 2021.
- [103] Michael S Breitenfeld, Philippe H Geubelle, Olaf Weckner, and S. A. Silling. Non-ordinary state-based peridynamic analysis of stationary crack problems. *Computer Methods in Applied Mechanics and Engineering*, 272:233–250, 2014.
- [104] Meinhard Kuna. Fracture mechanics of piezoelectric materials—where are we right now? *Engineering Fracture Mechanics*, 77(2):309–326, 2010.
- [105] S. A. Silling and R. B. Lehoucq. Peridynamic theory of solid mechanics. *Advances in Applied Mechanics*, 44:73–168, 2010.
- [106] F. Bobaru, J. T. Foster, P. H. Geubelle, and S. A. Silling. *Handbook of Peridynamic Modeling*. CRC Press Taylor & Francis Group, 2016.
- [107] R. D. Cook, D. S. Malkus, M. E. Plesha, and R. J. Witt. *Concepts and applications of finite element analysis*. John wiley & sons, 2007.
- [108] T. Belytschko, W. K. Liu, B. Moran, and K. Elkhodary. *Nonlinear finite elements for continua and structures*. John wiley & sons, 2013.
- [109] Y. D. Ha and F. Bobaru. Studies of dynamic crack propagation and crack branching with peridynamics. *International Journal of Fracture*, 162:229–244, 2010.
- [110] J. F. Kalthoff and S. Winkler. Failure mode transition at high rates of shear loading. *DGM Informationsgesellschaft mbH, Impact Loading and Dynamic Behavior of Materials*, 1:185–195, 1988.
- [111] J. F. Kalthoff. Modes of dynamic shear failure in solids. *International Journal of Fracture*, 101:1–31, 2000.
- [112] X. Zhou, Y. Wang, and Q Qian. Dynamic crack propagation based on loss of hyperbolicity and a new discontinuous enrichment. *European Journal of Mechanics-A/Solids*, 60:227–299, 2016.

- [113] Petia Dineva, Dietmar Gross, Ralf Müller, and Tsviatko Rangelov. Piezoelectric materials. In *Dynamic fracture of piezoelectric materials*, pages 7–32. Springer, 2014.
- [114] Jiashi Yang. *An introduction to the theory of piezoelectricity*, volume 9. Springer, 2005.
- [115] P. Li, Z.M. Hao, and W.Q. Zhen. A stabilized non-ordinary state-based peridynamic model. *Computer Methods in Applied Mechanics and Engineering*, 339:262–280, 2018.
- [116] Hailong Chen. Bond-associated deformation gradients for peridynamic correspondence model. *Mechanics Research Communications*, 90:34–41, 2018.
- [117] David Littlewood. Roadmap for software implementation. In *Handbook of peridynamic modeling*, pages 147–178. Chapman and Hall/CRC, 2016.
- [118] Bahattin Kilic and Erdogan Madenci. An adaptive dynamic relaxation method for quasi-static simulations using the peridynamic theory. *Theoretical and Applied Fracture Mechanics*, 53(3):194–204, 2010.
- [119] M.N.O. Sadiku. *Numerical Techniques in Electromagnetics with MATLAB*. CRC Press, 2009.
- [120] C.T. Sun and S.B. Park. Measuring fracture toughness of piezoceramics by Vickers indentation under the influence of electric fields. *Ferroelectrics*, 248(1):79–95, 2000.